High Precision Stress Measurements

in Semiconductor Structures

by Raman Microscopy

A dissertation of the

TU Dresden, Germany

for the degree of

Doctor of Natural Sciences
(Dr. rer. nat.)

presented by

BENJAMIN UHLIG

Accepted on the recommendation of:

Prof. L. M. Eng, TU Dresden
Prof. A. Michaelis, IKTS Fraunhofer Dresden

2009

Abstract

Stress in silicon structures plays an essential role in modern semiconductor technology. This stress has to be measured and due to the ongoing miniaturization in today's semiconductor industry, the measuring method has to meet certain requirements.

The present thesis deals with the question how Raman spectroscopy can be used to measure the state of stress in semiconductor structures. In the first chapter the relation between Raman peakshift and stress in the material is explained. It is shown that detailed stress maps with a spatial resolution close to the diffraction limit can be obtained in structured semiconductor samples. Furthermore a novel procedure, the so called *Stokes-AntiStokes-Difference* method is introduced. With this method, topography, tool or drift effects can be distinguished from stress related influences in the sample.

In the next chapter *Tip-enhanced Raman Scattering* (TERS) and its application for an improvement in lateral resolution is discussed. For this, a study is presented, which shows the influence of metal particles on the intensity and localization of the Raman signal. A method to attach metal particles to scannable tips is successfully applied. First TERS scans are shown and their impact on and challenges for high resolution stress measurements on semiconductor structures is explained.

Kurzzusammenfassung

Spannungen in Siliziumstrukturen spielen eine entscheidende Rolle für die moderne Halbleitertechnologie. Diese mechanischen Verspannungen müssen gemessen werden und die fortlaufende Miniaturisierung in der Halbleiterindustrie stellt besondere Anforderungen an die benutzte Messmethode.

Diese Arbeit beschäftigt sich mit dem Thema, inwieweit Raman Spektroskopie zur Spannungsmessung in Halbleiterstrukturen geeignet ist. Im ersten Kapitel wird der Zusammenhang zwischen Raman Peakverschiebung und mechanischer Spannung erläutert. Es wird gezeigt wie man detaillierte *stress maps* in strukturierten Halbleiterproben erhält mit einer Auflösung nah am Diffraktionslimit. Darüberhinaus wird ein neuartiges Verfahren, die sogenannte *Stokes-AntiStokes-Differenz* Methode vorgestellt mit deren Hilfe man Einflüsse von Topographie, Geräteeffekten und Drift von den zu messenden Spannungszuständen in der Probe unterscheiden kann.

Im nächsten Kapitel wird diskutiert, inwiefern der Ansatz von *Tip-enhanced Raman Scattering* (TERS), also spitzenverstärkter Raman Streuung genutzt werden kann um die laterale Auflösung bei Raman Spannungsmessungen zu erhöhen. Hierzu wird eine Studie präsentiert, die zeigt, welchen Einfluss Metallpartikel auf Erhöhung und Lokalisierung des Ramansignals haben. Eine Methode um Metallpartikel an scannbare Spitzen anzubringen wird erfolgreich angewendet. Erste TERS-Scans werden gezeigt und deren Bedeutung und Herausforderungen bei der hochaufgelösten Messung von Spannungen in Halbleiterstrukturen wird erläutert.

Contents

1. Introduction

Stress or strain is one of the most important material properties in present microelectronic devices. Film stresses due to thermal mismatch of different layers can lead to film delamination, formation of voids or cracks and electromigration induced damage [1]. On the other hand there is process induced stress which can enhance the mobility of the electric carriers in the transistor gate channel and thus improve the device characteristics [2, 3]. It is therefor crucial to find a way to measure the amount and kind of stress in the device.

A well known and widely used method for stress measurements in semiconductor industry is obtaining the wafer curvature or bow and calculating the stress situation in the film. However this method gives only an integral value over the whole wafer. Going one step further one can use interferometric measurements to gain excess to local wafer curvature. Measuring the lattice constant by the means of x-ray spectroscopy increases the spatial resolution even more. Though being very sensitive to small stress variations one is still restrained by the size of the measuring spot in the range of 0.5 mm^2.

Convergent beam electron diffraction (CBED) with the help of transmission electron microscopy (TEM) lamellas enables measurement in the nanometer regime. However destructive sample preparation, time consumption and extensive modeling limits this method for use in today's semiconductor metrology. A suitable method for measuring stress in semiconductor structures is Raman microscopy. It is a fast, non destructive technique which offers good stress sensitivity and spatial resolution. Unfortunately the resolution is limited to the laser spot size, around 500 nm.

Following *Moore's Law* [4], the semiconductor industry is moving to smaller and smaller structures which results in more complex elements and new kind of materials like strained silicon or silicon-germanium [5, 6]. Thus, new challenges arise when physical properties have to be measured. In order to meet the present demands in transistor dimensions (< 100 nm) one has to use UV laser or to go beyond the diffraction limit and find new techniques. Tip enhanced Raman spectroscopy (TERS) is such an approach.

Figure 4.4 shortly summarizes the motivation of this thesis. Starting in the upper left corner, unwanted stress after film deposition or structuring as well as intentionally applied stress, for example in the transistor gate channel, have to be measured. This can be accomplished by Raman microscopy illustrated in the lower left corner. Due to the miniaturization of devices depicted in the upper right corner, the regions from where stress information has to be obtained becomes smaller and goes below the diffraction limit. Thus conventional Raman microscopy has to be enhanced to increase the spatial resolution of the technique.
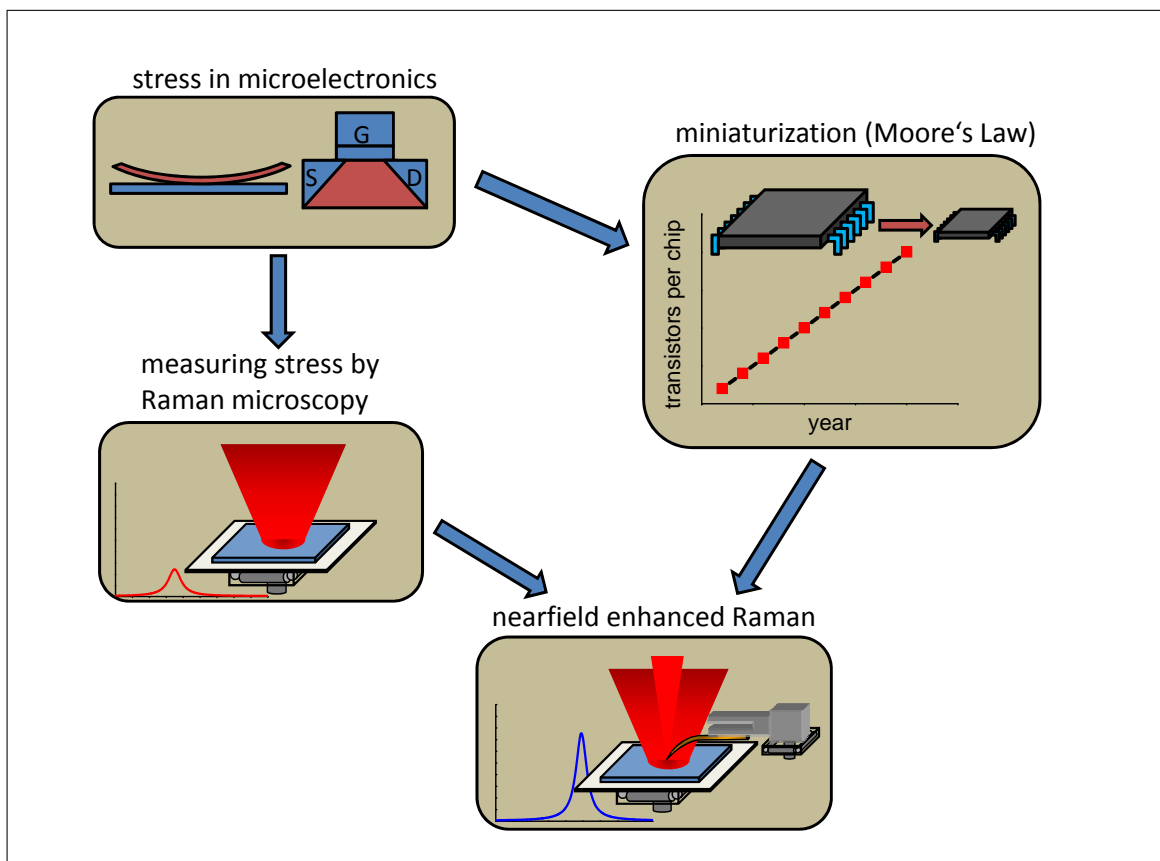

Figure 1.1.: Motivation scheme. A conventional way of measuring unwanted or applied stress in microelectronics is using Raman microscopy. Due to the scaling of devices, the technique has to be improved to yield better spatial resolution and higher accuracy, this can be achieved by the means of near-field enhanced Raman spectroscopy.

The term *high precision* in the title of this thesis: *High Precision Stress Measurements in Semiconductor Structures by Raman Microscopy* refers to several issues that are discussed throughout this work. At first the spectral resolution, which translates directly into the stress sensitivity, i.e. what is the smallest detectable stress variation, is discussed in chapter 2. The Raman tool is introduced together with its improvements and limitations. A detailed view on the scanning Raman technique with respect to stress mapping on semiconductor materials is given. In the same chapter the second meaning of *high precision* is dealt with. The important question: is the measured effect stress related or are there any influencing artifacts, for example from topography features, is analyzed and a novel method for data deconvolution and extraction of stress related effects in presented. The important steps to obtain a real map of the stress distribution in a sample from a Raman scan are explained.

Finally in chapter 3 the important topic of the lateral resolution, leading to the idea of near-field enhanced Raman spectroscopy is discussed. A preliminary study of metal particles on the surface to enhance the Raman signal and an evaluation of TERS on semiconductor samples is given. It is shown that there is an increase in Raman signal intensity, signal contrast and most importantly an increase in the spatial resolution, but the application of scanning TERS on solids still remains challenging and contains special demands and limitations.

2. Stress Measurements

2.1. Introduction

In this chapter the measurement of stress in micro structured silicon samples by the means of Raman spectroscopy is presented. At first the history of the Raman effect and the relationship between the stress state in the material and its effect on the Raman spectrum is described in section 2.1. The theoretical background of both issues is shown in section 2.2 together with an exemplary calculation of the Raman peak shift in presence of uniaxial stress.

Section 2.3 deals with the setup of the used Raman microscope, some detailed views on specific parts which are necessary for high precision Raman measurements and an overview of the used samples. The actual measurements can be found in section 2.4, including single spectra, linescans and two-dimensional mappings. A novel method to deconvolute information in Raman spectra regarding stress and non-stress related effects is presented in section 2.4.4 together with several measurements where this method was applied successfully.

Finally in section 2.5 remarks on various effects which occurred during the measurements, like the intensity increase at structural edges or the effect of defocussing are discussed together with some statements regarding the simulation of Raman linescans with the help of finite element calculations and modeling.

2.1.1. Raman history

Analyzing the interaction between light and matter is an excellent and wide-used way to easily obtain a variety of material properties in a sample, and it has been a field of research since the 19th century. One of the early scientific papers concerning light interaction dates back to 1872, when Lord Rayleigh explained the blue color of the sky by his classical theory of elastically scattered light [7]. In 1928 Sir Chandrasekhara Venkata Raman, an Indian physicist, experimented with light scattered inelastically from a liquid. The observed effect, which was theoretically predicted five years earlier by Adolf Smekal [8] was named Raman scattering [9] and its experimental discovery was awarded with the Nobel prize in 1930. Shortly after, Raman spectroscopy became the primary method for non-destructive chemical analysis but it was replaced by infrared spectroscopy due to its easier use and less demanding experimental setup. With the invention of the laser, a new monochromatic light source with high intensity was available which posed a good way to overcome the inherent low scattering cross section for Raman scattering being several orders of magnitude lower than the cross section for fluorescence. Hence the first measurements of semiconductor samples became possible [10], with the first stress measurement on structured silicon samples in 1989 [11].

2.1.2. The Raman effect

Quantum mechanically the Raman effect involves the absorption and emission of photons. The incident photon excites the molecule or crystal lattice and lifts it in a higher virtual energy state. It than relaxes almost instantaneously into an excited vibrational state by the emission of a photon. The energy difference between incident and emitted photon depends on the characteristics of the vibrational state and hence can be used to get information about the molecular or lattice binding properties. The effect is illustrated in figure 2.1 together with an energy diagram showing the process involving the ground state *0*, a virtual state *v*, and the excited vibrational state *1*.

If the nature of the binding is altered, for example when a certain stress σ is applied, the emitted photon will have a different energy because the excited vibrational state has changed. This situation is shown in figure 2.2 with a changed vibrational state 1_s.
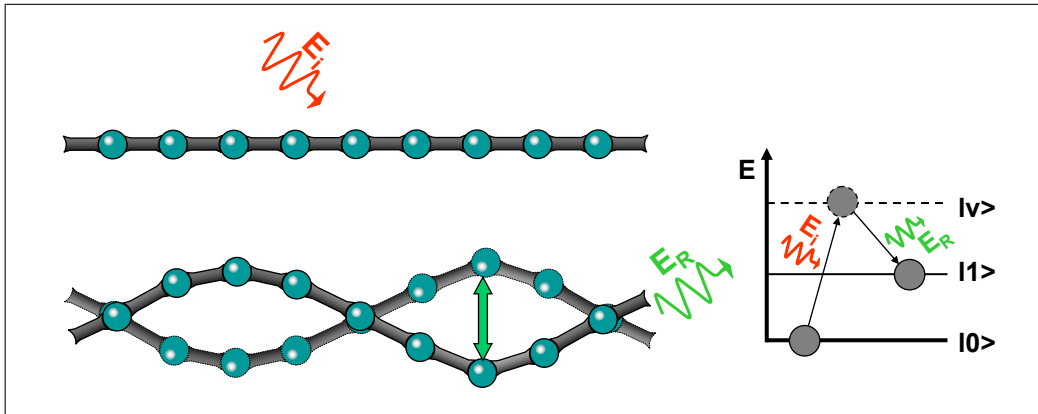
Figure 2.1.: Illustration of the Raman effect. A photon (red) is incident on an atomic chain and excites the system into a higher virtual state. From there it relaxes into a vibrational state described by an oscillation of the chain under the emission of a second Raman photon (green). The energy difference between both photons is given by the oscillation of the chain. On the right side the corresponding energy diagram is shown.
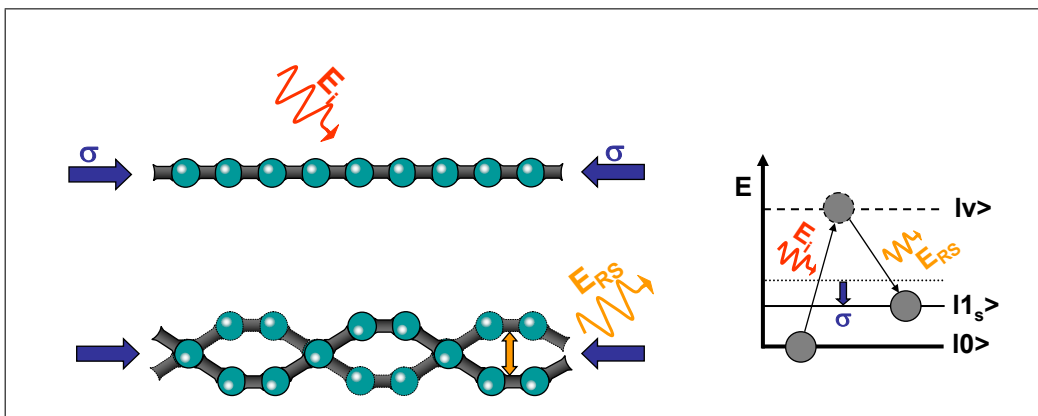

Figure 2.2.: Illustration of the Raman effect under the effect of a stress σ.

2.1.3. Measuring stress with Raman

One of the first who dealt with the Raman effect in crystals was Loudon who derived the Raman tensors for silicon and laid the foundation for later calculations [12]. The dependency between the stress state in silicon and its effect on the phonon vibrations was extensively studied by Anasstasakis et al [13, 14]. They showed that the main Raman peak of a silicon sample at around $520\ \text{cm}^{-1}$ is in fact a three fold degenerated peak from the first order longitudinal optical phonon, hence called LO phonon mode. Under the effect of stress this degeneracy is split and one could observe singlets or doublets of peaks in principle. However, temperature related peak broadening as well as the natural line width mostly prevent the observation of distinct peaks so just the sum can be seen in the Raman spectrum. Another important statement is, that stress itself is not a scalar but in general a tensor with at most six non-zero components. Each of them influences the peak position of the Raman signal which means that we have six unknown components versus one known value, the Raman peak shift. This shows that we have to make certain assumptions about the stress state in the material and that it is rather difficult to make assumptions about absolute stress values or different stress states just by Raman measurements.

In a limited way it is possible to get a closer look at the tensorial nature of the stress, involving different polarization settings [84], for example near a scratch in a silicon sample [17]. In addition, samples which were mechanically bent before the measurements [18], or special microstructuring [19] can be used to further locate the stress state. A validation of the stress measured by Raman microscopy in industrial samples can be approached by modeling of the structures, e.g. with finite element models [20, 21].

2.2. Theoretical considerations

2.2.1. Raman scattering

The Raman effect refers to an interaction between electromagnetic radiation and matter. An incoming monochromatic beam with the frequency ω_0 interacts with the sample and the scattered light with the frequency ω_s is detected. Three main cases regarding the difference frequency Ω can be distinguished:

1. Rayleigh scattering, an elastic process where no change in energy is observed

$$\hbar\omega_s = \hbar\omega_0 \ , \tag{2.1}$$

2. Stokes scattering, an inelastic process where the scattered energy is lower

$$\hbar\omega_s = \hbar\omega_0 - \hbar\Omega \ , \tag{2.2}$$

3. and Anti-Stokes scattering, an inelastic process where the scattered energy is higher than the incoming energy

$$\hbar\omega_s = \hbar\omega_0 + \hbar\Omega \ . \tag{2.3}$$

Following classical theory the electric field $\vec{E}$ induces a polarization $\vec{P}$ in the material with the susceptibility tensor χ and the permittivity ϵ_0:

$$\vec{P} = \epsilon_0\chi\vec{E} \tag{2.4}$$

With the plane wave description for the incoming light it follows:

$$\vec{P} = \epsilon_0\chi\vec{E}_0\cos(\omega t) \tag{2.5}$$

The susceptibility is dependent on molecular or lattice scattering. It can be expanded in a Taylor-series with respect to the coordinate of a vibration q_j:

$$\chi = \chi_0 + \sum_j \frac{\partial\chi}{\partial q_j}q_j + \dots \tag{2.6}$$

Higher orders are neglected and the sum goes over all possible vibration modes. The vibration q_j can be described by an oscillation with the frequency Ω_j:

$$q_j = q_{j0}\cos(\Omega_j t) \tag{2.7}$$

Combining equations (2.5), (2.6) and (2.7) leads to:

$$\vec{P} = \epsilon_0 \chi_0 \vec{E}_0 \cos(\omega t) + \sum_j \epsilon_0 \vec{E}_0 \frac{\partial \chi}{\partial q_j} q_{j0} \cos(\Omega_j t) \cos(\omega t) \tag{2.8}$$

Finally with the help of a cosine addition theorem this reads as:

$$\vec{P} = \underbrace{\epsilon_0 \chi_0 \vec{E}_0 \cos(\omega t)}_{\text{Rayleigh}} + \frac{1}{2} \sum_j \epsilon_0 \vec{E}_0 \frac{\partial \chi}{\partial q_j} q_{j0} \left[\underbrace{\cos((\omega + \Omega_j)t)}_{\text{Anti Stokes}} + \underbrace{\cos((\omega - \Omega_j)t)}_{\text{Stokes}} \right] \tag{2.9}$$

where the first term represents Rayleigh scattering, the second term Anti-Stokes, and the right most term Stokes scattering.

It can be seen that Stokes or Anti-Stokes only take place if the derivative $\frac{\partial \chi}{\partial q_j}$, which is also called Raman tensor, is non zero. This leads to the well known selection rules. For silicon the three Raman tensors for a normal xyz coordinate system are [12]:

$$R_x = \begin{pmatrix} 0 & 0 & 0 \\ 0 & 0 & d \\ 0 & d & 0 \end{pmatrix}, \ R_y = \begin{pmatrix} 0 & 0 & d \\ 0 & 0 & 0 \\ d & 0 & 0 \end{pmatrix}, \ R_z = \begin{pmatrix} 0 & d & 0 \\ d & 0 & 0 \\ 0 & 0 & 0 \end{pmatrix} \tag{2.10}$$

with a constant d.

The total scattering intensity I is dependent on the Raman tensors R_i and the directions of incoming $\vec{e}_0$ and scattered polarization $\vec{e}_s$ and it is proportional to:

$$I \propto \sum_i |\vec{e}_0 R_i \vec{e}_s| \tag{2.11}$$

2.2.2. Influence of strain on phonons

Not only molecular vibrations can be studied by Raman spectroscopy. In a similar fashion it can be used to look at crystalline solids where lattice vibrations, so called phonons, represent the elementary vibrations which alter the susceptibility tensor. In silicon the observed Raman peak is in fact the result from the three optical phonons at $\vec{k} = 0$ which are degenerated in the absence of any strain in the crystal. Applying a strain ϵ_{ij} lifts this degeneracy and a split to terms linear in the strain in three different singlets or a singlet and a doublet takes place [22]. The individual phonon mode's frequency ω_n is then given by:

$$\sum_\beta K_{n,\alpha\beta} \eta_\beta = \omega_n^2 \eta_\alpha \tag{2.12}$$

with the second rank force constant tensor $K_{\alpha\beta}$ and η_{α} the Cartesian coordinates of the eigenvectors with $\alpha, \beta = 1\text{-}3$. Expanding the elements of the force constant tensor in powers of the elements of the strain tensor ϵ_{ij} leads to:

$$K_{n,\alpha\beta} = K^{(0)}_{n,\alpha\beta} + \sum_{ij} \epsilon_{ij} K^{(\epsilon)}_{ij\alpha\beta} \tag{2.13}$$

The symmetric fourth rank tensor $K^{(\epsilon)}$ has only three independent nonzero elements for silicon, namely:

$$
\begin{aligned}
K^{(\epsilon)}_{1111} &= K^{(\epsilon)}_{2222} = K^{(\epsilon)}_{3333} =: p \\
K^{(\epsilon)}_{1122} &= K^{(\epsilon)}_{1133} = K^{(\epsilon)}_{2233} =: q \\
K^{(\epsilon)}_{1212} &= K^{(\epsilon)}_{1313} = K^{(\epsilon)}_{2323} =: r
\end{aligned}
\tag{2.14}
$$

Here the so-called phonon deformation potentials p, q, r are introduced which connect the strain in the lattice to the shift in phonon frequency [14]. Combining equation (2.12)-(2.14) leads to the following secular equation [13, 22]:

$$
\begin{vmatrix}
p\epsilon_{11} + q(\epsilon_{22} + \epsilon_{33}) - \lambda & 2r\epsilon_{12} & 2r\epsilon_{13} \\
2r\epsilon_{12} & p\epsilon_{22} + q(\epsilon_{33} + \epsilon_{11}) - \lambda & 2r\epsilon_{23} \\
2r\epsilon_{13} & 2r\epsilon_{23} & p\epsilon_{33} + q(\epsilon_{11} + \epsilon_{22}) - \lambda
\end{vmatrix} = 0
\tag{2.15}
$$

Here the eigenvalues λ_j are given by:

$$\lambda_j = \omega^2_{s,j} - \omega^2_{0,j} \tag{2.16}$$

with ω_s the frequency of the phonon in the presence of strain and ω_0 the frequency for the unstrained case. With the assumption that the frequency difference $\Delta\omega$ is small compared to ω_0 it follows:

$$\Delta\omega_j = \frac{\lambda_j}{2\omega_{0,j}} \tag{2.17}$$

2.2.3. Uniaxial stress

In the following the stress dependent Raman shift in the presence of uniaxial stress is calculated. Calculations for other stress states can be found in the literature [15]. For uniaxial stress in the material the stress tensor has the following form:

$$
\sigma' =
\begin{pmatrix}
\sigma'_{11} & 0 & 0 \\
0 & 0 & 0 \\
0 & 0 & 0
\end{pmatrix}
\tag{2.18}
$$

with the stress σ' oriented along the samples (100) x-axis with the value σ'_{11}.

Calculation of the Raman shift is done by solving the secular equation (2.15). To link stress effects to phonon frequency changes we use Hooke's law where the stress σ is connected to the strain ϵ by the fourth rank compliance tensor S:

$$\epsilon = S\sigma \tag{2.19}$$

The derived secular equation (2.15) from the last section is only true for the reference coordinate system with the axes x=[100], y=[010], z=[001]. However most microelectronic structures are oriented different so that we have to use the system with the axes oriented along x'=[110], y'=[-110], z'=[001]. To calculate stress induced Raman shifts either one transforms the strain/stress tensor into the reference system and solves the secular equation, or one calculates the secular equation in the sample system [23].

Transforming (2.19) to the sample system results in the strain tensor in the sample system ϵ':

$$\epsilon' = \frac{1}{2}\sigma' \begin{pmatrix} S_{11} + S_{12} + \frac{1}{2}S_{44} & 0 & 0 \\ 0 & S_{11} + S_{12} - \frac{1}{2}S_{44} & 0 \\ 0 & 0 & 2S_{12} \end{pmatrix} \tag{2.20}$$

Setting equation (2.20) into the following secular matrix transformed to the sample axis system:

$$\begin{vmatrix} p'\epsilon'_{11} + q'(\epsilon'_{22} + \epsilon'_{33}) - \lambda & (p-q)\epsilon'_{12} & 2r\epsilon'_{13} \\ (p-q)\epsilon'_{12} & p'\epsilon'_{22} + q'(\epsilon'_{33} + \epsilon'_{11}) - \lambda & 2r\epsilon'_{23} \\ 2r\epsilon'_{13} & 2r\epsilon'_{23} & p\epsilon'_{33} + q(\epsilon'_{11} + \epsilon'_{22}) - \lambda \end{vmatrix} = 0 \tag{2.21}$$

with the substitutions:

$$p' = \frac{p+q}{2} + r, \quad q' = \frac{p+q}{2} - r \tag{2.22}$$

results in the solutions for the eigenvalues λ_j:

$$\lambda_1 = \frac{1}{2}[(p+q)S_{11} + (p+3q)S_{12} + rS_{44}]\sigma_{11} \tag{2.23}$$

$$\lambda_2 = \frac{1}{2}[(p+q)S_{11} + (p+3q)S_{12} - rS_{44}]\sigma_{11} \tag{2.24}$$

$$\lambda_3 = [pS_{12} + q(S_{11} + S_{12})]\sigma_{11} \tag{2.25}$$

The Raman tensors in the sample system in the presence of stress R'_s are given by:

$$R'_{s1} = \begin{pmatrix} 0 & 0 & d \\ 0 & 0 & 0 \\ d & 0 & 0 \end{pmatrix}, \; R'_{s2} = \begin{pmatrix} 0 & 0 & 0 \\ 0 & 0 & -d \\ 0 & -d & 0 \end{pmatrix}, \; R'_{s3} = \begin{pmatrix} d & 0 & 0 \\ 0 & -d & 0 \\ 0 & 0 & 0 \end{pmatrix} \qquad (2.26)$$

In the common back scattering setup, i.e. the scattered beam travels in direction $z'=[001]$, only the third phonon mode can be observed when using light polarized in the sample's plane. This follows from the selection rules, see equation (2.11).

Combining equations (2.17), (2.20) and (2.23)-(2.25) finally gives the expression for the Raman shift in silicon $\Delta\omega_3$ for the case of uniaxial stress σ_{11}:

$$\Delta\omega_3 = \frac{1}{2\omega_0}[pS_{12} + q(S_{11} + S_{12})]\sigma_{11} \qquad (2.27)$$

If we fill in the phonon deformation potentials p, q and r from [14] and the compliance tensor elements S_{11} and S_{12} for silicon from [24], the relationship between Raman peak shift and stress for the uniaxial case becomes:

$$\Delta\omega_3 = -2.01 \; 10^{-9}\sigma_{11} \qquad (2.28)$$

with $\Delta\omega_3$ in cm^{-1} and σ_{11} in Pa. In other words, a peak shift of $1cm^{-1}$ is caused by an uniaxial stress of about 500 MPa.

2.3. Experimental setup

2.3.1. Raman Microscope

A commercially available Raman spectrometer (InVia) from Renishaw[1] is used. It contains three available wavelengths, a 488 nm Argon ion laser, a 532 nm Nd:YAG laser, and a 633 nm Helium-Neon laser. The polarization of the incoming light can be rotated by a motorized lambda half waveplate and the scattered light can be analyzed by using two perpendicular polarizing filters. The laser light is focused on the sample by an objective and collected in backscattering configuration through the same objective. For diffraction, a 3000 lines grating for the 488 nm and the 532 nm laser, or a 2400 lines grating for the 633 nm laser, both working in minus first order, is used. Detection is done by a Pixies CCD camera with 2048x512 pixels with 13.5 μm pixel width, cooled down to $-70°$C. The sample is scanned by a piezo driven AFM stage with a precision of about 0.1 nm. A scheme of the setup is shown in figure 2.3.

2.3.2. Calibration issues

In conventional Raman measurements, for example for the detection of chemical components in a sample, basically just the intensities or even simpler the existence of specific peaks is important. When using Raman microscopy to study stress states in semiconductor structures two more issues have to be taken into account. On the one hand we need good lateral resolution in order to assign specific stress states to separate regions on the sample, and on the other hand we need high spectral resolution for being able to quantify small changes in the peak frequency.

The lateral resolution in micro Raman spectroscopy is defined by the use of the laser wavelength and the optical setup of the tool. The latter influence comes from different sources like the numerical aperture of the used objective, the quality of all optical elements like lenses and mirrors and the confocality of the tool.

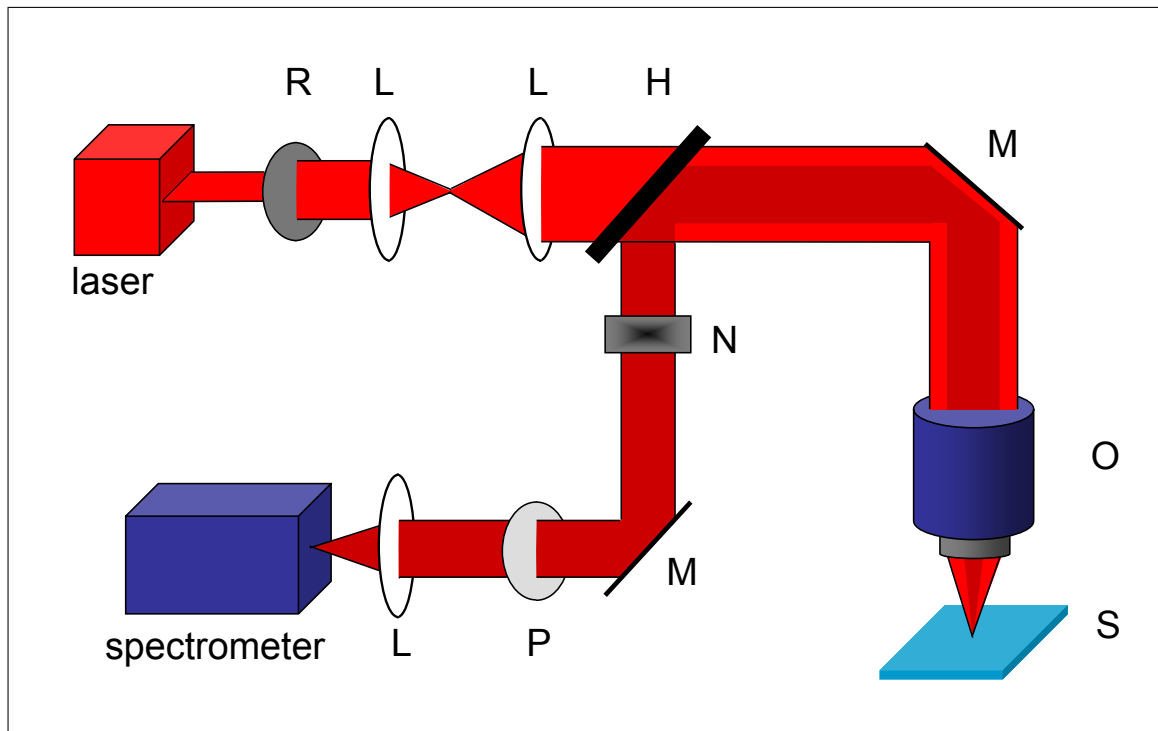[1]Renishaw plc, United Kingdom, http://www.renishaw.com

Figure 2.3.: Setup of the Raman microscope. Linearly polarized light from the laser can be rotated with an polarizer (R), travels through some lenses (L), passes a half transparent mirror (H) and is focused via a mirror (M) through the objective (O) onto the sample (S). The Raman scattered light is then collected through the same objective, passes the notch filter (N) to get rid of the Rayleigh line and can be analyzed by a polarizing filter (P). In the spectrometer it is then diffracted by a grating onto a CCD camera.

Regarding the confocality, the used Raman tool does not use the standard pinhole for cutting out out-of-focus regions of the scattered beam. Instead the pinhole is represented by an entrance slit for the vertical clipping and the choice of pixel rows on the CCD array for horizontal clipping. This means we can tune the confocality, of course at the cost of signal intensity, by narrowing the entrance slit and choosing a smaller number of CCD pixel rows used for signal accumulation.

The influence of the entrance slit on the intensity of the Raman signal is shown in figure 2.4. The slit position can be changed by applying certain offsets and it has to be matched with the middle of the beam in order to not lose important information. The opening of the slit can be narrowed down to $10\,\mu m$. Increasing the slit opening increases the signal up to a point where the whole laser beam can pass through the slit.
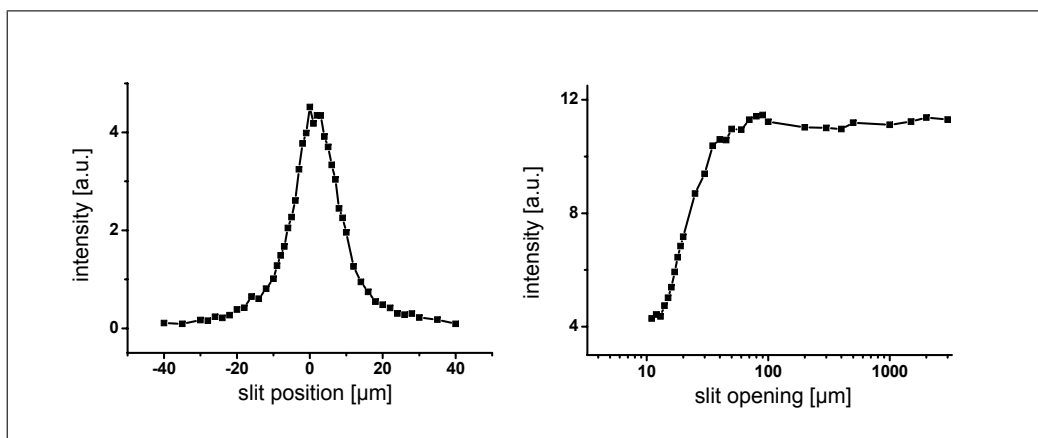
Figure 2.4.: *Left:* Influence of slit position on the signal intensity, *Right:* influence of the slit opening on the peak intensity, note the logarithmic scale for the slit width.

The impact of these confocality settings is demonstrated in figure 2.5. A linescan over a silicon edge was done and the resulting silicon intensity plot was fitted by a step function to compare the widths and thus making a statement about the lateral resolution. The standard mode curve was obtained with a slit opening of $50\,\mu m$ and an accumulation of about 40 pixel rows. The confocal mode curve was collected with a slit width of $15\,\mu m$ at a pixel accumulation of 10 rows. By changing these settings the width of the step curve could be narrowed from about 370 nm to 290 nm, an improvement of about 22%. It should be clearly stated that these values do not represent any numbers of actual lateral resolution,

a term which is used with many different definitions anyway. Here the width of the step is defined by the points where the intensity drops by $1/e^2$.
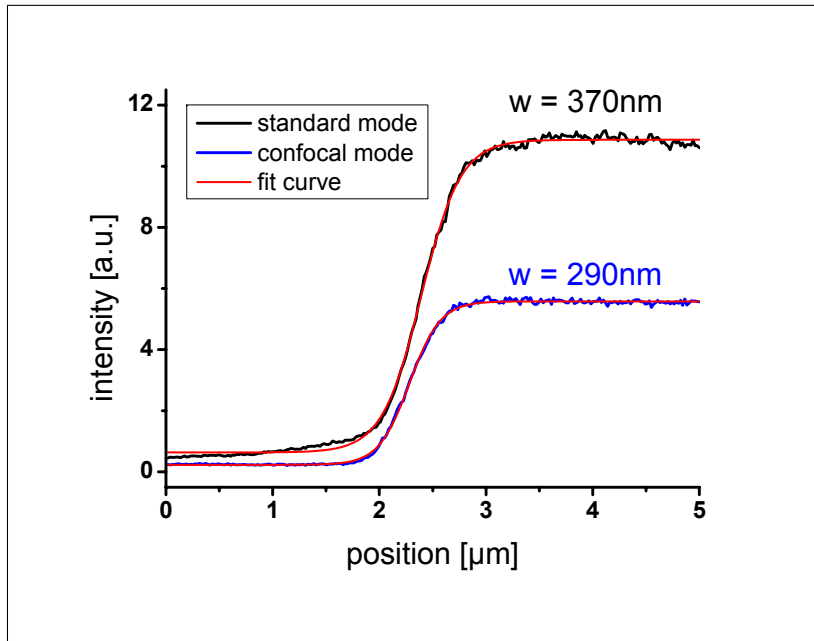

Figure 2.5.: Linescan over a silicon edge with two different confocality settings with step curve fits. Confocal mode scan was done with decreased slit width and smaller number of CCD pixel rows.

The spectral resolution is mainly influenced by the number of grooves in the diffraction grating, the focal length of the spectrometer and the width of the individual pixels on the CCD camera. To be sure that the Raman peak position displayed in the spectrum is exact, the instrument has to be calibrated. This was done by taking a neon light source and measuring its different excitation lines. The measured peak frequencies were then compared to the values of the neon lines known from literature and a calibration fit curve was automatically calculated. Because the grating will be rotated during Raman measurements to cover different spectral ranges this rotation has to be included in the calibration procedure as well. Another error source are the pixel columns: when the exact same neon line hits pixel number 1 it should read the same peak position as it would hit pixel number 2048. Often these dependencies are not considered in Raman measurements, but they have an impact on the actual peak position, especially during high precision measurements.

The effect is demonstrated in figure 2.6 where both, the Stokes and Anti-Stokes peak position of a silicon sample were plotted, after changing the grating rotation step by step, so that the spectrum's center wavelength is varied. The ideal

case would be two horizontal lines for Stokes and Anti-Stokes at the exact same absolute wavenumber, but the grating rotation and the different pixel columns where the silicon peak hits, read as a different peak position in the spectrum. It is therefore crucial that we don't change the rotation position of the grating when comparing two measurements, the silicon peak should always hit the same pixel columns. The second thing is, that Stokes and Anti-Stokes line should be brought together, at least for the center wavelength value used during the measurement. This can be done by applying a certain grating offset, which shifts the peak positions displayed in the spectrum linearly to lower or higher wavenumbers.
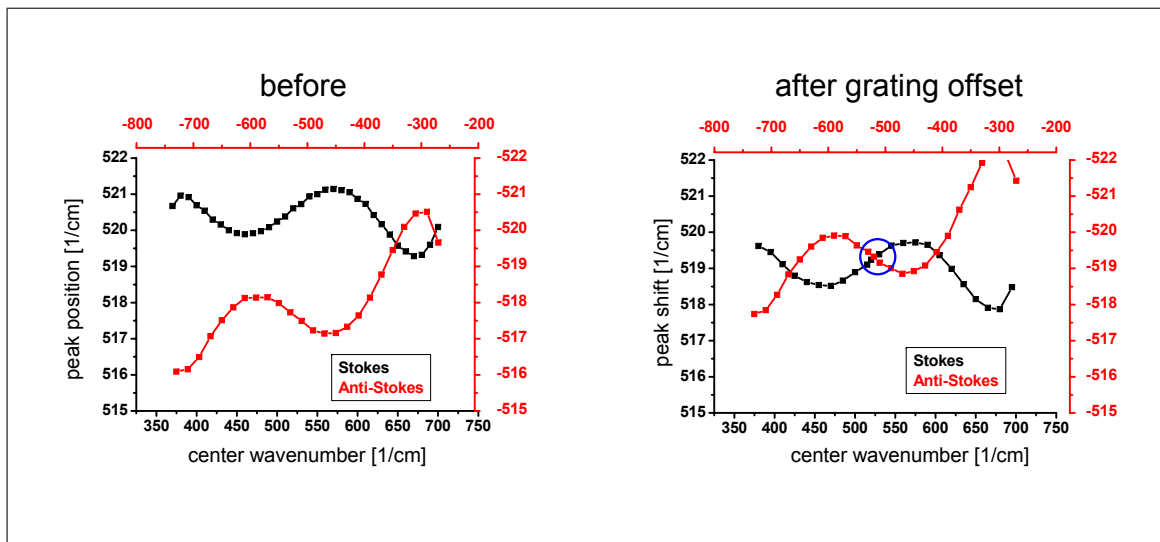
Figure 2.6.: *Left:* Stokes and Anti-Stokes peak positions displayed in silicon spectrum with varying grating rotation defined by the center wavenumber of the covered spectral range. *Right:* Peak positions brought together by applying a grating offset, the blue circle marks the ideal point which should be used for further measurements.

Figure 2.7 shows that the grating offset procedure indeed results in a linear shift of the measured Stokes and Anti-Stokes peak position. The somewhat greater deviation from the Anti-Stokes data around the fit curve is due to larger fitting errors caused by the lower Anti-Stokes peak intensity.
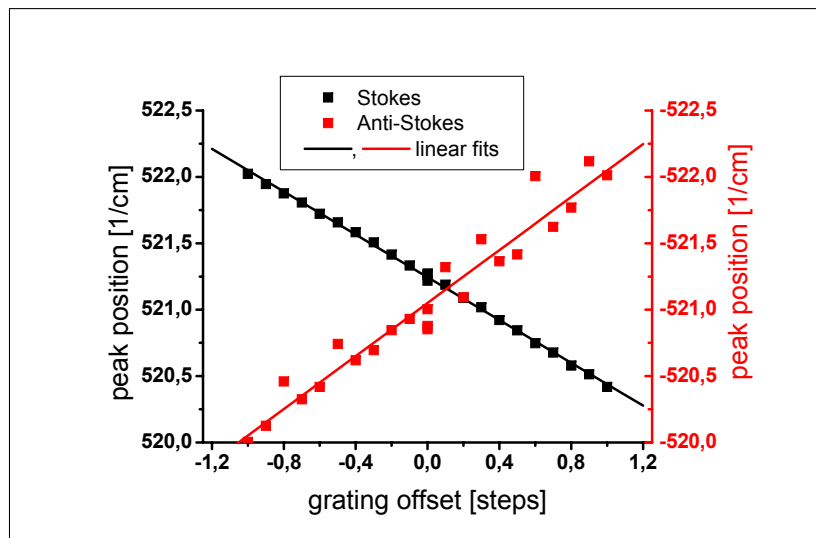

Figure 2.7.: Plot of measured Stokes and Anti-Stokes peak position versus grating offset. The fitted straight lines show the linear dependence.

2.3.3. Sample preparation

Most samples used throughout the micro Raman measurements were silicon sample pieces cut from a wafer. The ones used for measurements on industrial chips were structured by e-beam lithography or etching processes and filled with silicon-oxide by different processes. The second kind of samples had different layers consisting of a silicon substrate followed by a silicon-oxide layer and on the surface a strained silicon layer. These strained silicon on insulator samples will be called sSoI. The fabrication process, involving 'wafer-bonding' and 'smart-cutting' of the strained silicon layer can be found in the literature [25, 26]. Structured sSoI samples with differently sized pads or lines were produced with e-beam lithography and reactive ion etching. The two types of samples are illustrated in figure 2.8.
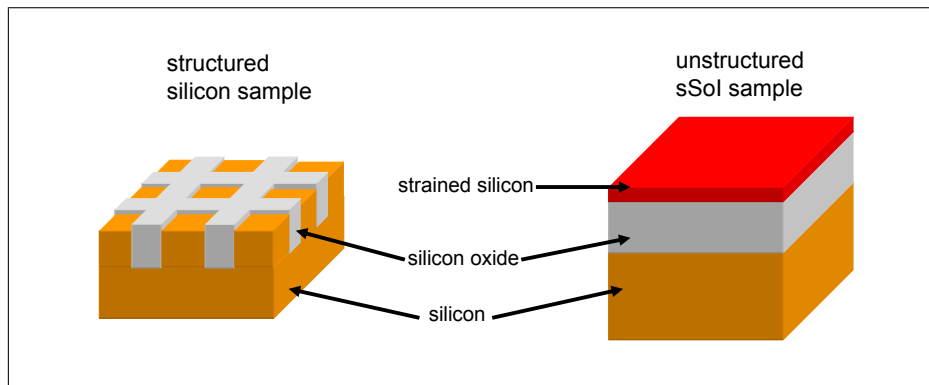
Figure 2.8.: *Left:* Sketch of a structured silicon sample filled with silicon oxide, *Right:* layered sSoI sample.

2.4. Results

2.4.1. Instrument characterization

Laser parameters

Many experiments deal with stacked samples like strained silicon on insulator (sSoI). Here we can use the information from Raman spectroscopy to distinguish between two stress states in one material. Figure 2.9 shows two Raman spectra of such a sSoI sample after excitation with two different laser wavelengths. After fitting the spectrum with two Lorentz curves, we see one peak at around $520\,\mathrm{cm}^{-1}$ which belongs to the stress free silicon substrate, as well as one peak at around $516\,\mathrm{cm}^{-1}$ which can be attributed to the strained silicon surface layer. Because of the different penetration depths of the used lasers, the ratio of the two peak intensities changes. Both spectra were normalized to the fitted bulk silicon peak, hence the blue laser spectrum shows a higher intensity in the strained silicon peak due to its smaller penetration depth. The inset shows the sample's structure, note that the intermediary silicon oxide layer shows no significant Raman peak because it is almost fully transparent to laser light in the used wavelength region.
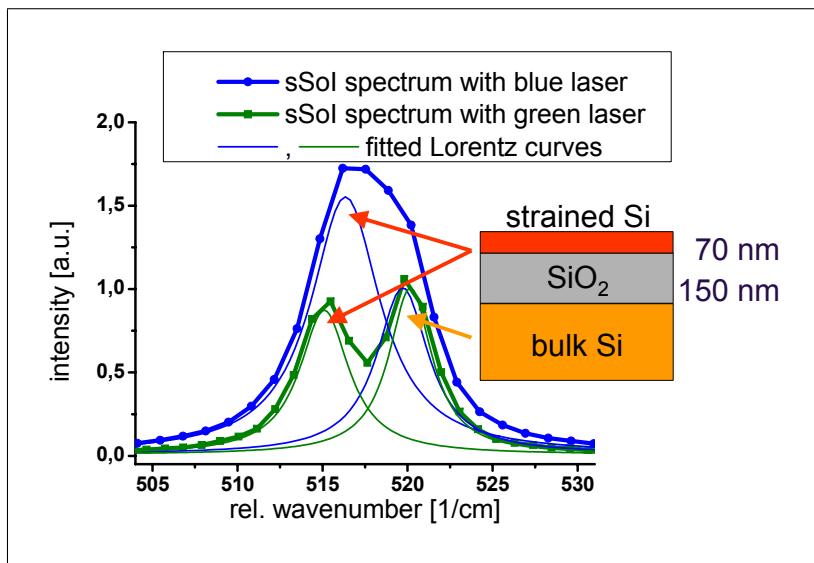
Figure 2.9.: Raman spectra of sSoI sample with blue (488 nm) and green (532 nm) laser excitation. Fitted bulk and strained silicon peaks are displayed, the inset shows the sample's structure.

In figure 2.10 a similar sample was measured, this time with a much thinner strained silicon layer (about 15 nm). Again blue and green laser light was used,

but this time with different microscope objectives: one with a magnification of 50x and a numerical aperture of 0.45 and one with a 100x magnification having a numerical aperture of 0.8. In the original spectra, the strained silicon peak was barely visible as a small shoulder, so in the inset a zoomed view of the fitted strained silicon peak is added. The better collection efficiency of high NA objectives translates directly into an increased Raman peak intensity. Note also the change in peak position which might be a sign for a local surface heating when using the 100x objective with blue laser.
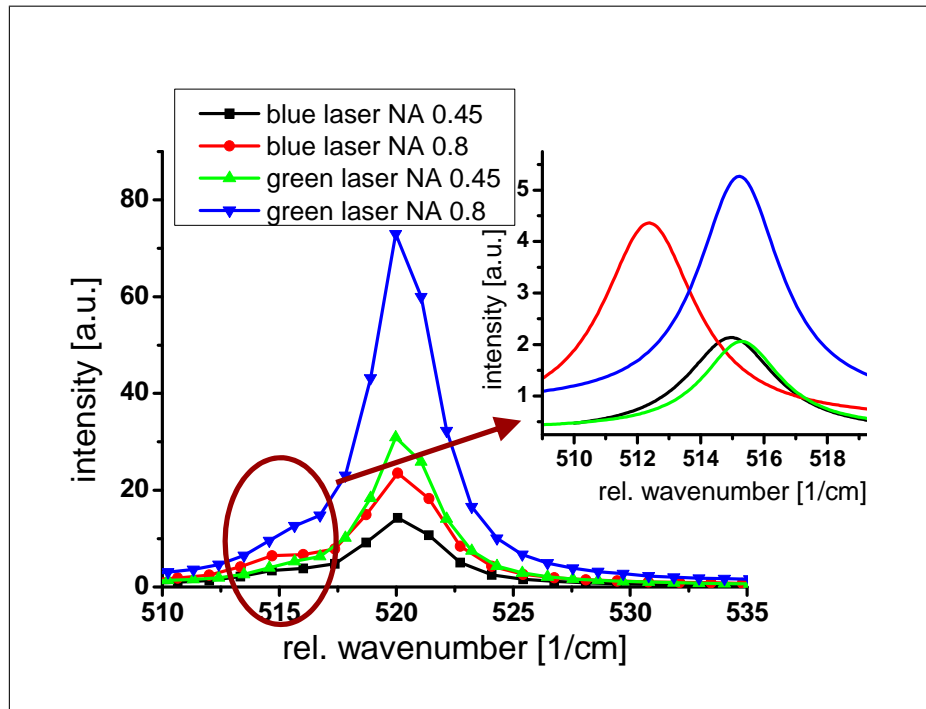
Figure 2.10.: Raman spectra of a sSoI sample with blue (488 nm) and green (532 nm) laser excitation and different objectives. Fitted strained silicon peaks are displayed in the inset as a zoomed view.

The output power of the used laser plays an important role in Raman spectroscopy. In order to make statements about the dependency of the laser power on the Raman spectrum, the three main Raman peak characteristics, the intensity, position and width were looked at with varying laser output power. Again a sSoI sample was used, so two peaks, one from the surface strained silicon layer and one from the bulk silicon substrate were analyzed. Figure 2.11 shows the change in intensity, position and width of the fitted strained silicon peak (red) and the bulk silicon peak (black). All data show a linear behavior as expected from Raman radiation being a first-order scattering process. Thus the scattering

intensity is proportional to the incident laser power [48]. An interesting result is the greater slope of the strained silicon peak position compared to the bulk silicon peak position. This is a consequence of the surface layer being exposed to the majority of laser power and thus experiencing higher peak shifts caused by a changed crystal lattice.
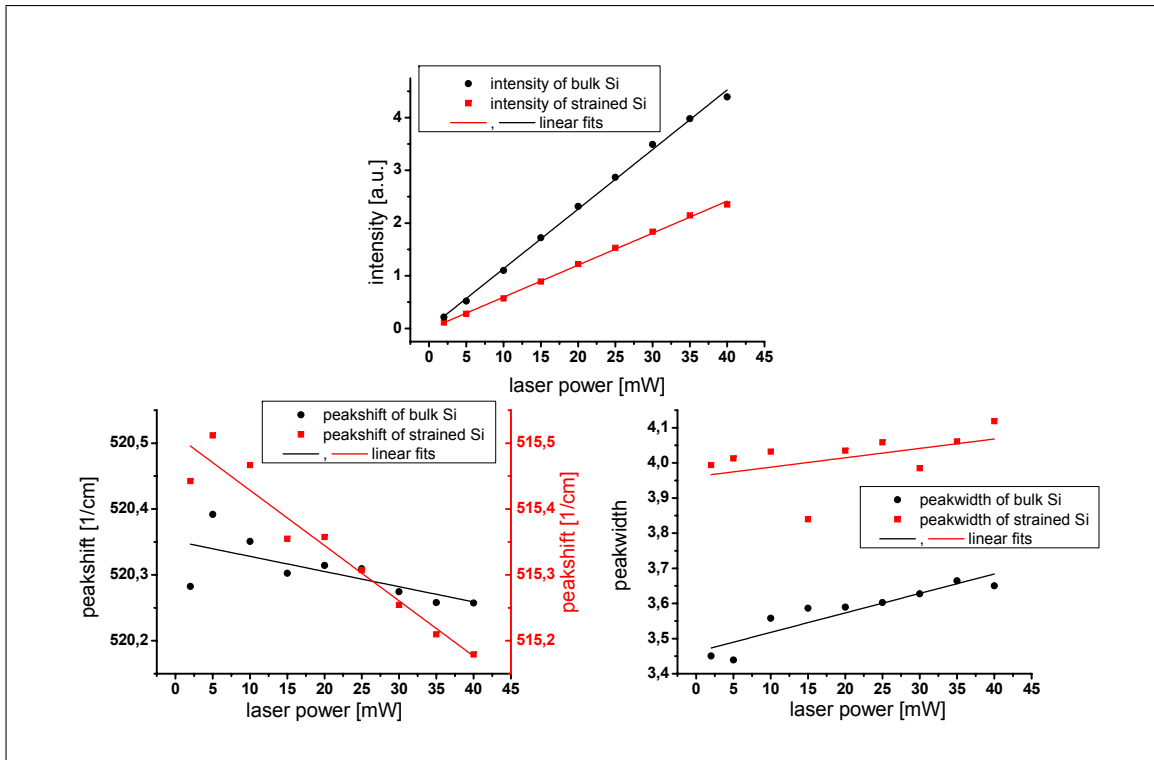

Figure 2.11.: *Top:* Fitted peak intensity of bulk silicon substrate (black) and strained silicon surface layer (red), *Left:* fitted peak position, and *Right:* fitted peak width versus incident laser power.

Changes in Raman intensity or peak frequency also depend on the laser focus depth and position in z-direction. Figure 2.12 presents the result of measurements on a simple silicon sample where the microscope stage was moved in z-direction over a range of 40 µm. The red laser with 632 nm excitation was used together with an objective with a numerical aperture of 0.8. The peak intensity plot represents the product of the focused laser beam shape and the absorption in the silicon. The curve of the fitted peak position changes slightly when the focus lies next to the samples surface, reasons for this deviation will be treated in section 2.4.4. Because the microscope stage could only be moved in steps of 1 micron, additional measurements were performed with the help of the piezo

in the lower scanner. By this the focus could be changed in nanometer steps, these results are plotted in the insets.
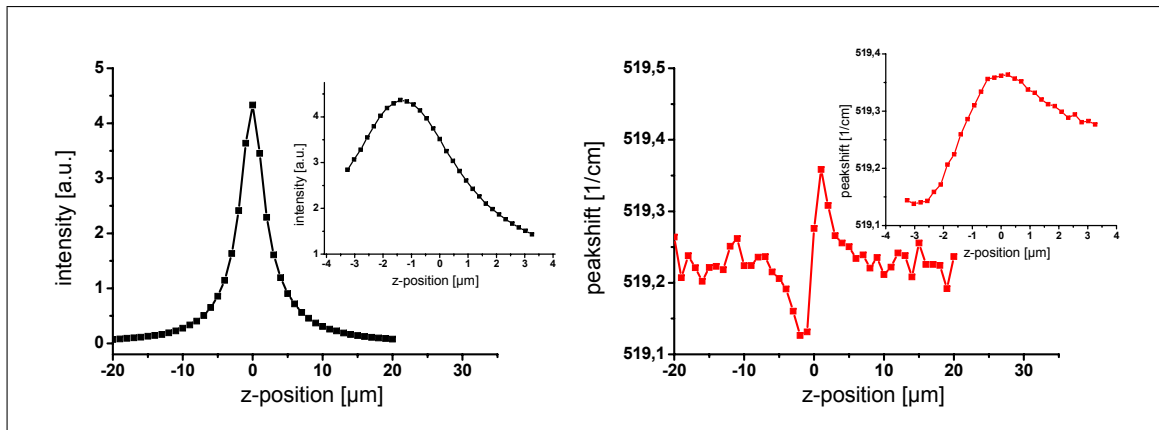

Figure 2.12.: *Left:* Plot of silicon peak intensity versus vertical position of microscope stage, *Right:* plot of silicon peak position versus vertical position of stage, insets give a detailed view of the near-surface region obtained with the help of the scanner's z-piezo.

Linescans

In semiconductor industry not only absolute values for material parameters, but in most cases relative statements are needed. So an important issue is to look at Raman spectra recorded from different points on the sample. The simplest way to do this is performing a linescan by just moving the sample under the laser spot and recording Raman spectra at each scanning point. The shape of the laser spot hereby influences the lateral resolution, i.e. the ability to resolve small changes along scanning path.

A typical linescan with blue laser excitation can be seen in figure 2.13. Here a structured sSoI sample was used with decreasing strained silicon line widths. The intensity as well as the strained silicon peak frequency are plotted versus the scan position. The location of the strained silicon lines can be attributed to the maxima in the intensity curve. The thinner the trenches become, the more difficult it is to get enough intensity from the strained silicon peak to measure a clear value for intensity and peak position. The curve of the peak frequency shows, that in between the strained silicon lines, the signal shifts to higher wavenumbers. This can be described by a relaxation of the stress at the line edges. The lowest wavenumbers, i.e. highest stress values, can be found in the middle of

the lines. Note that the stress free silicon peak frequency lies at about 520.5 cm^{-1}, so the strained silicon material is tensile stressed.
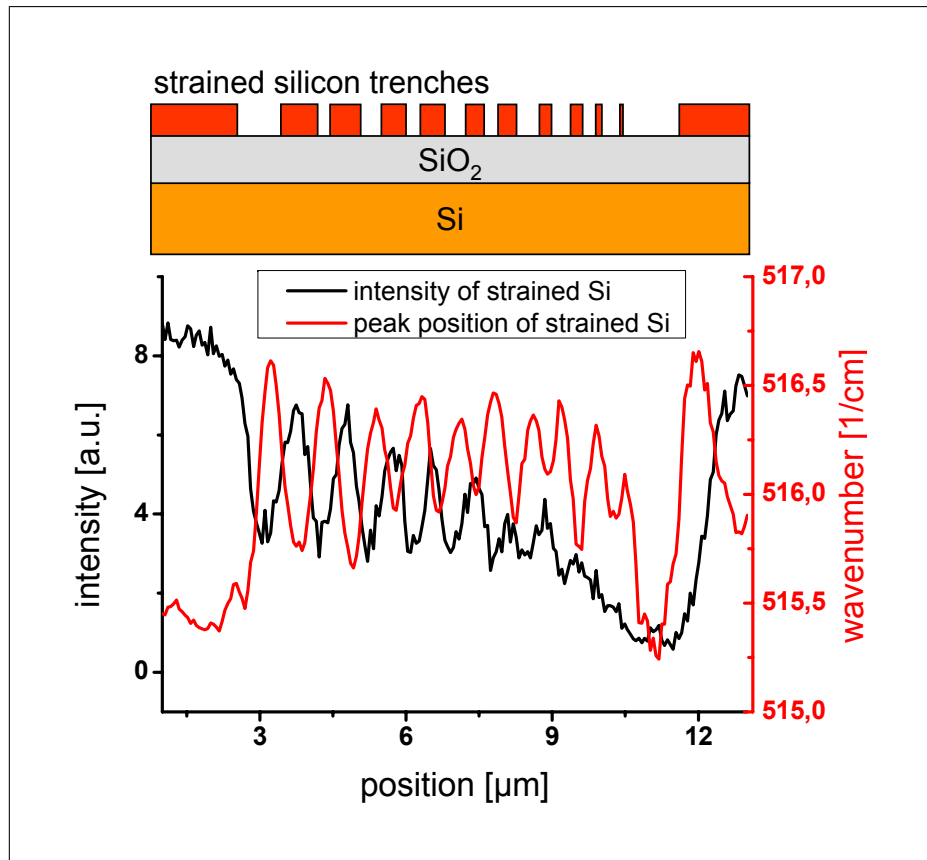

Figure 2.13.: Peak intensity and peak position of strained silicon trenches versus scan position. Scheme of the used sSoI sample above.

A similar linescan was done on a sample with strained silicon pads on a silicon substrate. With a rectangular shape they have a spacing of about 500 nm in horizontal direction and 250 nm in vertical direction. So two linescans were made to study the resolving power of these structures. In the left picture of figure 2.14 there is the horizontal scan where the periodicity of three strained silicon pads can be clearly seen in the peak intensity, position and width curve. Again the effect of stress relaxation at the structure edges becomes visible. When looking a the right picture of figure 2.14, which relates to the vertical linescan the structure's periodicity is hardly seen in the intensity curve and not visible at all in the peak position curve, but it can be resolved in the change of the peak width. This shows that different information in Raman spectroscopy can be used to get information of otherwise invisible changes.
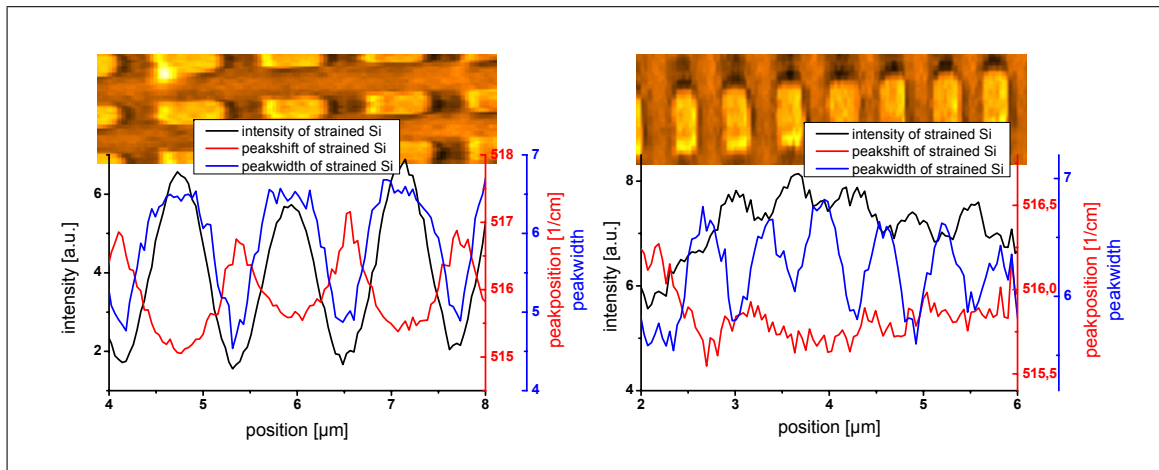
Figure 2.14.: Fitted strained silicon peak intensity (black), pea position (red) and peak width (blue) versus scan position, *Left:* horizontal scan over sSoI pads with a spacing of 500nm, *Right:* vertical scan over sSoI pads with a spacing of 250nm. The insets show the sample topography obtained by AFM.

The importance of peak fitting

At this point some words about extracting the information in a linescan from several Raman spectra should be dropped. Two things must be kept in mind. At first, some information about the sample should be known, for example: which materials were used and where are the related Raman peaks in the spectrum. Secondly the Raman spectra have to be deconvoluted by some kind of fitting process, especially if several peaks overlap.

Take for example the Raman spectrum from a sSoI sample, with two adjacent peaks at 516 cm^{-1} and 520 cm^{-1} in figure 2.15. If the raw intensity data from the two spectral positions are used and plotted as a linescan we achieve the curves on the left side of the picture. On the other hand, if two separate peaks are fitted and this information is used in the linescan, we receive the curves on the right side. Comparing both result it becomes clear that the distribution of the red strained silicon curve is very similar, but the black curve from the bulk silicon substrate peak has a different characteristic. This happens because the much smaller bulk silicon peak at 520 cm^{-1} is dominated by the strained silicon peak at 516 cm^{-1} which makes up the biggest part of the measured Raman spectrum. The Origin[2] script developed for fitting multiple peaks in measurements with a high number of spectra is presented in the appendix A.1.

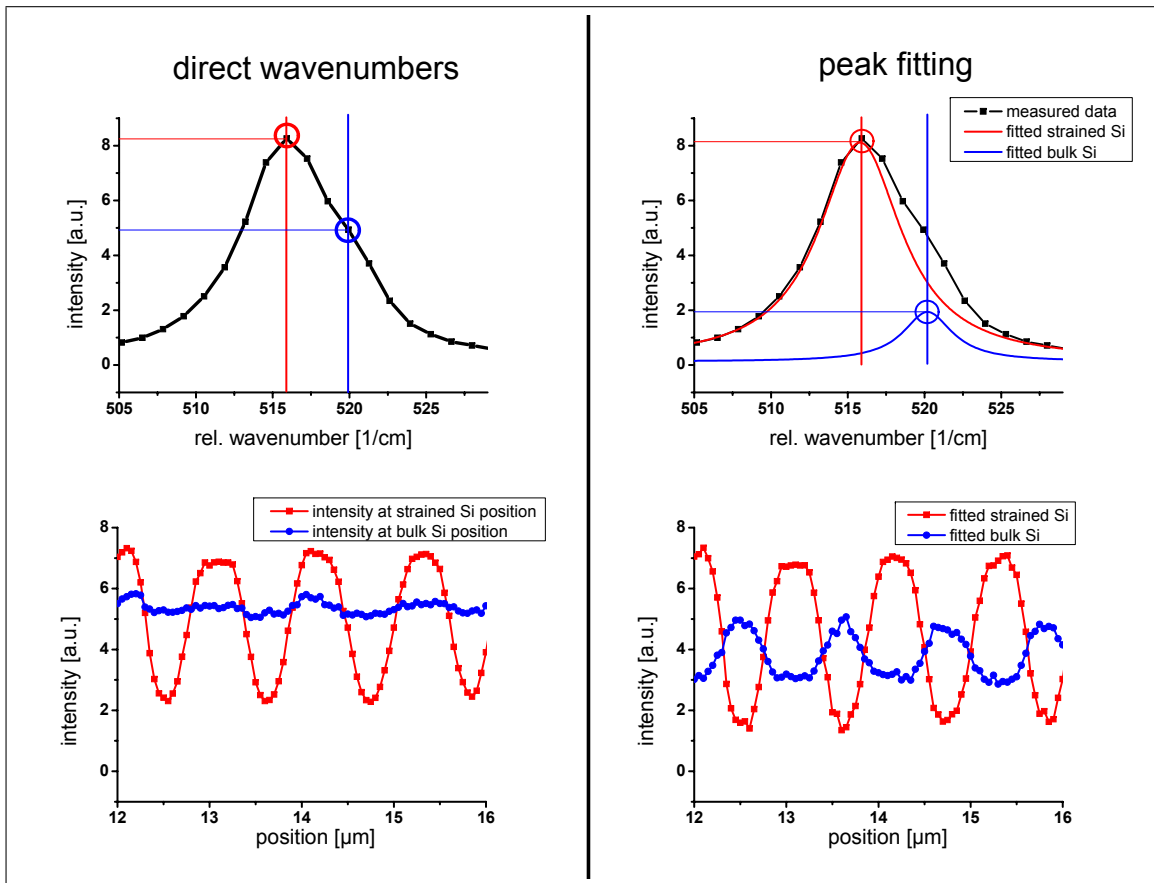[2]ADDITIVE GmbH, Deutschland, http://www.additive-net.de

Figure 2.15.: *Top Left:* Measured Raman spectrum from sSoI sample, intensities taken directly from spectral position and *Bottom Left:* plotted into a linescan. *Top Right:* Measured Raman spectrum fitted with two Lorentz curves and peak fit information used in *Bottom Right:* a linescan for correct distribution of strained and bulk silicon along the scan.

Resolving power

What is the practical limit on lateral resolution? This question leads to the next measurement where a linescan was done on a special test sample containing strained silicon lines with decreasing width. The specific lines size was measured by SEM beforehand. In the lower section of figure 2.16 a sketch of the used sample is shown and the different line dimensions are added. In the upper section the fitted peak intensity and position of strained silicon is plotted versus the scan position. The dashed boxes between the lines mark positions where the fit routine gave no results due to the absence of a sufficient strained silicon signal intensity. The black intensity curve shows an increase at the line edges,

where the left and right edge can be distinguished up to the third line. Below 500 nm linewidth the lower plateau on the strained silicon line is no longer visible, both edge induced intensity effects add up to a higher value. Regarding the red curve showing the peak position, the already mentioned relaxation effect at the line edges is visible. The induced strain for the layer can only be sustained for wide lines, the narrower they become, the more they relax, i.e. shift to higher wavenumbers (keep in mind the the stress free value at 520.5 cm^{-1}). Interesting is the somewhat unexpected behavior on the thinnest line, which seems to have a higher stress level than the line before. This might be attributed to the etching process which could induce additional stress in the thin lines.
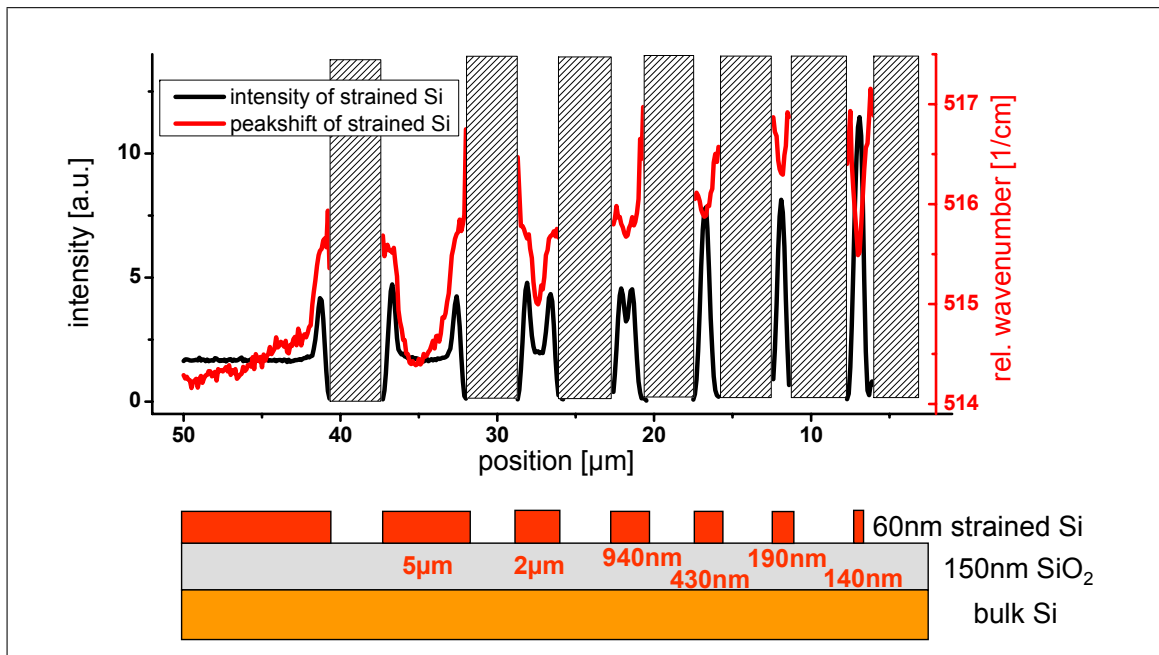
Figure 2.16.: Fitted strained silicon peak intensity (black) and peak position (red) versus scan position, dashed boxes mark regions with insufficient strained silicon Raman signal. Below is a sketch of the structured sSoI sample with added line widths obtained by SEM.

Raman maps

Apart from linescans, obtaining two-dimensional maps is the second important measuring method. A simple mapping was done on an AFM calibration sample consisting of a silicon - silicon oxide structure with etched pitches. The spectra recorded at every scanning point were fitted, and then plotted into a two-dimensional map. The left side of figure 2.17 shows the intensity map of the silicon peak. We get highest values for the groove edges and lowest when the laser beam is directly on the silicon groove. This is somewhat irritating because one might expect a higher Raman intensity when there is no silicon oxide between the spot and the silicon substrate. But the absorption losses in the silicon oxide layer are almost negligible, on the contrary the oxide layer serves as an anti reflexive coating which lets more Raman light into the objective. In the right side of the figure the peak position is plotted. Despite only small variations, stress free regions in the grooves and between them can be recognized by green color, while at the edges we have tensile (blue) and compressive (red) stresses.
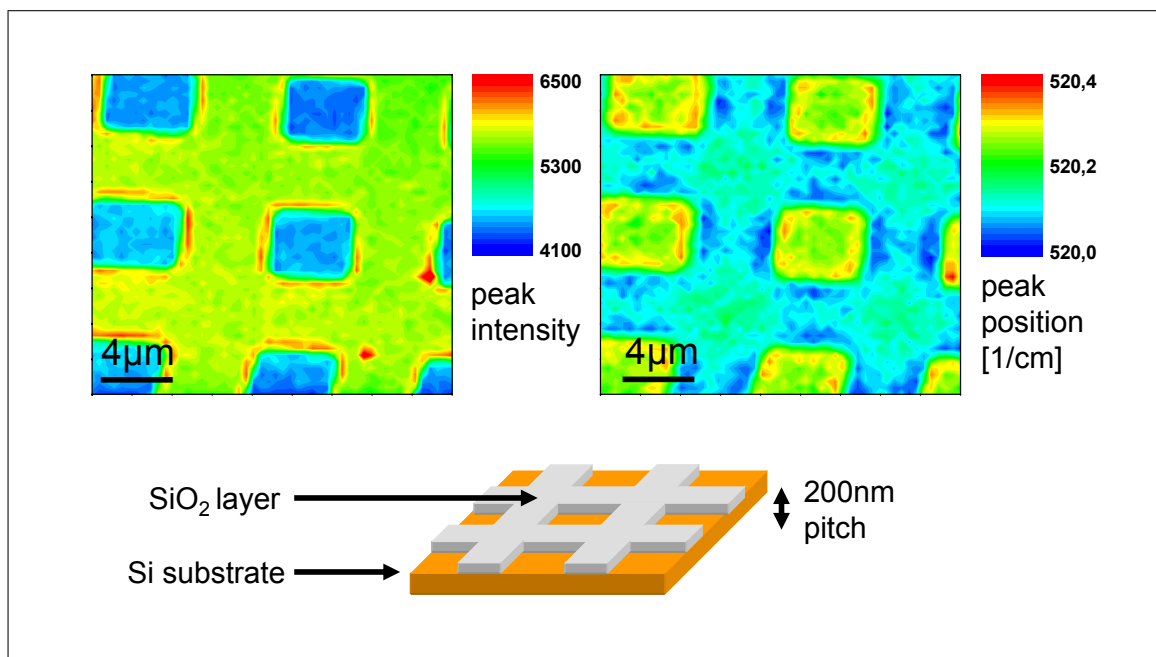
Figure 2.17.: *Left:* Silicon peak intensity mapping and *Right:* peak position mapping on structured silicon oxide test sample, sketch of the used sample below.

The picture becomes much more complex when performing a two-dimensional Raman scan on a strained silicon pad. Figure 2.18 shows the analysis of the Raman mapping together with single spectra taken at specific points in the scanned area. The data in the maps are related to the strained silicon Raman peak, the brown regions relate to points where no strained silicon is present, hence no information comes out of the fit. Peak intensity (A), peak shift (B) and peak width (C) all show different information. Comparing the spectra at points (1) and (2), the appearance of the strained silicon peak at around 514 cm^{-1} comes along with the decrease of the bulk silicon peak at 520 cm^{-1}. Remarkably the intensity increases and the peak position decreases at the lower and upper pad edges (point (3)) which might be a sign for an asymmetric strain distribution or a polarization dependent behavior. At the pad corners (point (4)) the peak width has its biggest values, this is related to the many different stress states at the corners resulting in a broad Raman peak.
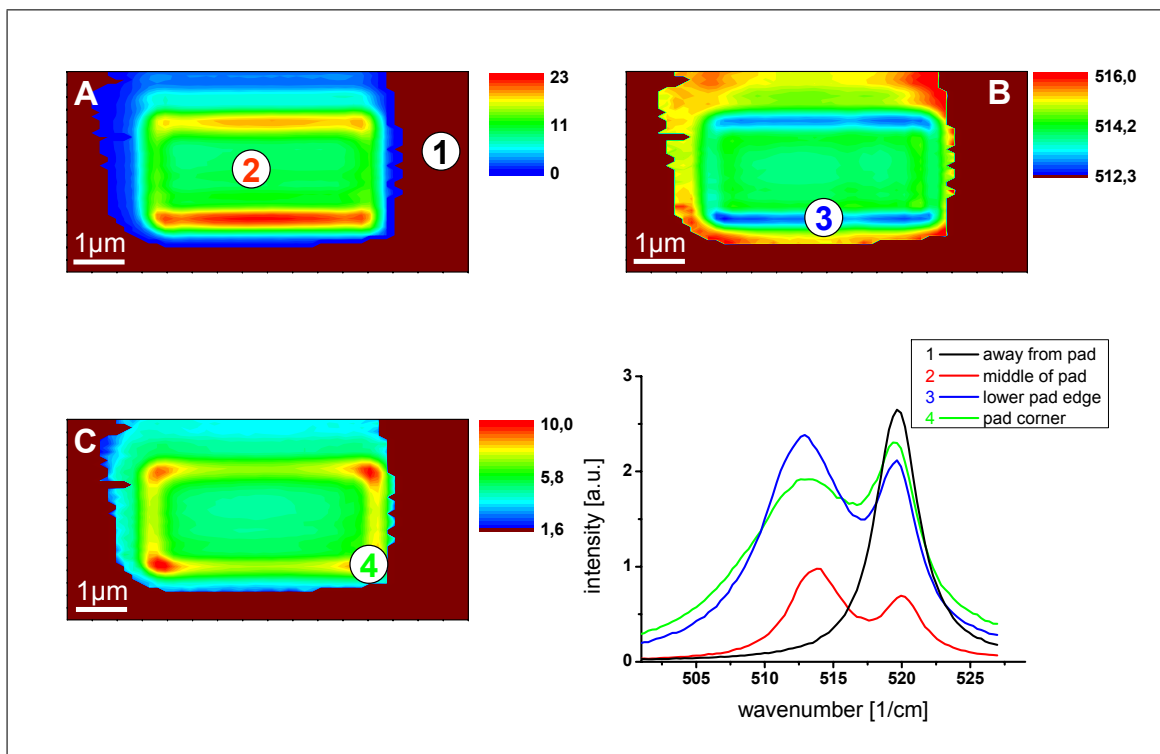
Figure 2.18.: Raman mapping over a sSoI pad showing *A:* strained silicon peak intensity, *B:* peak position, and *C:* peak width. *D:* Single spectra at specific scanning points (1) - (4).

Polarization and scan direction

The used lasers all provide linearly polarized light. With the use of a lambda half waveplate directly behind the laser output, the direction of the electric field vector can be rotated to get different polarization directions on the sample. In addition, with the use of polarization filter films in front of the detector it is possible to measure only certain portions of the Raman signal.

But even without polarizing filters there are polarization dependent elements in the beam path. The biggest influence here comes from the diffraction grating. Light polarized parallel to the grating grooves is diffracted much more efficiently than light polarized perpendicular to the grooves. This effect is demonstrated in figure 2.19 where the intensity of the silicon Raman peak was plotted versus the incoming laser polarization.
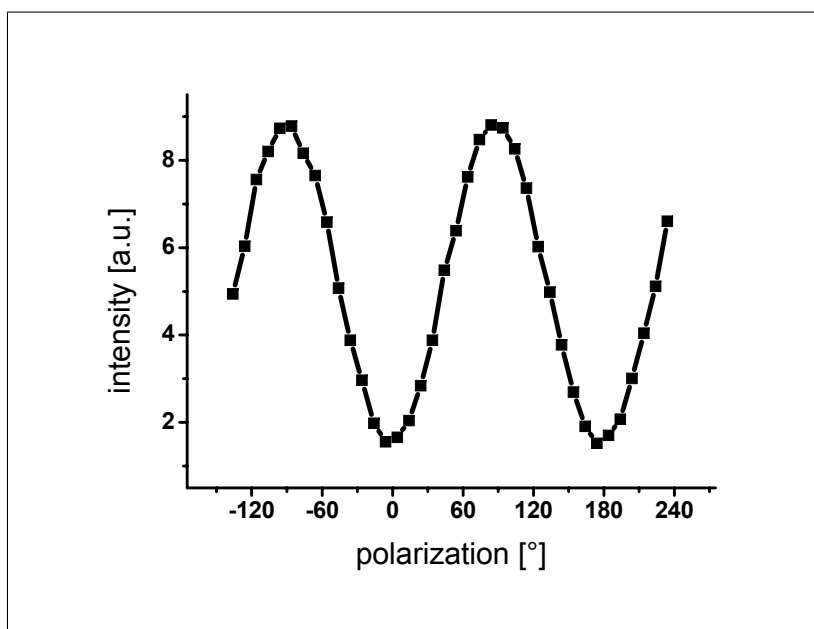
Figure 2.19.: Plot of silicon peak intensity versus laser polarization. The signal is suppressed when light is polarized perpendicular to the grating grooves.

There is also an influence of the sample on the polarization of the Raman signal. When dealing with crystalline samples the lattice might rotate the incoming polarization. This doesn't apply to every peak from the silicon Raman spectrum, but for example to the strongly polarized first order longitudinal optical phonon (1 LO), the main peak at 520 cm^{-1}. Other, less prominent peaks, for example the second order transversal acoustic phonon (2 TA) at 300 cm^{-1} or the second order

transversal optical phonon (2 TO) don't rotate the incoming laser polarization when the sample is rotated. This is shown in figure 2.20 where a polar diagram is used for better visualization. Mentionable is the 2θ shift for the 1 LO peak, this means that if the sample is rotated by α we get a Raman signal rotated by 2α compared to the incident polarization, i.e. rotating the sample by $90°$ would not change the polarization state.
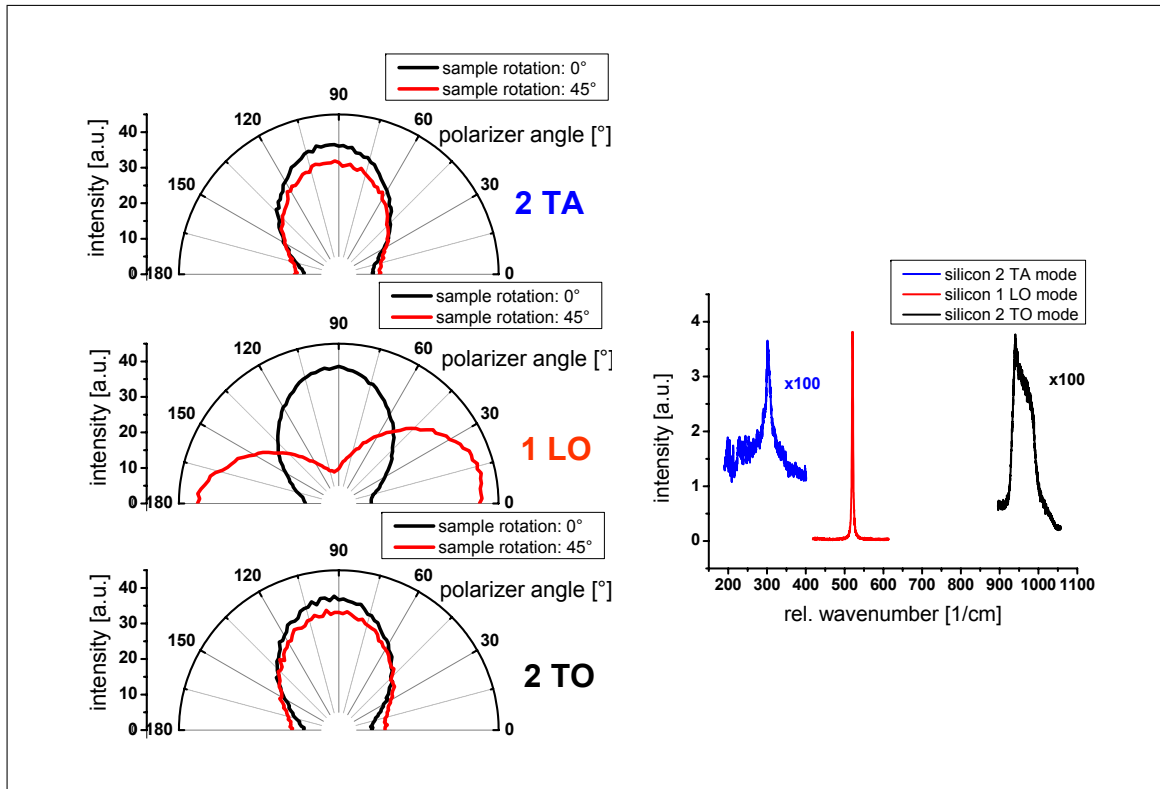

Figure 2.20.: *Top:* Polar diagram of the 2 TA silicon mode intensity versus incoming laser polarization with the sample rotated by 45 degrees, *Middle:* same measurement with the intensity of the 1 LO silicon mode, and *Bottom:* with the 2 TO silicon mode. *Right:* Extended Raman spectrum of silicon sample showing all three Raman modes, intensity multiplied for the second order peaks.

The result of a polarizing filter film before the detector is presented in the next experiments. In figure 2.21 again a polar diagram is used to better visualize the polarization dependence. The black curve without polarizing filter shows the known two-lobe shape with a non-zero waist, which means that the grating does not suppress the perpendicular polarization completely. When introducing the filters parallel or perpendicular in the beam we suppress the related polarizations completely, this can be seen in the waists with zero signal intensity.
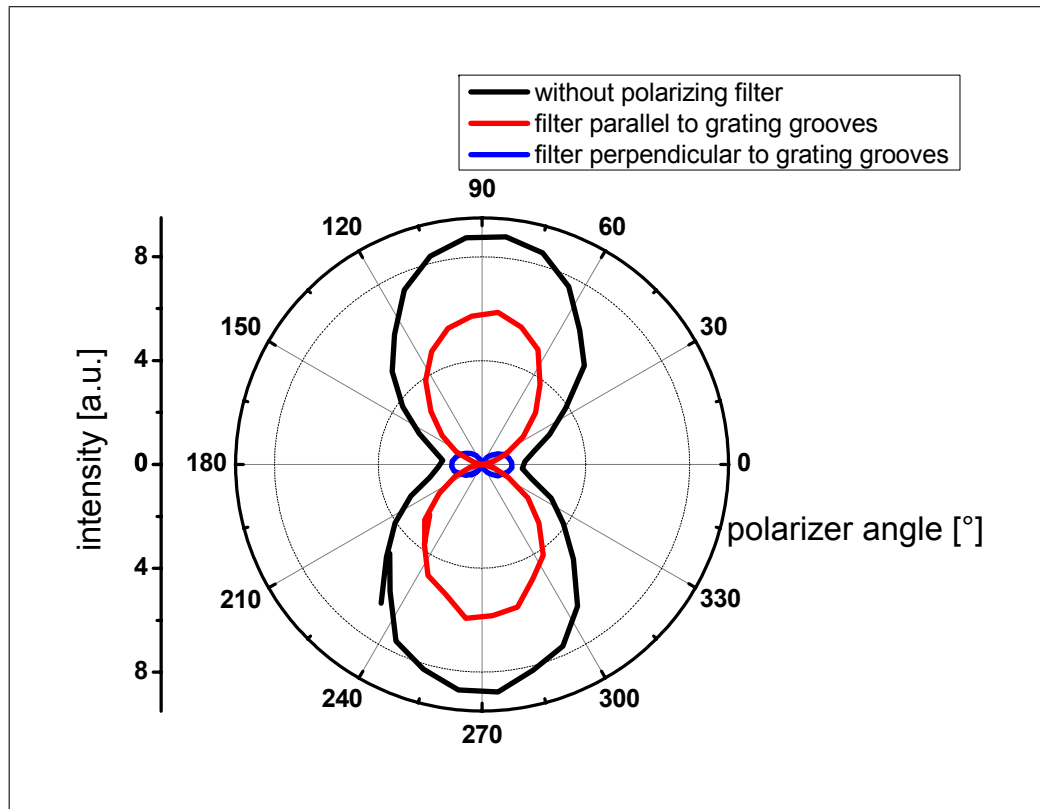
Figure 2.21.: Polar diagram showing the intensity of a silicon peak versus the angle of incoming polarization. Red and blue curve belong to measurements with a polarizing filter film before the diffraction grating.

This behavior is only true for Raman scattered light. For comparison, the polarization influence on Rayleigh scattered light as well as on directly reflected light from a laser plasma line is presented in figure 2.22. The left plot for the Rayleigh line is similar to the Raman plot but with a less defined polarization, the plasma line plot on the right side shows no polarization dependence, this light is completely unpolarized.
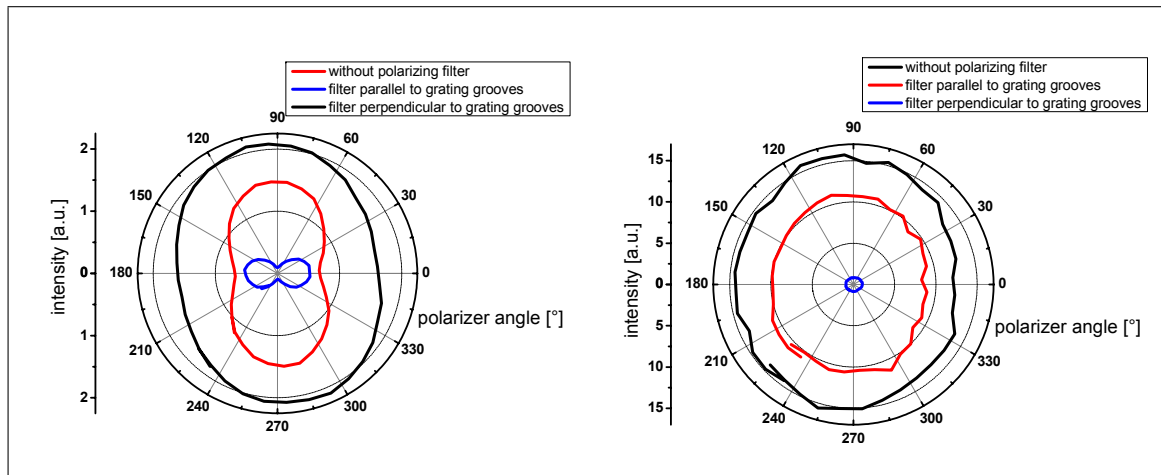
Figure 2.22.: *Left:* Polar diagram of the intensity of the Rayleigh line versus the incoming laser polarization, *Right:* intensity of a laser plasma line versus the incoming laser polarization, red and blue curves show the measurements with introduced polarizing filter films.

Topographic features have a significant impact on Raman spectra. The next experiment was done to show this influence on the intensity of Raman peaks. Linescans were performed over the breaking edge of a sSoI sample. The scanning direction as well as the polarization of the incident light was changed. The measurements are summarized in figure 2.23. Pictures (A) and (B) show the experiments where the linescan was done horizontally over the samples edge, (C) and (D) show the results of the vertical linescans. Horizontal laser polarization was used in (A) and (C), vertical polarization was used in (B) and (D). The actual sample edge is visualized by the black vertical lines in the diagrams, and the airside of the linescan is also labeled. The sketches above each diagram illustrate the scanning direction with the black arrow, and the laser polarization with the blue arrow. The diagrams show the fitted intensity of the strained silicon surface layer and the bulk silicon substrate, as well the peak shift of the strained silicon compared to the unstressed value of about $520 \, \mathrm{cm}^{-1}$.

The most interesting effect is the increase of peak intensity when the laser spot is positioned at the very edge of the sample, in fact the intensity maxima occur when the spot is positioned next to the sample, in air. This is most likely to the increased silicon surface at the side of the sample, where the laser spot 'sees' much more material where Raman scattering can take place. An other possibility is the creation of wave guide modes in the silicon oxide between the strained silicon and the silicon substrate [27]. This only happens when the laser
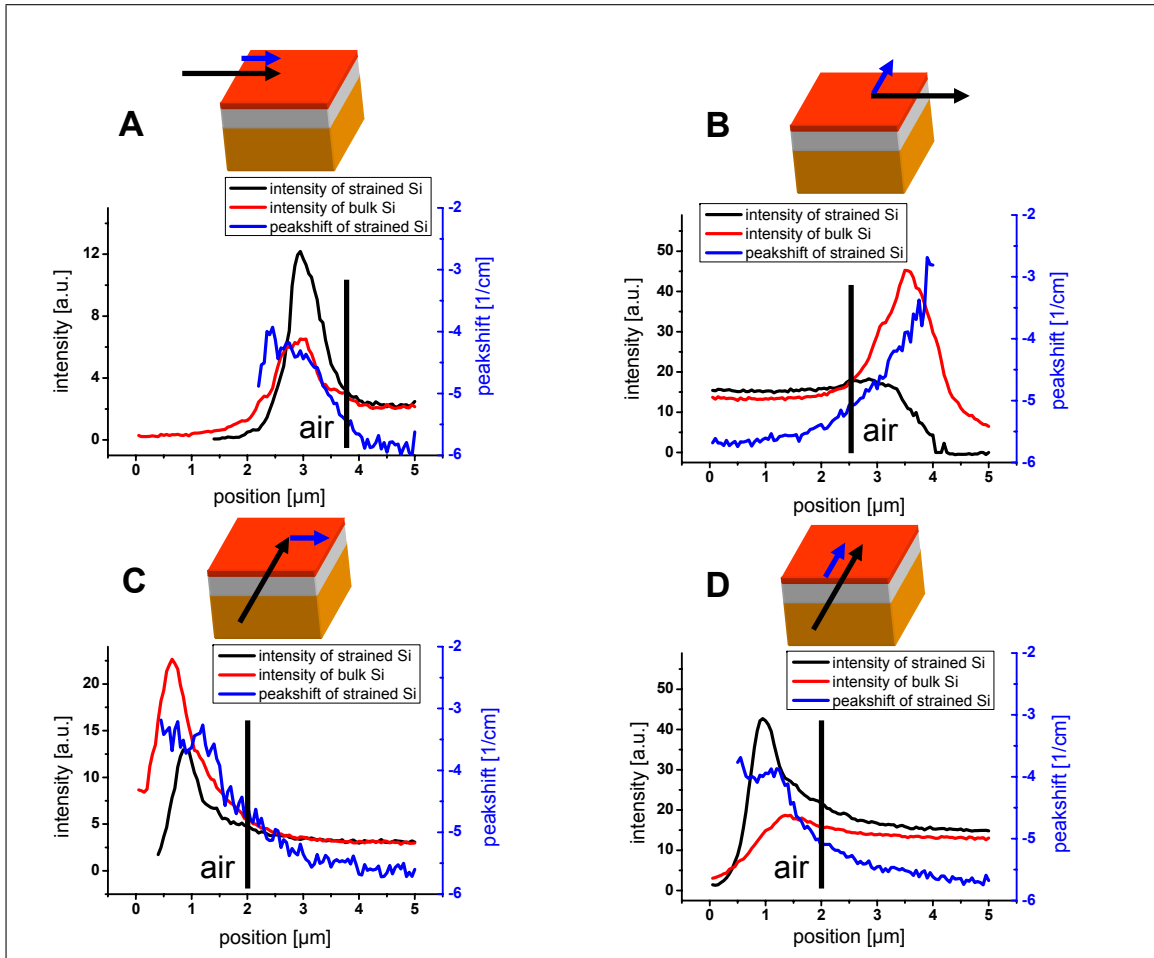
Figure 2.23.: *A:* Horizontal linescan over sSoI sample edge with laser polarized horizontally, *B:* horizontal linescan with laser polarized vertically, *C:* vertical linescan with laser polarized horizontally, and *D:* vertical linescan with laser polarized vertically. Included in the graph are the intensities of the strained and bulk silicon as well as the peak shift from the strained silicon. Sketches illustrate the sample structure, scan direction and laser polarization.

polarization is aligned parallel to the linescan edge. These cases are represented by figure 2.23B and figure 2.23C. Here the strained silicon layer peak is strongly increased, and its red curve peaks at much higher values than the black curve from the bulk silicon.

The blue curve showing the strained silicon peak shift, is mostly unaffected by the scan direction and laser polarization and always shows a relaxation of stress towards the sample edges, which can be seen by the decreasing peak shifts.

2.4.2. Capability of the tool and diversity of measurements

In the following, several experiments on different materials were performed, to show the usefulness of the tool and its range of applications. Statements about the stress state, mechanical stability or grain orientation can be derived from Raman measurements.

SiGe islands

Small islands of silicon-germanium were grown on a silicon substrate [28]. The corresponding Raman spectrum as well as a microscope overview of the SiGe islands can be seen in figure 2.24. The fitted peaks for the SiGe island signal and the silicon substrate signal are shown in red and blue respectively.
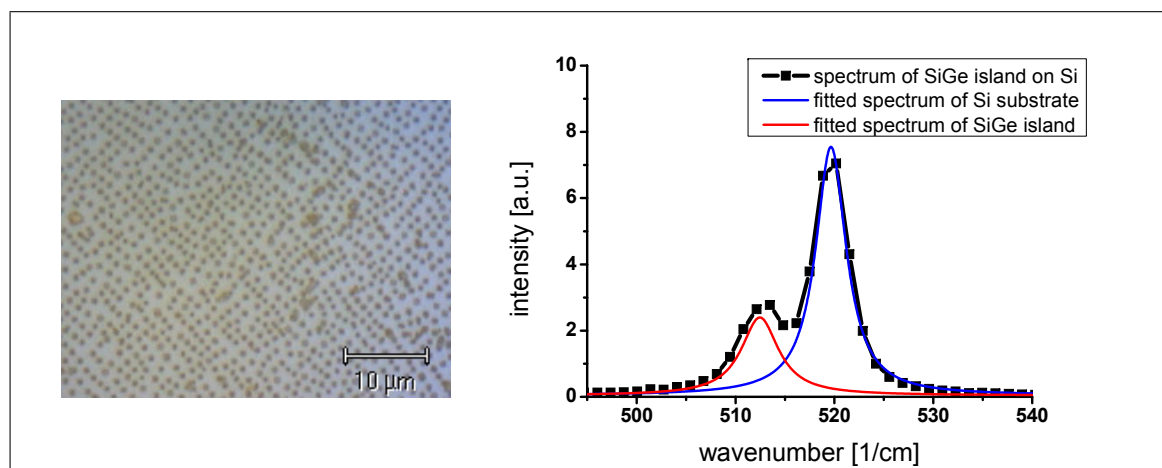
Figure 2.24.: *Left:* Microscope view of SiGe islands on silicon, *Right:* single Raman spectrum showing the signal from the silicon germanium at 512 cm^{-1} and from the silicon substrate at 520 cm^{-1}.

A six µm map was taken with AFM and Raman. The SiGe signal from the islands and the Si signal from the underlying substrate were fitted and analyzed regarding intensity and peak shift. In figure 2.25A the topography is shown, while in figure 2.25B the intensity of the SiGe signal is plotted. The position of the individual islands can be clearly allocated. Additionally, in figure 2.25C a plot of the fitted Si peak shift is shown. Here the influence of the SiGe islands on the underlying substrate is visible. At the locations of the SiGe islands the peak position of the silicon signal deviates from its normal position at 520.2 cm^{-1} and shifts down by as much as 0.6 cm^{-1}. This peak shift can be described by tensile

stress in the silicon substrate induced by the SiGe islands which have a different lattice constant and expansion coefficient [29].
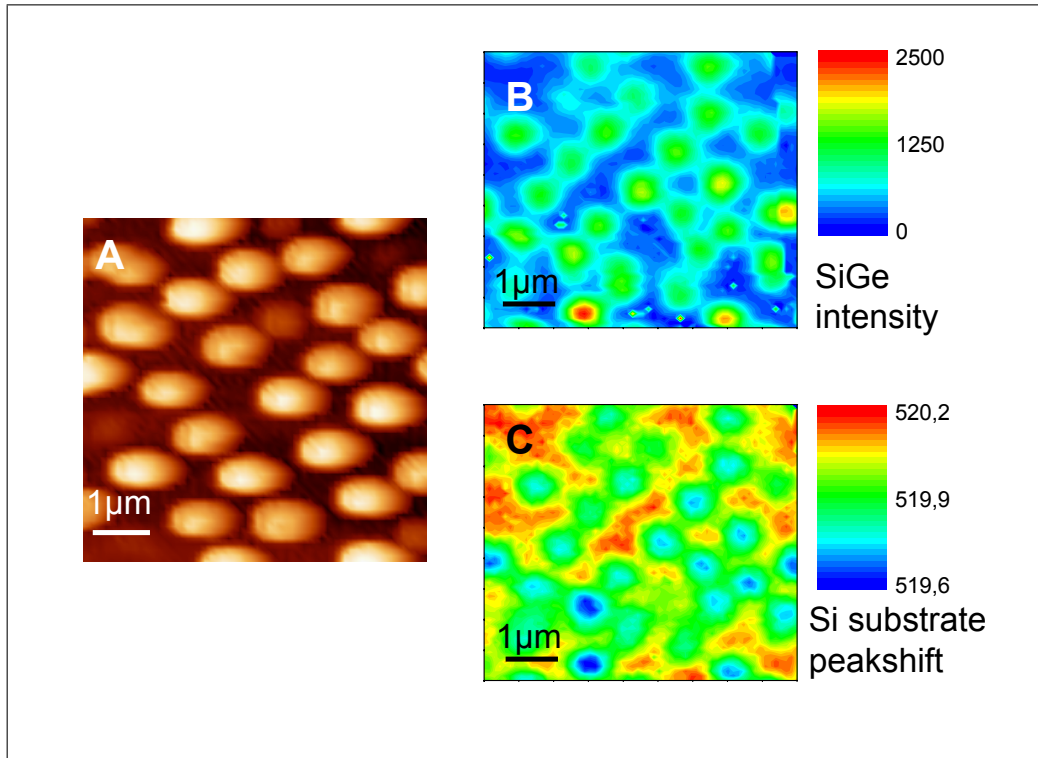

Figure 2.25.: *A:* AFM topography map of SiGe islands on silicon, *B:* SiGe Raman intensity showing the allocation of the SiGe islands, *C:* Si Raman peak position showing the stress effect of the SiGe islands on the underlying silicon substrate.

Silicon nanowire

A different application of stress measurements with Raman spectroscopy lies in testing the mechanical stability of small structures. An interesting approach for Tip Enhanced Raman Scattering is using silicon nanowires attached to an AFM tip. The nanowires have a small half-sphere gold droplet on the top which can be used to enhance and localize the Raman signal. Details of the process involving these nanowires can be found in the literature [30]. In figure 2.26 a SEM view of the nanowire attached to an AFM tip can be seen, the orange circle denotes the gold droplet.

In the following experiment the tip with the attached nanowire was first held above a surface and in the laser beam to acquire a Raman spectrum. It was then

approached to the sample which caused the wire to break off, and a second Raman spectrum was recorded from the silicon nanowire laying on the sample. On the right side of figure 2.26 the two Raman spectra are shown. After approach the silicon peak position of the nanowire shifts by approximately seven wavenumbers to its stress free frequency at about 520 cm^{-1}. When converting this rather large peak shift to a stress value, it shows that the attached nanowire can sustain up to 3 - 4 GPa of stress.
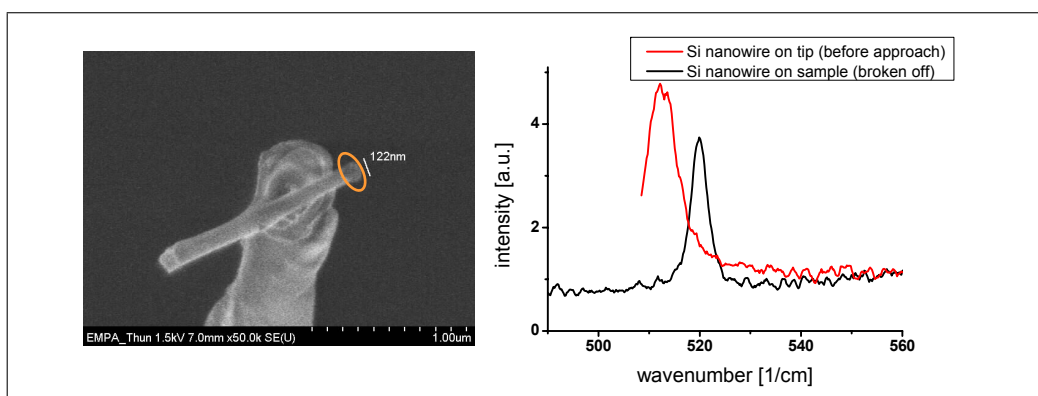
Figure 2.26.: *Left:* SEM view of a silicon nanowire with a gold droplet on top (orange ellipse) attached to an AFM tip, *Right:* Raman spectra showing the nanowire's silicon peak shift. Before the tip approach (red curve) the nanowire is strongly stressed and thus the peak is shifted. After approach, the nanowire breaks off and can relax, resulting in the stress free silicon peak position at 520 cm^{-1} (black curve).

PZT measurements

An interesting field of materials science deals with piezo resistive samples. Raman spectroscopy might be used to make statements about individual grains in the material or, more interestingly, about different electrical domains. A 10 micron AFM map was taken on a PZT sample. PZT is the abbreviation for lead-zirconate-titanate ($Pb[Zr_xTi_{1-x}]O_3$) , a material used for sensor applications, material testing and diagnostics. The AFM map can be seen in figure 2.27. Also shown is the area of the Raman map which was taken afterwards, as well as the location of an individual grain and some parallel structures which seemed to be electrical domains. Figure 2.28 then shows a Raman spectrum of one of the PZT Raman peaks used for peak fitting. The peaks intensity, position and width is plotted in different Raman maps. All three plots give different information

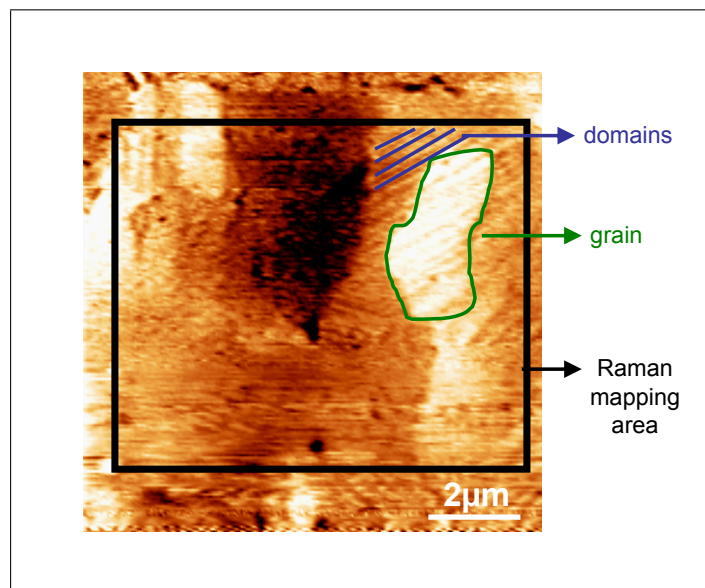which shows that Raman might be a good tool to analyze these kinds of samples
[31].

Figure 2.27.: AFM map of PZT sample. Individual grain and electrical domains
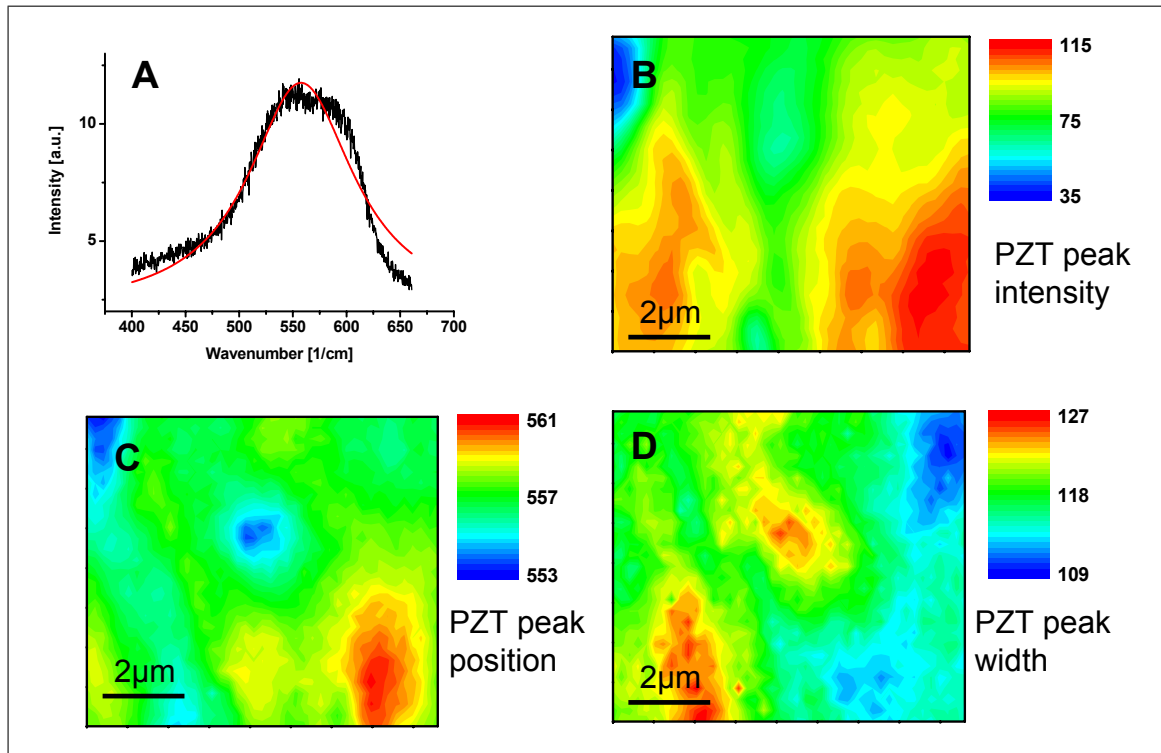   shown.

Figure 2.28.: *A:* PZT Raman peak with fitted Lorentz curve, *B:* Raman peak intensity map, *C:* Raman peak position map, *D:* Raman peak width map, all showing different information.

2.4.3. Industrial chip structures

In this section experiments on real chip structures coming out of the production line are presented. Most of them were ordered to receive information about the stress state at specific sample positions or to compare different process steps in terms of material stress.

STI fill comparison

The process of filling the etched silicon trenches with a dielectric is a key step in semiconductor industry. Three different filling procedures were compared by Raman spectroscopy. Raman linescans were made on wafers processed by SOG (Spin On Glass), HDP (High Density Plasma) and HARP (High Aspect Ratio Process) [32], respectively, at a recognizable sample position. A microscope view of the area is shown in figure 2.29 together with a zoomed view and the position of the Raman linescan represented by a red line.
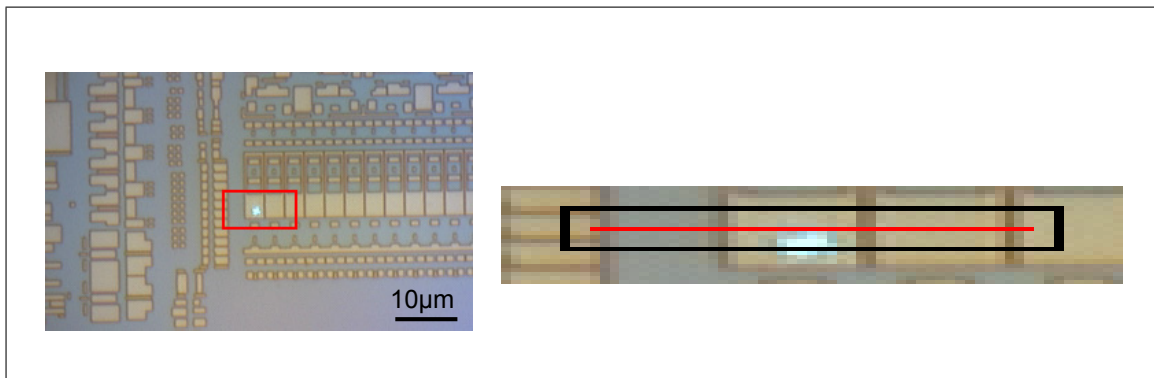
Figure 2.29.: Microscope view of the chip position where the Raman linescan was taken. White regions represent silicon and blue regions represent the trenches filled with silicon oxide.

The silicon intensity and peak position plots are shown in figure 2.30. A partial map from an AFM measurement is also included. It shows the actual scan position in the diagram. The lighter areas in the AFM map are the trenches filled with silicon oxide and the darker areas represent the silicon regions.
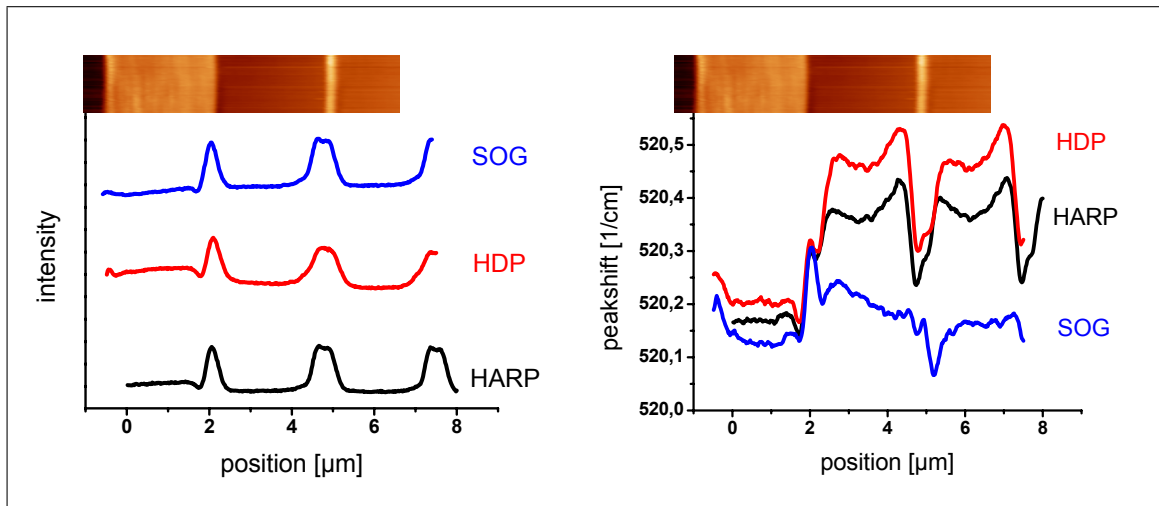
Figure 2.30.: *Left:* Silicon peak intensity versus scan position and *Right:* silicon peak position versus scan position for three different trench fill processes. A partial AFM map showing the topography is included, height difference was about 20 nm.

The intensity curves are offset for better comparison. All three scans show an increased intensity at the trench edges, but otherwise no significant difference is found in the intensity scans. This changes when looking at the peak position curves. Considering the value of 520.2 cm^{-1} as the frequency for stress free silicon, we see that for the case of HDP and HARP we get a compressive stress throughout the scan with very similar values. On the other hand the SOG behaves differently, here we get almost no stress variation.

The same area on the chip was used for the next measurement. This time all three samples were processed by HARP but with different oxide thicknesses of 0 nm, 60 nm and 540 nm. Again silicon peak intensity and position were recorded and plotted versus the scan position, see figure 2.31. The intensity linescans show variation for the different oxide thicknesses. The edge effect resulting in higher intensity at topographic edges is much more pronounced for the cases with non-zero oxide thickness. Additionally, the induced stresses, shown by the high wavenumbers in the peak position linescan in the right picture of figure 2.31, are slightly higher with increasing oxide thickness.
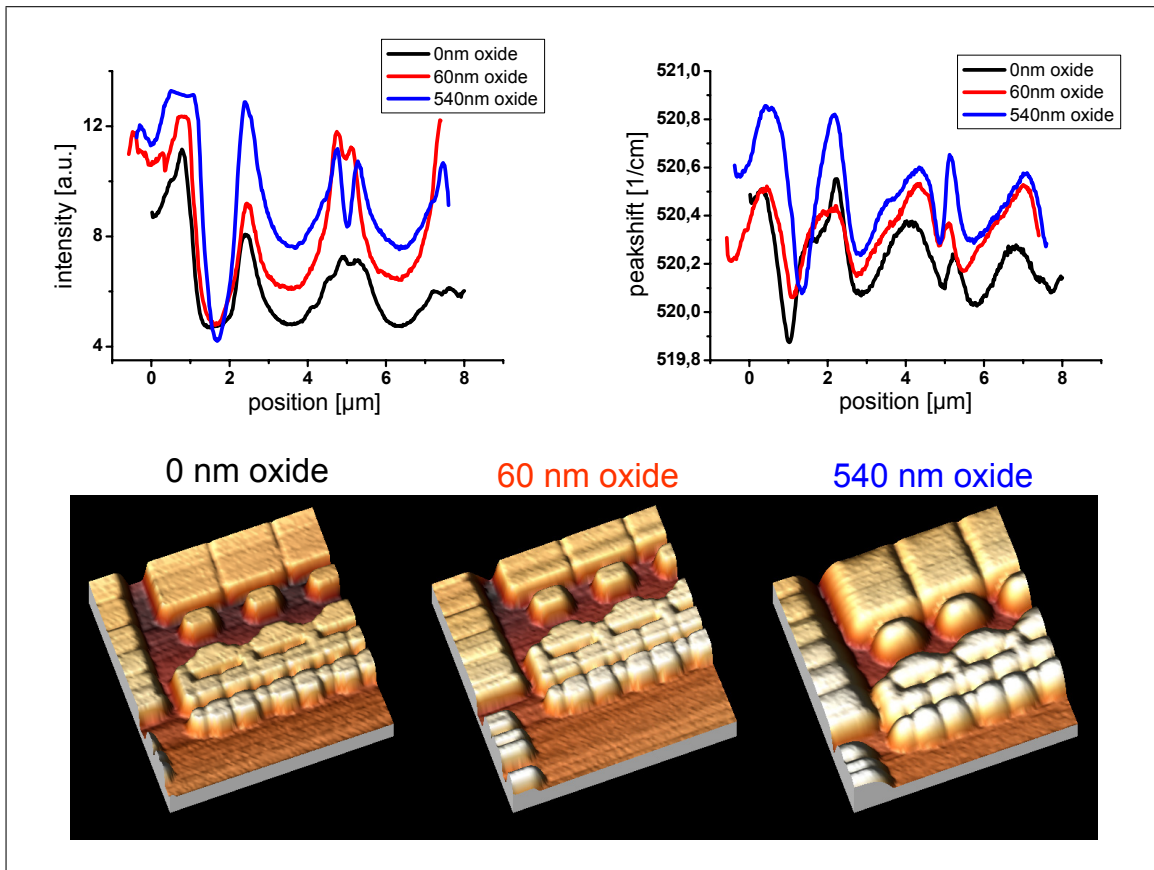
Figure 2.31.: *Left:* Silicon peak intensity versus scan position and *Right:* silicon peak position versus scan position for HARP fill with different oxide thicknesses. Below the respective AFM maps are displayed.

Spine measurements

For a certain process step the problem arose, that the masks used for lithography did not match the underlying structure. A specific question was, if stress was the reason for this and if Raman spectroscopy could be used for verification. Three different tasks were defined. First: what is the stress distribution along the spine, second: are the stress values at the right and left spine edge the same and third: what is the stress distribution along an array pad. The named regions and the linescans resulting from these tasks are visualized in figure 2.32. The spine is a wide area separating the different chips on a wafer and the array pads contain the narrow trenches with the transistor and capacitor elements.
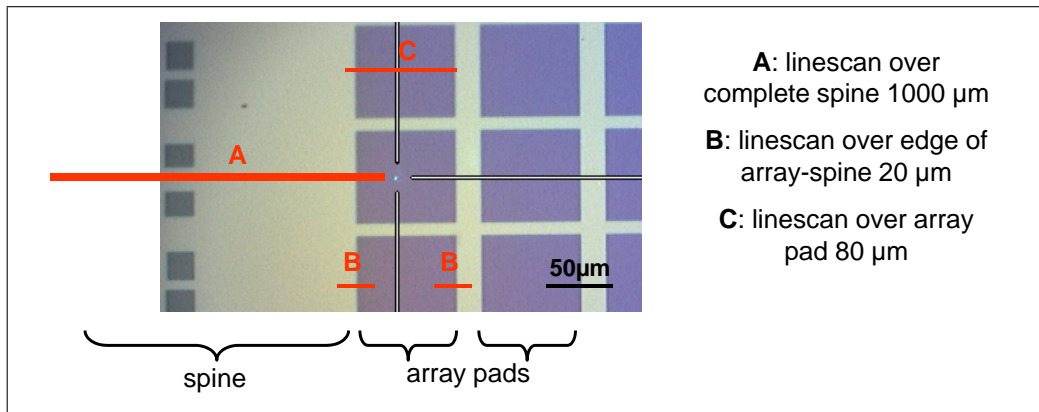
Figure 2.32.: Overview of the spine measurements. White regions stand for silicon areas, purple regions for the filled trenches.

Figure 2.33 shows the result of measurement (A). The silicon peak shift from its stress free value is plotted against the scan position. The blue line marks the stress free state, so that positive values result in compressive stress, while negative values result in tensile stress. It can be seen, that all along the spine the stress is slightly compressive and constant, except for two interrupts where some structured pads happened to be in the scanning path.
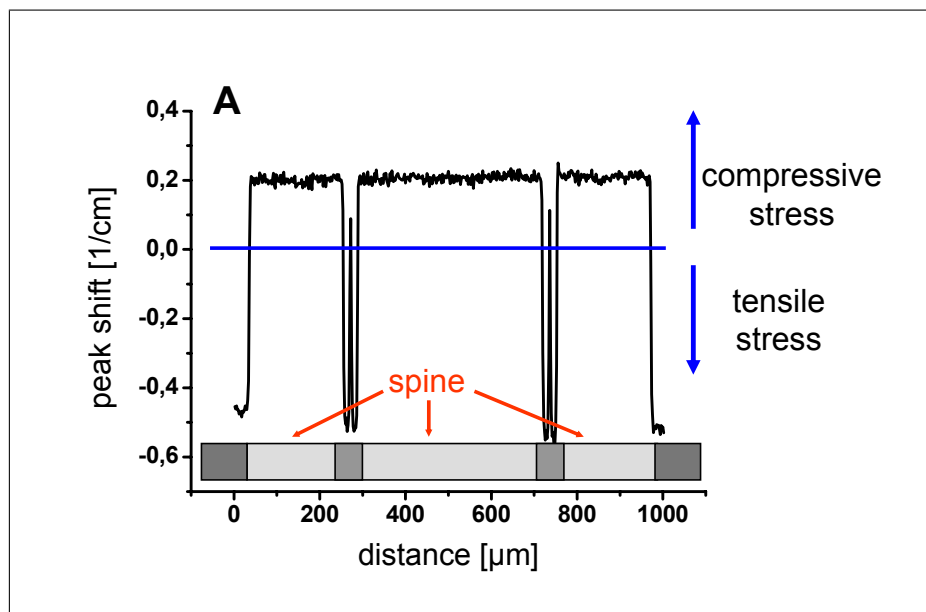
Figure 2.33.: Peak shift of silicon versus scanning position during linescan over spine area.

Measurements (B) and (C) are presented in figure 2.34. For (B) detailed lines-cans over the left (black curve) and the right edge (red curve) of the spine area were made and the silicon peak shift was plotted. The overlay shows that the stress states are the same on both sides, on the spine there is little compressive stress and on the array pad there is tensile stress.

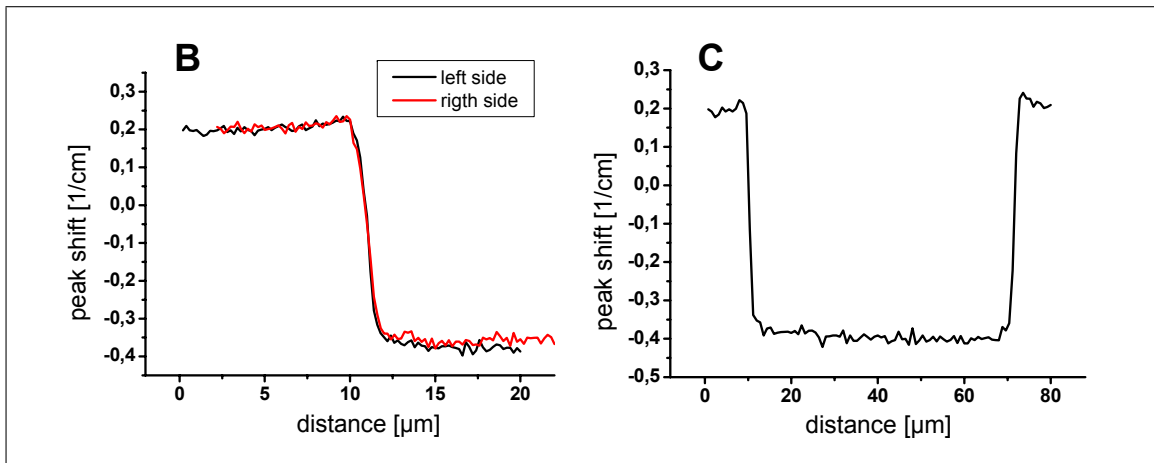Along an array pad finally there is a uniform tensile stress distribution which can be seen in figure 2.34C.

Figure 2.34.: *B:* Linescans over left and right side of the spine edge showing equal stress distribution. *C:* Linescan over an array pad showing uniform tensile stress.

Silicon pads

The next set of measurements was to study the influence of the size of silicon pads on the stress induced by surrounding trench structures. This is important for the chip layout design in stress engineering, i.e. creating stress in structures to alter material properties like the electrical resistance [2]. As a first measurement, horizontal and vertical linescan over a large silicon pad surrounded by trenches filled with silicon oxide, were done. The silicon peak intensity, position and width were analyzed and the results can be seen in figure 2.35.
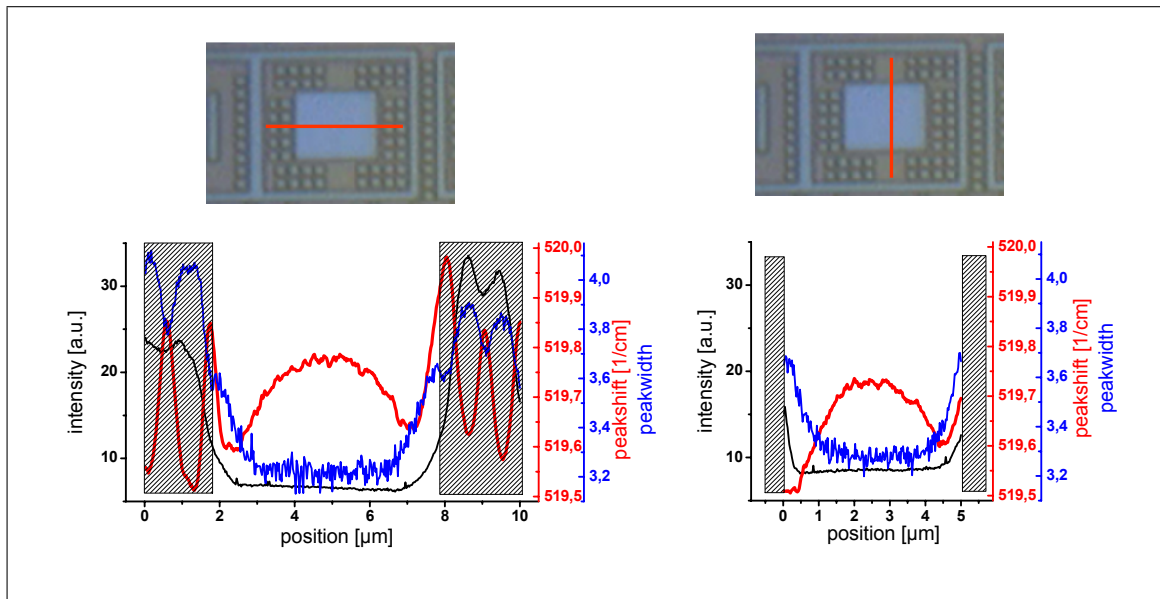
Figure 2.35.: *Left:* Horizontal linescan over silicon pad with peak intensity, position and width plotted versus the scan position. *B:* Vertical linescan over the same pad. A microscope view of the pad used in this measurement is included, with the red line symbolizing the laser position during the scan.

Regarding the left side, strong variations in all three curves are visible in the regions of the small squared silicon spacers next to the pad. Theses regions were marked with dashed boxes and are not looked at further. The interesting part is the area of the silicon pad in the middle. In both scans, horizontal and vertical, the peak position shifts closer to the stress free value at around 520.2 cm^{-1} when reaching the middle of the pad. There, the biggest relaxation from the stress induced by the silicon oxide boundaries occurs.

In a next step linescans were made across a set of silicon pads of different widths. The results are compared in figure 2.36 together with a microscope view of the measured pads. All linescans were made in a vertical direction and show the same behavior of stress relaxation towards the pad center, i.e. shift to wavenumbers closer to the stress free value at around 520.2 cm^{-1}. What is different, is the average pad's stress value in the center. It first increases for smaller pad widths up to pad 4 and then begins to decrease again.
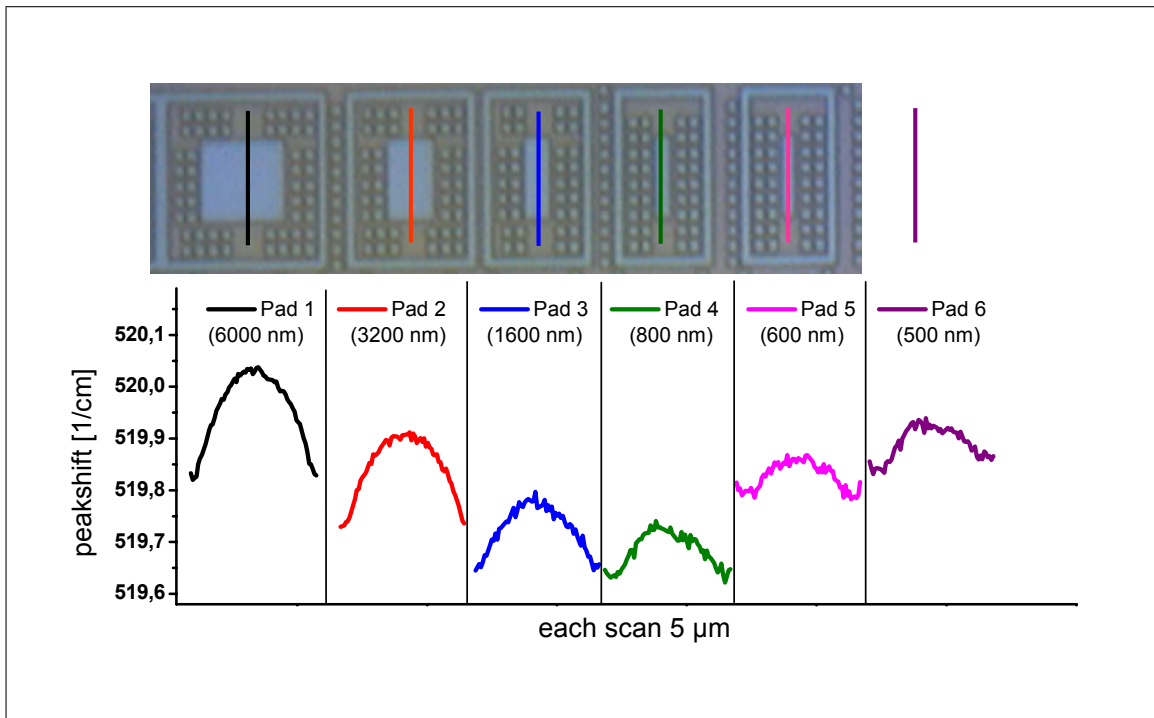
Figure 2.36.: Vertical linescans over silicon pads with different widths. Silicon peak position plotted versus scan position. Microscope view shows the measured pads with the location of the linescans.

A comparison of the average stress value for a specific pad width is given in figure 2.37. The different curves present measurement with all three available laser wavelengths. They were done to study the depth distribution of the stress. A second y-axis was added to the right to give an idea about the absolute stress values related to the peak shifts, but these are just to be seen as rough estimations (see section 2.5). As can be seen from the measurement, the stress seems to be located at the surface as the higher stress values for the blue laser light indicate. For all laser wavelengths the stress first increases with decreasing pad widths and then decreases for the smallest ones. The three measuring points marked as 'STI area' were chosen for comparison on a region far away from the silicon pad, where we have only the areas filled with silicon oxide.

The reason for the observed stress distribution lies in the process of the bilayer oxide fill, where we have a HARP pre-fill in the trench area together with a HDP cap. The tensile nature of the pre-fill creates the stress increase for the pad width up to 300 nm. Then there is a compensation of the compressive HDP cap which dominates for short pad widths [33].
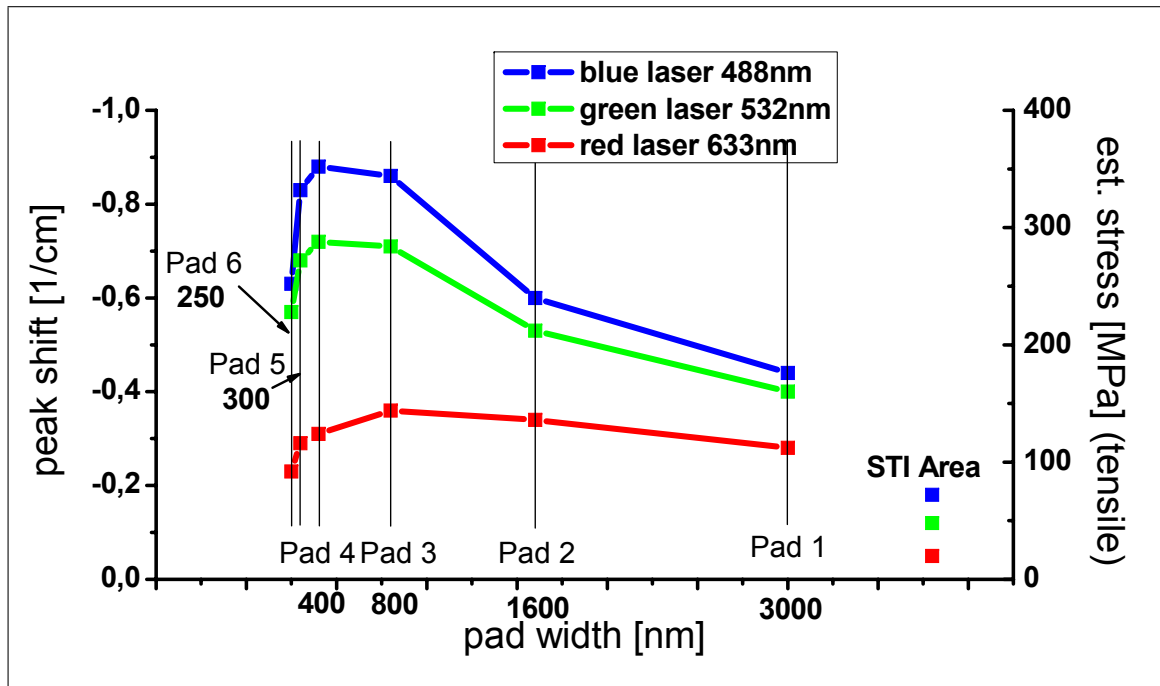
Figure 2.37.: Silicon peak shift versus pad width for three different wavelengths. Points marked as STI area are single measurements far away from the silicon pad. Stress axis added for rough estimation of total (tensile) stress value.

Originally these Raman measurements of the pad width stress dependence were done to verify results from electrical measurements and simulation data performed by Qimonda earlier. The electrical measurements were done with the help of a dummy gate over the pad and by measuring the current change after applying a certain voltage. Simulation data were obtained by complex TCAD simulation and resulted in the dependence of the electric carrier mobility change versus the pad width [33]. Figure 2.38 shows both, the electrical data as the black curve and the simulation results as the red curve. When comparing these with the Raman stress results from figure 2.37 we get the same turning point for a pad width at around 300 nm and thus a good qualitative correlation. With its fast and non-destructive nature, this makes Raman spectroscopy an ideal tool for measuring important material properties in semiconductor chip industry.
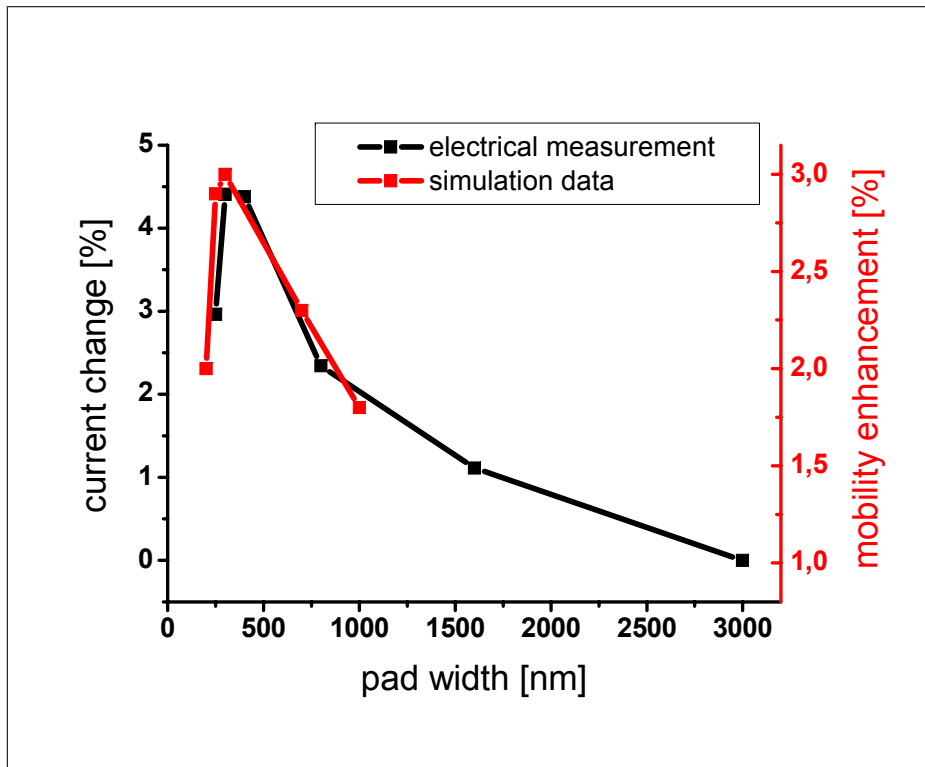
Figure 2.38.: Data from electrical measurements (black curve) for current change and simulation for carrier mobility change (red curve) versus silicon pad width.

Detailed Raman maps

The most descriptive way of presenting stress data obtained by Raman spectroscopy is a two-dimensional mapping. The downside is, the more detailed information one desires and the larger the scanned area is, the more time- and work-consuming the spectra acquisition and data analysis becomes. For a better comprehension of the stress state in the silicon pads used in the last experiments such two-dimensional maps were taken.

Figure 2.39 shows peak shift maps of two different silicon pads where the incoming laser polarization was rotated. Comparing the Raman maps with the microscope views it becomes apparent that STI filled regions (darker ones in the microscope view) lead to compressive stress (positive peak shifts, i.e. red regions in Raman map). On the other hand we get tensile stress (negative peak shifts, i.e. blue regions in Raman map) for the silicon areas. For the larger pad 3, the stress relaxation towards the pad center is also visible. Changing the polarization does not change the stress distribution but only leads to lesser stressed tensile regions.
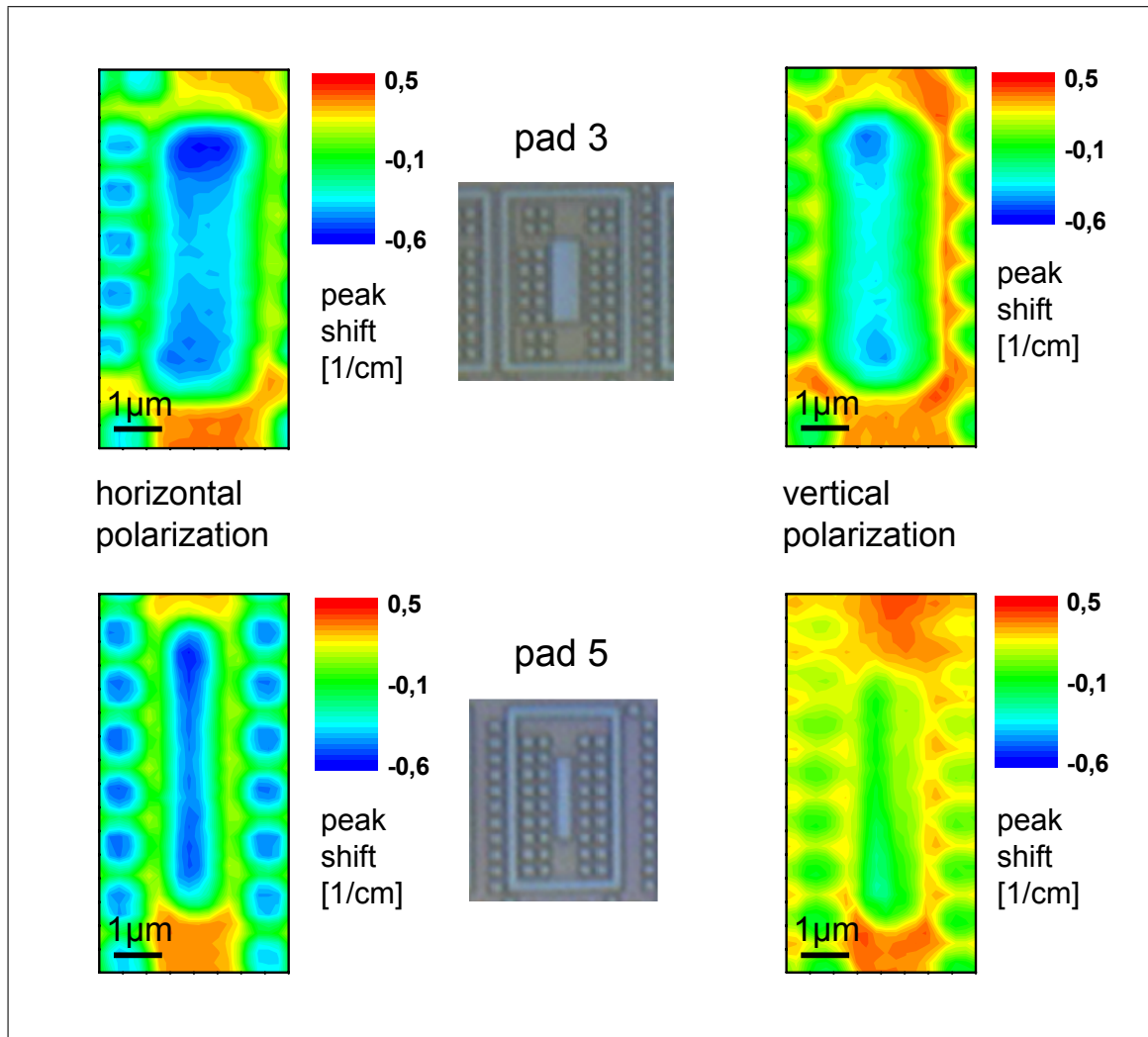
Figure 2.39.: Detailed Raman maps of two different silicon pads showing the silicon peak shift from its stress free position. Incoming blue laser polarization rotated by 90 degrees.

As already mentioned, by using different laser wavelengths the depth stress distribution can at least partly be visualized. Figure 2.40 shows all three relevant peak information, namely the intensity, shift and width in Raman mappings over a thin silicon pad. The results from Raman scans with blue and red laser are compared to each other. The intensity maps are mainly a picture of the samples topography. We get low values for flat regions and high values for structured areas due to increased scattering at edges. In the peak shift maps we again have compressive areas for the STI fills and tensile stressed regions for the silicon structures. By comparing the peak shift maps of the blue side with the red laser side, we see that all tensile stressed regions are next to the surface, and that

the deep penetrating red laser beam only 'sees' compressive stress. Finally the peak width maps show the broadest peaks at structural edges accompanied by certain peak shifts. The red laser peak width map has much narrower peaks, this is again caused by the increased penetration depth. By probing a much larger sample volume, the highly stressed, and thus shifted regions from the surface provide only a small contribution to the whole signal.
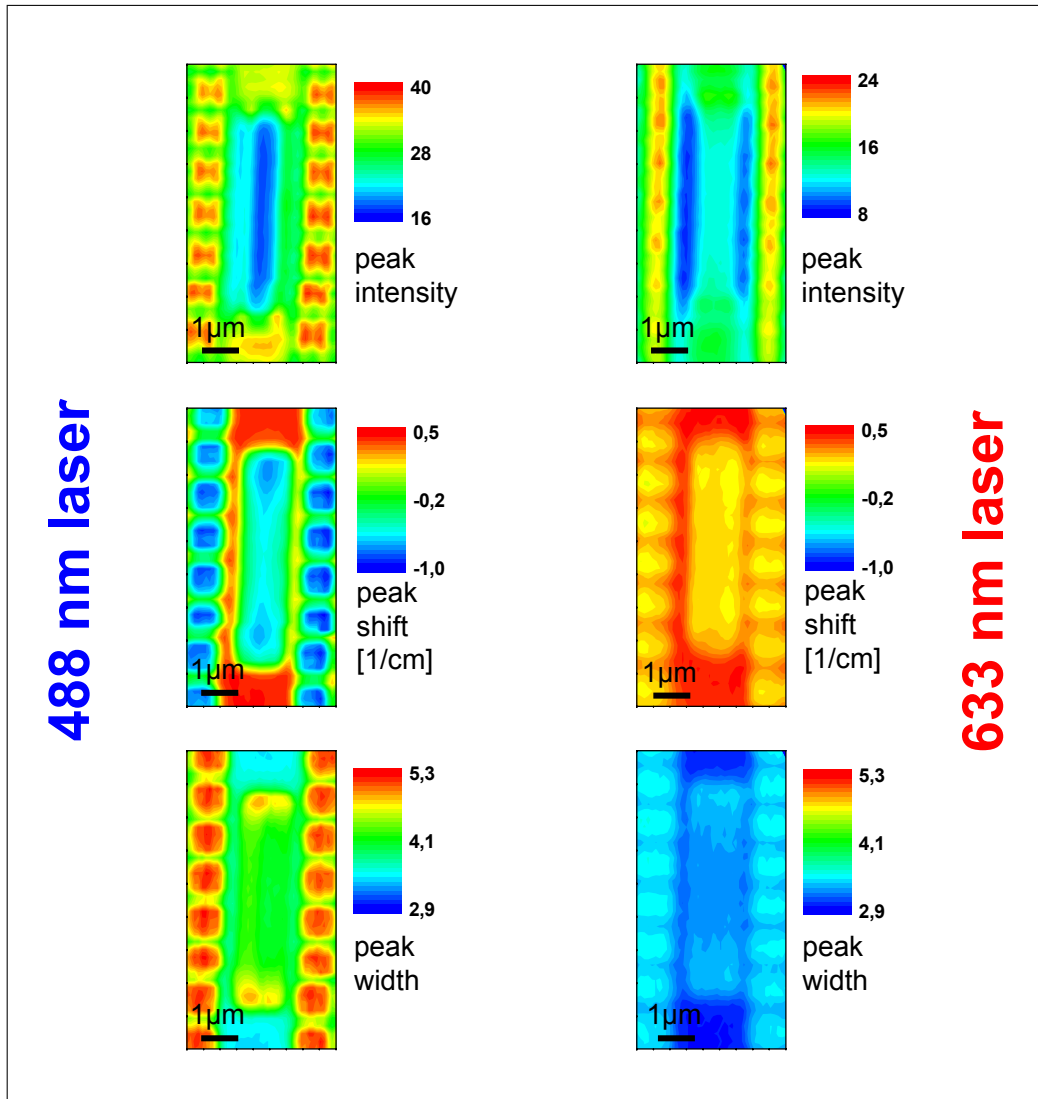

Figure 2.40.: *Top:* Mapping of silicon peak intensity on silicon pad, *Middle:* mapping of silicon peak shift and, *Bottom:* mapping of silicon peak width. Left side taken with blue laser, right side with red laser.

The stress in the support regions between the deep trench arrays is an important information for chip design tasks. Figure 2.41 shows two areas where Raman maps were to be taken, in order to get information about the stress state there.
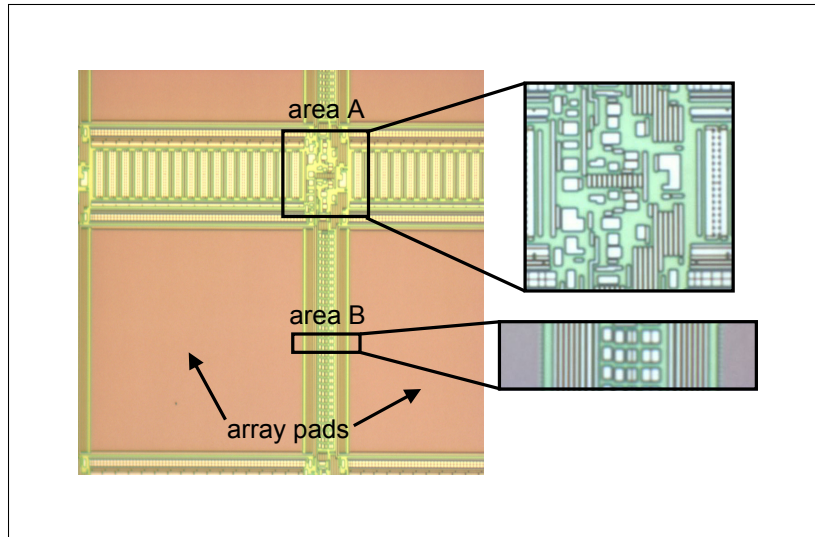

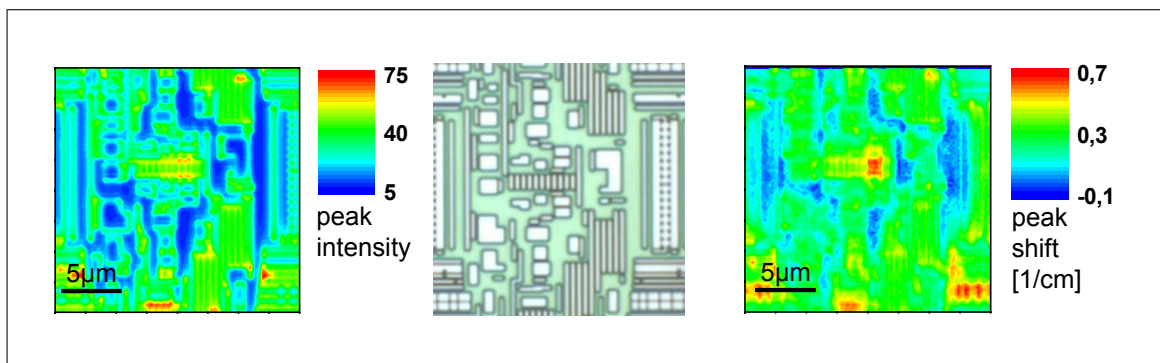**Figure 2.41.:** Overview of support region on chip, areas for Raman mappings shown.

Figure 2.42.: *Left:* Mapping of silicon peak intensity on area A, *Middle:* microscope view of mapped region, *Right:* mapping of silicon peak shift on area A.

The results for 'map A' containing a map of the silicon peak intensity and the silicon peak shift are summarized in figure 2.42. The intensity map on the left of figure 2.42 shows the influence of the topography, flat areas result in small peak heights, while structured regions, for example pads and trenches next to each other, give larger peak intensities. On the right side, the peak shift map

shows the stress state in scanning area A, on specific structures we get rather big compressive stresses, as can be seen by the red regions.

The results of the two-dimensional Raman scan in area B are shown in figure 2.43. Again the intensity map on the top results from the topographic situation on the sample. The peak shift map on the bottom shows little to no stress for the vertical lines and medium compressive stress in the deep trench array to the left and the right. What was surprising for the chip design staff, was the high compressive stress at the border line between array and support structure. Raman spectroscopy again proved to be a valuable tool for getting material information from micro-structured semiconductor samples.
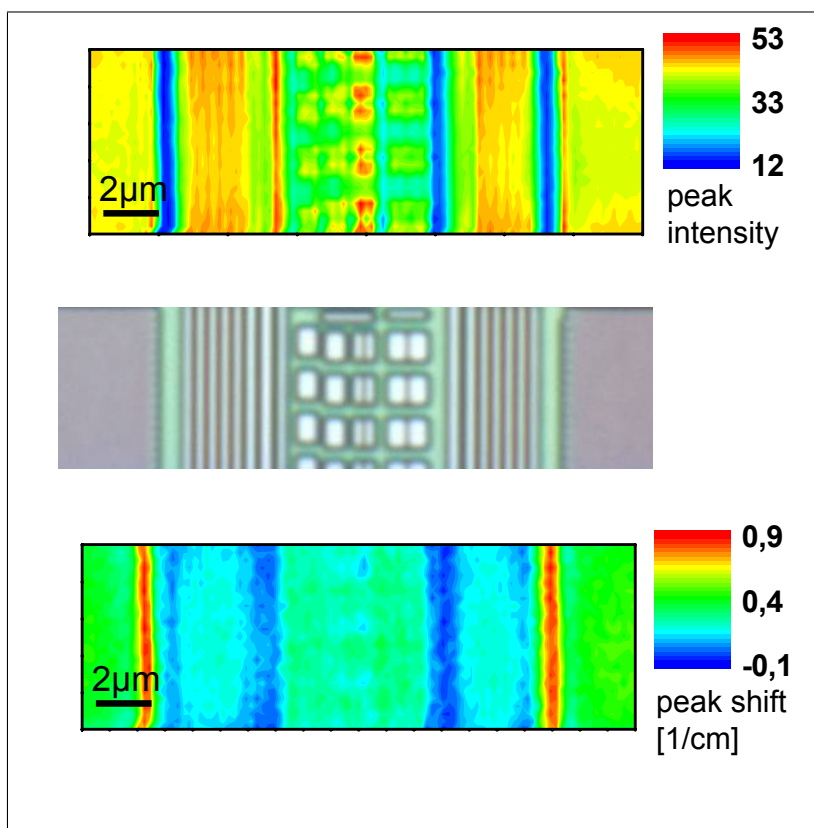

Figure 2.43.: *Top:* Mapping of silicon peak intensity on area B, *Middle:* microscope view of mapped region, *Bottom:* mapping of silicon peak shift on area B.

An excellent way to further increase the informative value of Raman stress maps is the convolution with data from other measurements like SEM or light microscope. By this, it is possible to correlate and pinpoint stress values more precisely to certain micro structures. Figure 2.44 demonstrates this method which is done by matrix multiplication of the peak shift information from a Raman scan and the topographic information from a microscope view.
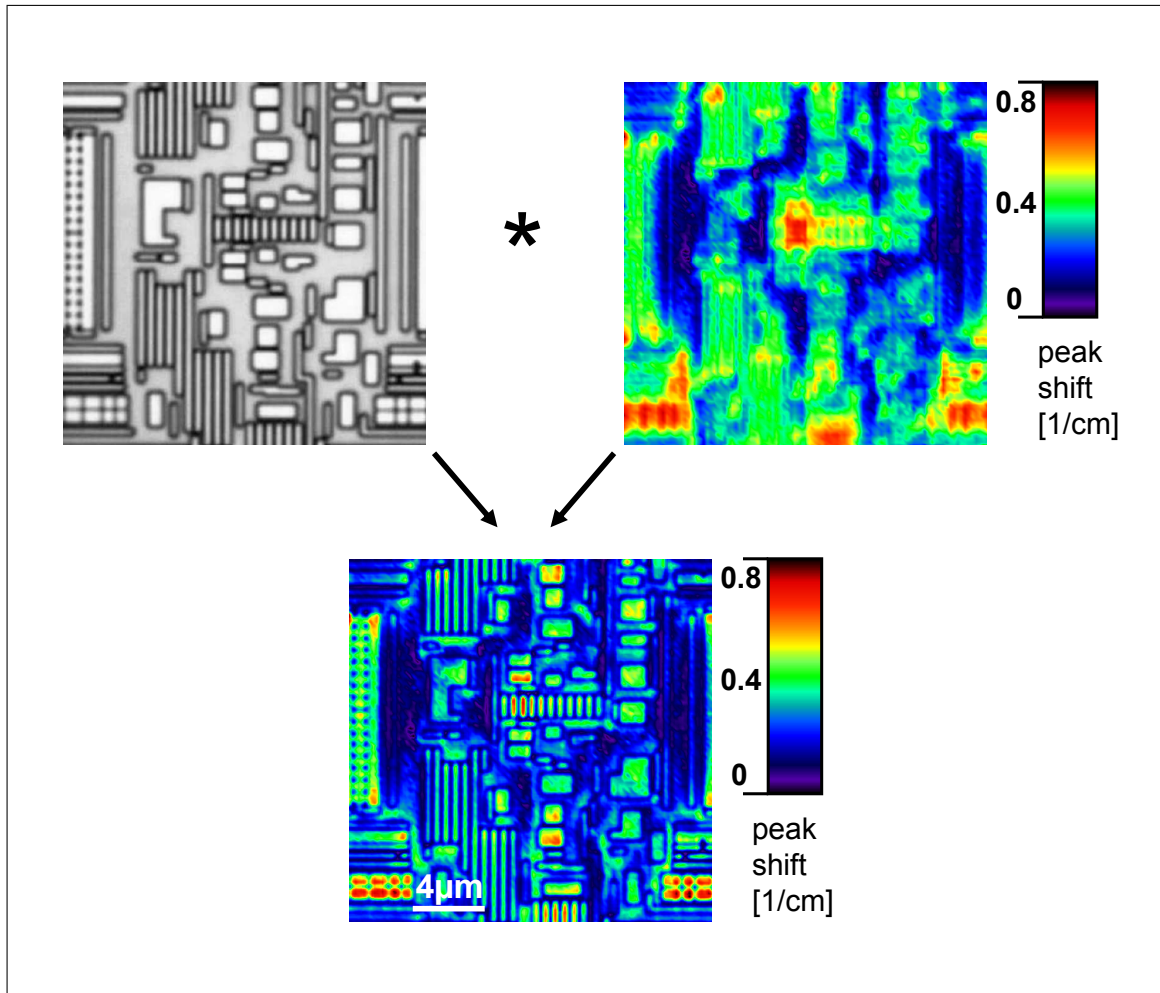

Figure 2.44.: Map overlay process by matrix multiplication of topographic information from light microscope with peak shift information from Raman mapping.
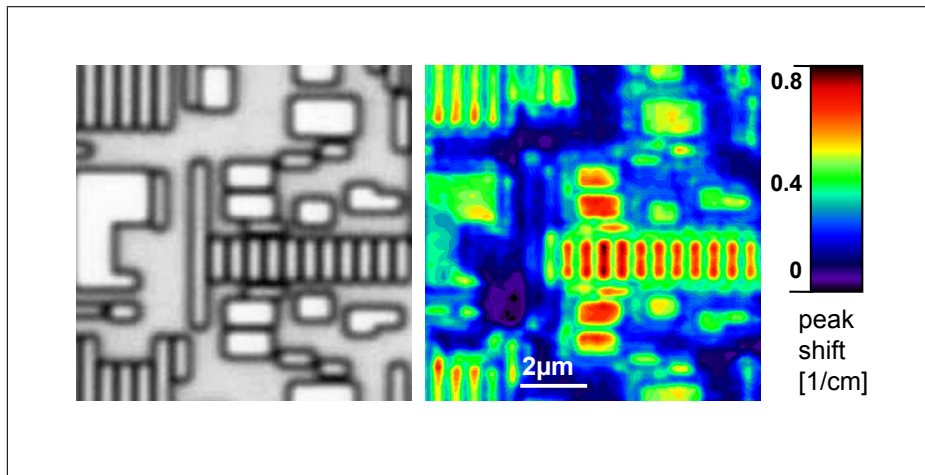
Figure 2.45.: *Left:* Microscope view of zoomed region in area A, *Right:* overlay
with Raman peak shift map for highly detailed view of structure
related stress states.

For an even more precise result, the previous measurement was repeated on
the same region but in a smaller area with a finer step size. Figure 2.45 shows the
measured area in a microscope view and the overlay with the Raman peak shift
map. By this we get detailed information about the stress state in a small area
of micro structured semiconductor devices, which is unmatched by any other
method.

2.4.4. Stokes Anti-Stokes method

Motivation

As the measurements and the data analysis became more and more detailed, an issue occurred when performing Raman linescans. A certain slope or asymmetry was visible for structures which should behave purely symmetric. The interesting fact was, that the intensity plot was perfectly fine, it was the plot of the peak position which caused troubles [34]. To study this unwanted effect several measurements were done and it became clear that this effect depended on the scan direction. Scanning from the bottom to the top was unproblematic but scanning from the left to the right, on the same sample with the exact same scanning and laser properties led to unexpected results. Figure 2.46 shows this effect. A simple linescan was performed over an alternating structure of silicon and silicon oxide filled areas, as the sample sketches illustrate.
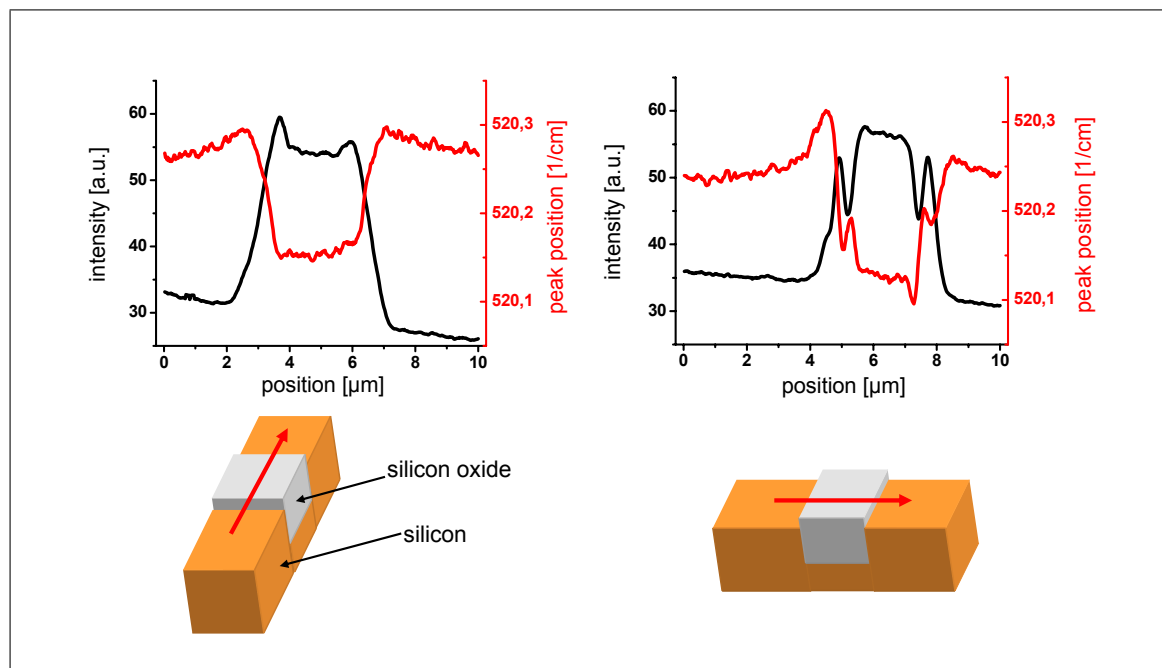

Figure 2.46.: *Left:* Vertical linescan showing intensity and peak position of silicon, *Right:*horizontal linescan with silicon peak intensity and position. Included are sketches of the used sample and the scan direction illustrated by the red arrow.

Apart from a homogeneous slope, presumably caused by a slight defocussing, the intensity curves are symmetric. Changes in the intensity curve shape result from the laser polarization being parallel to the structural edges for the vertical

scan and perpendicular to them in the horizontal scan. However the peak position curve, which should represent the stress state in the material, behaves completely different for the two scan directions. For the vertical linescan it shows the expected symmetric distribution but for the horizontal scan the peak position gives a strange distribution with several local maxima and minima which do not represent the expected stress situation.

It becomes clear that there is another effect causing changes in the peak position which is not stress related. The first assumption, that this asymmetry is caused by a tilted sample could not be verified. Experiments with defined tilted samples show no change in the peak position curve as can be seen in figure 2.47.
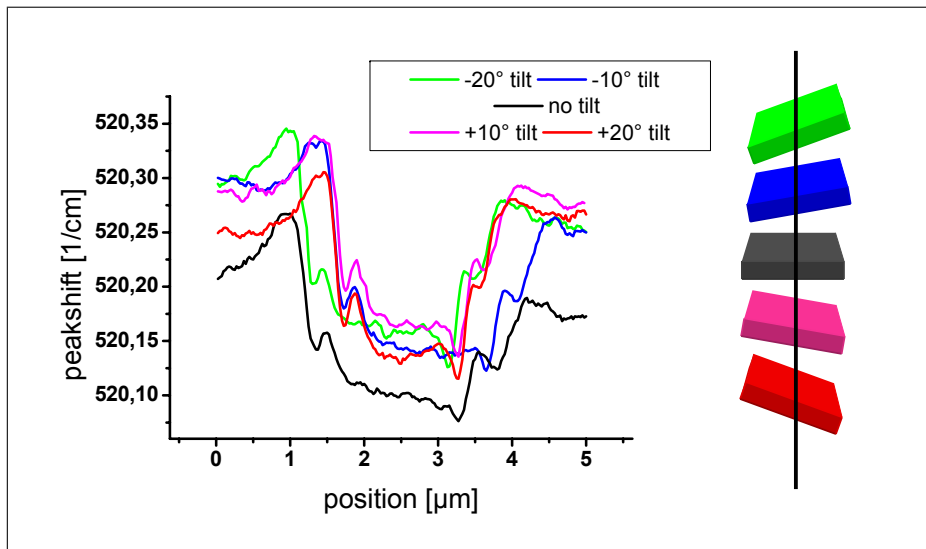

Figure 2.47.: Horizontal linescans over structured sample with different tilt angles. Curves of silicon peak position show no change in asymmetry.

The true reason for the different behaviors in the Raman peak position when changing the scan direction from vertical to horizontal lies in the tool setup. The rectangular slit in the detection path which cuts out parts of the scattered light, as well as the grating with its grooves aligned in a certain direction can lead to deviations of the beam which then reads as spectral changes upon hitting certain CCD pixels.

Many groups using Raman spectroscopy just calibrate their instrument beforehand to standard known emission lines. Then the Stokes peak is recorded and the spectral shift is simply translated into a stress value, regardless of non-stress related effects which might also influence the frequency of the Raman line.

Another common approach is to look at the frequency difference between the Stokes peak and a laser plasma line to compensate for drifting and for calibration issues [25, 35], but because of the plasma line originating from a different sample volume than the Raman line, this can give wrong results when having topographic artifacts (like structural edges which are apparent in almost all samples) or defocusing during the measurement. For high sensitive stress analysis with micro Raman spectroscopy this plasma line calibration is not sufficient and can lead to wrong stress estimations. The experiments with laser plasma lines for peak shift calibration are summarized in figure 2.48.
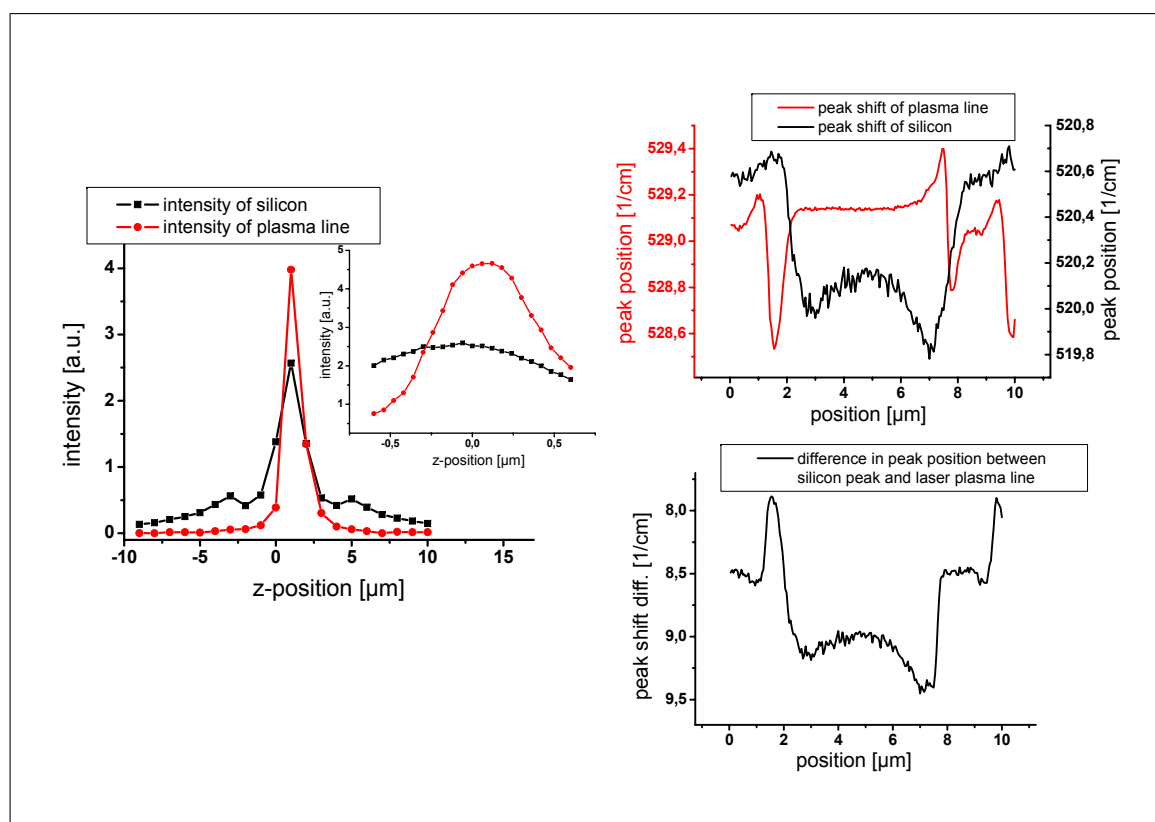

Figure 2.48.: *Left:*Z-scan showing the focus dependence of a Raman peak and a laser plasma line, inset shows a detailed z-scan obtained with the scanner piezos. *Top:* Linescan over silicon pad showing the peak position curves of silicon Raman peak and laser plasma line, *Bottom:* 'calibrated' peak shift by using the difference of the frequency of Raman peak and plasma line.

On the left side of figure 2.48 a z-scan is shown and the intensities of the silicon Raman line and the laser plasma line are plotted. In the inset a detailed z-scan obtained by using the z-piezo of the scanner is added. The curve of the plasma

line is much sharper and reacts more sensitive to changes in the focus position, this shows that both, Raman signal and the directly reflected laser plasma line, originate from different sample regions. In the top right diagram the peak positions from a linescan over a silicon pad are plotted. We see a slight asymmetry for the black curve of the silicon peak but a much stronger one for the asymmetry of the red plasma line curve. Now if we want to use the common method of peak shift calibration by using the frequency difference of the Raman peak and the plasma line, we won't get rid of non-stress related distributions to the peak frequency and still have an asymmetry which might become even worse, as shown in the bottom right diagram.

Solution

The actual method developed and used throughout this work is similar to using a laser plasma line for calibration purposes. The difference is, that together with the normal Raman peak from the Stokes side we also look at the Raman peak from the Anti-Stokes side. For high precision measurements it is necessary to record both peaks from one measuring point at the same time, or at least with a short time delay. By using a diffraction grating with a low number of grooves this can be done in one spectrum, but for stress measurements we need high spectral resolution, thus a grating with many grooves. The procedure now is that after recording the Stokes Raman peak, the grating is rotated by a specific angle, so that afterwards the Anti-Stokes Raman peak can be recorded.

The main idea behind this method is the following. Stress causes the peaks of Stokes and Anti-Stokes excitation to shift symmetrically towards or away from the Rayleigh line by the same value depending on the stress type. In contrast, effects like defocussing, drifting or topography cause both lines to shift either to higher wavenumbers (to the right) or to lower wavenumbers (to the left), i.e. asymmetrically in relation to the Rayleigh line. This is illustrated in figure 2.49.
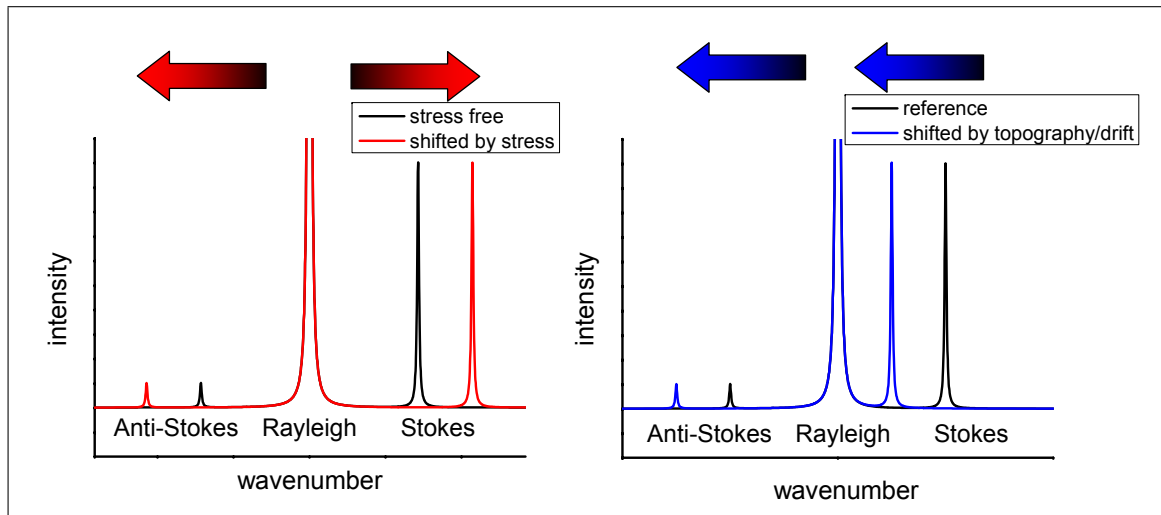
Figure 2.49.: *Left:*Illustration of symmetric stress induced peak shifts, *Right:* illustration of non-stress related asymmetric peak shifts.

The mentioned behavior of stress and non-stress related influences makes clear, that by looking at the sum of Stokes shift S and Anti-Stokes shift A and subtracting the stress-free Stokes shift S_0, one gets exclusively the influence of the stress:

$$\text{stress} = \frac{S + A}{2} - S_0 \tag{2.29}$$

Similarly one can estimate the value of the stress independent influences on the peak shift, here called *artifacts*, by looking at the difference of both peak shifts:

$$\text{artifacts} = S - A \tag{2.30}$$

In the following this method of deconvoluting stress and artifact related peak shift changes is called **SAD** for 'Stokes-Anti-Stokes-Difference'.

Example measurements

Using this method of recording spectra and analyzing the spectral data we gain many advantages:

- non stress related effects can be separated and eliminated

- direct stress information can be extracted out of Raman peak shifts

- restricting conditions like drift due to time consuming measurements can be overcome

- two dimensional scans independent of the scan direction can be made with high precision

In the following, some examples are shown which demonstrate the usefulness and potential of this method.
At first we take the previous example that demonstrated that a calibration with the help of a laser plasma line is not successful. Figure 2.50 shows the results of a horizontal linescan over a silicon pad.
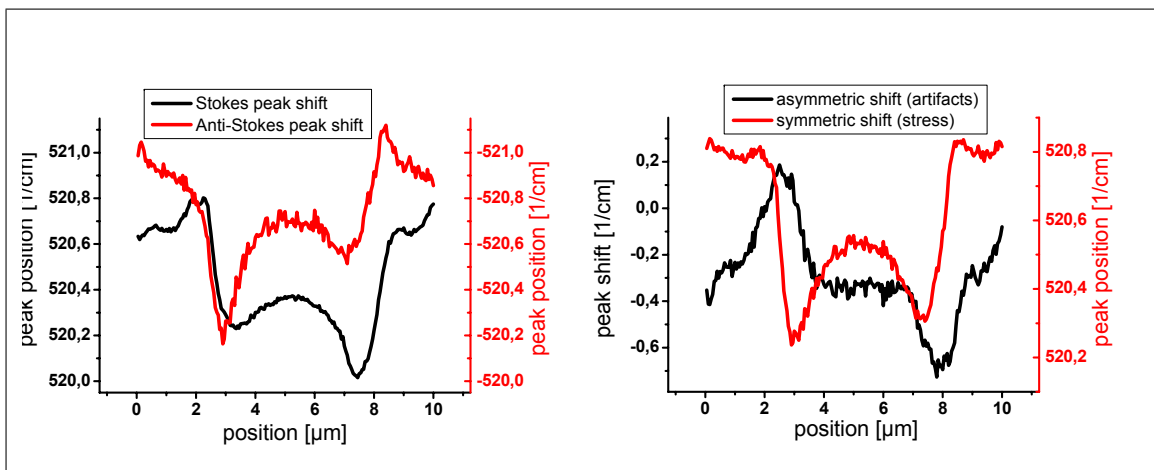

Figure 2.50.: *Left:* Horizontal linescan over a silicon pad with plotted Stokes and Anti-Stokes peak position, *Right:* deconvoluted information of stress (red) and non-stress related effects (black) on the peak position by SAD method.

On the left side the Stokes peak shift, as well as the Anti-Stokes peak shift are plotted in black and red respectively. Both curves show asymmetries in their slope regarding the left and right side of the silicon pad. Note the negative values for the Anti-Stokes peak shift and the higher noise of the Anti-Stokes data resulting from the lower intensity of the Anti-Stokes peak. When the SAD

method is applied we get the right picture of figure 2.50. The deconvoluted symmetric parts give the red curve and show the stress effect on the peak shift, while the asymmetric parts give the black curve and show any other non-stress related effects. For this measurement most of the artifact peak shifts result from the effect of horizontal scanning direction over topographical features like edges. We get an increased peak position on the left side of the pad and a decreasing peak position on the right side.

Comparing the results from a horizontal linescan over a silicon pad, to the results from a vertical linescan, we see that the deconvoluted topographic influence on the peak position is much less, as can be seen in figure 2.51. Here almost the whole influence on the peak position comes in fact from the stress distribution in the sample.
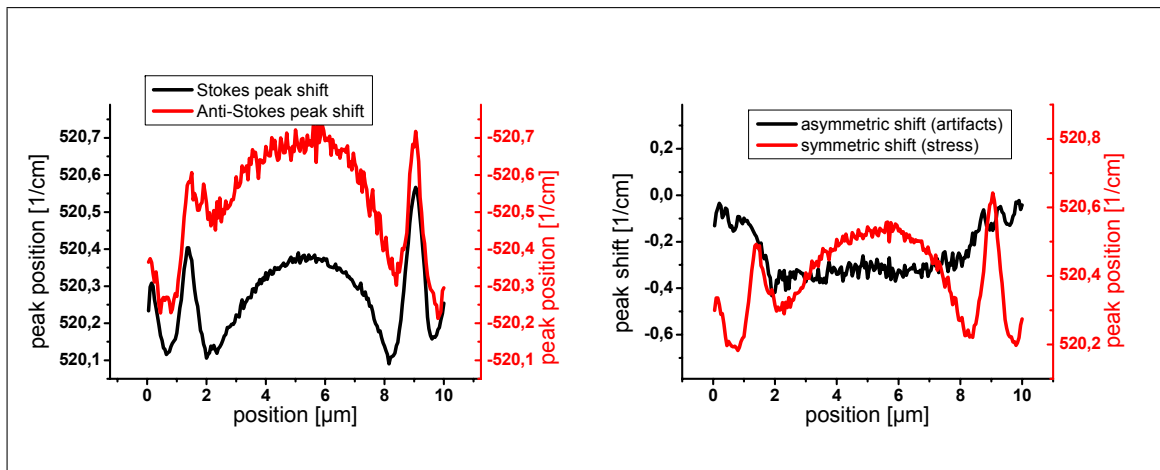

Figure 2.51.: *Left:* Vertical linescan over a silicon pad with plotted Stokes and Anti-Stokes peak position, *Right:* deconvoluted information of stress (red) and non-stress related effects (black) on the peak position obtained by the SAD method.

Another example can be seen in figure 2.52, where a measurement over an array pad in a silicon chip structure is shown. With the simple standard Raman measurement one could expect that the left side and the right side of the array pad have different stress states, which would effect the chip design. However, after applying the SAD method it becomes obvious that again the topography causes the peaks to shift, and that the stress distribution is symmetric.
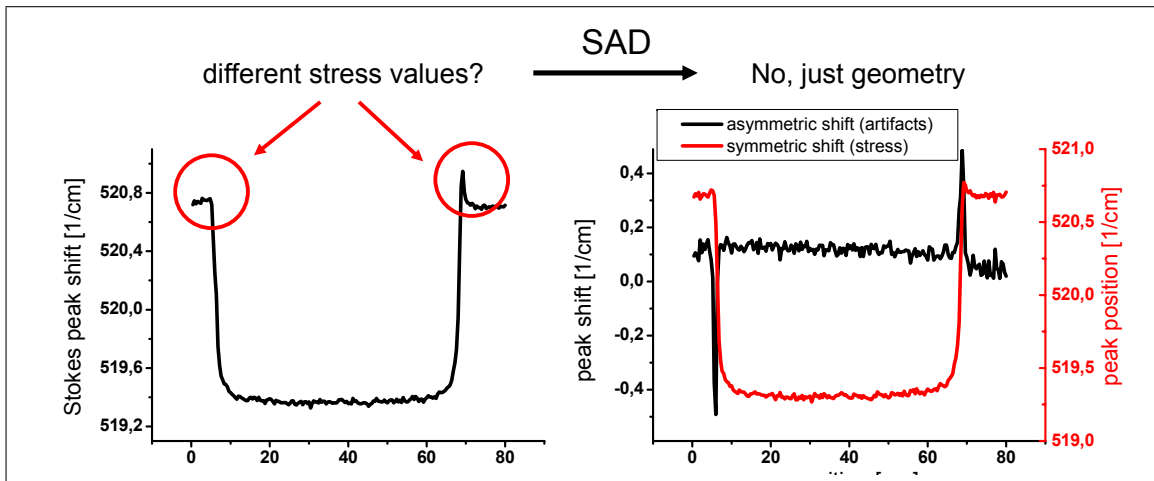
Figure 2.52.: *Left:* Horizontal linescan over an array pad with plotted Stokes peak position indicating different stress states, *Right:* deconvoluted information of stress (red) and non-stress related effects (black) on the peak position by SAD method showing symmetric stress distribution.

In section 2.4.1 some depth scans showing the focus dependency on peak intensity and position were presented. Now a closer look is taken on these results.
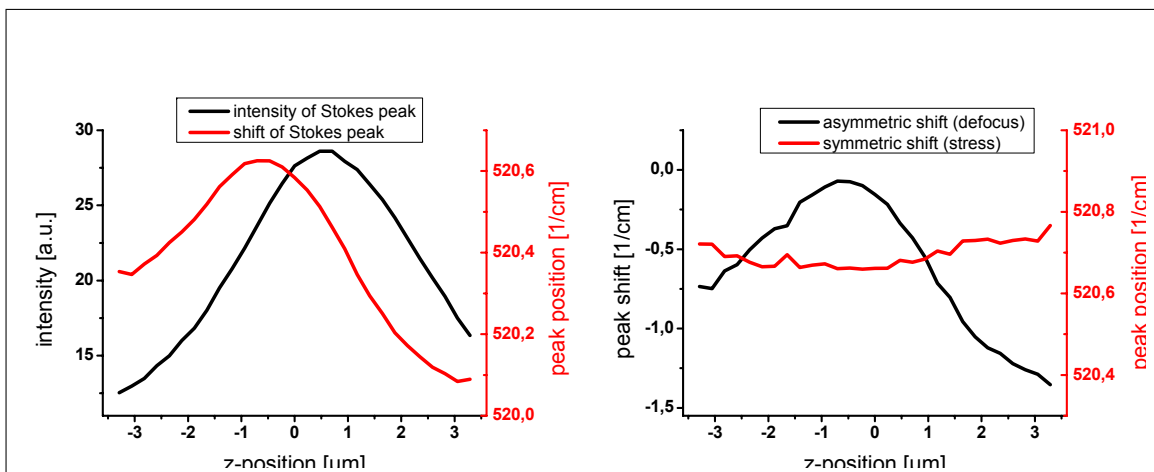

Figure 2.53.: *Left:* Depth scan on a silicon sample with plotted Stokes peak intensity and peak position, *Right:* deconvoluted information of stress (red) and non-stress related effects (black) on the peak position by SAD method, showing focus-related changes in peak position and little stress change.

The left side of figure 2.53 shows the plotted silicon peak intensity and peak position as a function of the focus position on the z-axis. A rather strong influence of the focus on the peak position is visible, which one would interpret as stress changes. With the SAD method the right side of the figure clearly shows that the stress changes are very small and that the majority of the changes in peak position in fact result from the change of the laser focus. This statement is rather important because focus changes can happen in every measurement, be it single acquisitions, linescans or two-dimensional maps.

One of the most important aspects of being possible to separate stress and topography effects on the peak shift in Raman spectroscopy is, that two-dimensional Raman maps with high precision can be generated. This is demonstrated in figure 2.54, where a Raman map was taken over one of the by now well known silicon pads. On the left side we have the maps from the Stokes and Anti-Stokes peak position, which both show an asymmetric behavior. With the help of the SAD method the source of this asymmetry can be clearly identified as a topographic effect resulting from the left and right edges of the pad. The extracted symmetric peak shift information in the top right map can now be used to make statements about the true stress state in the material.
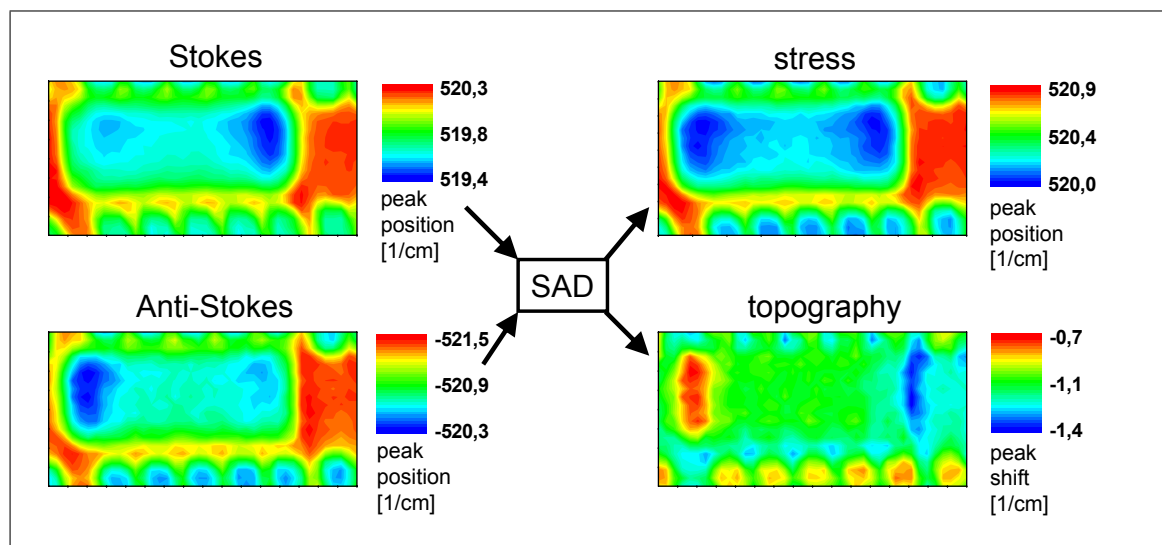

Figure 2.54.: *Left:* Stokes and Anti-Stokes peak position from a Raman mapping over a silicon pad, *Top right:* deconvoluted information of stress dependent effects on the peak position, *Bottom right:* topography related artifacts.

Another two-dimensional Raman mapping where the SAD method was applied can be seen in figure 2.55. In the top left a microscope view of the scanned region is shown, and in the top right the normal Stokes peak position is plotted. After deconvolution we get the pure stress-dependent information in the bottom left part of the figure. The non-stress related effects for the Raman peak shifts are then given in the bottom right part. Here two different sources can be distinguished. One is the change on structural edges which can be seen in the region marked with the red ellipse and the other are focus dependent changes, marked with a blue circle.
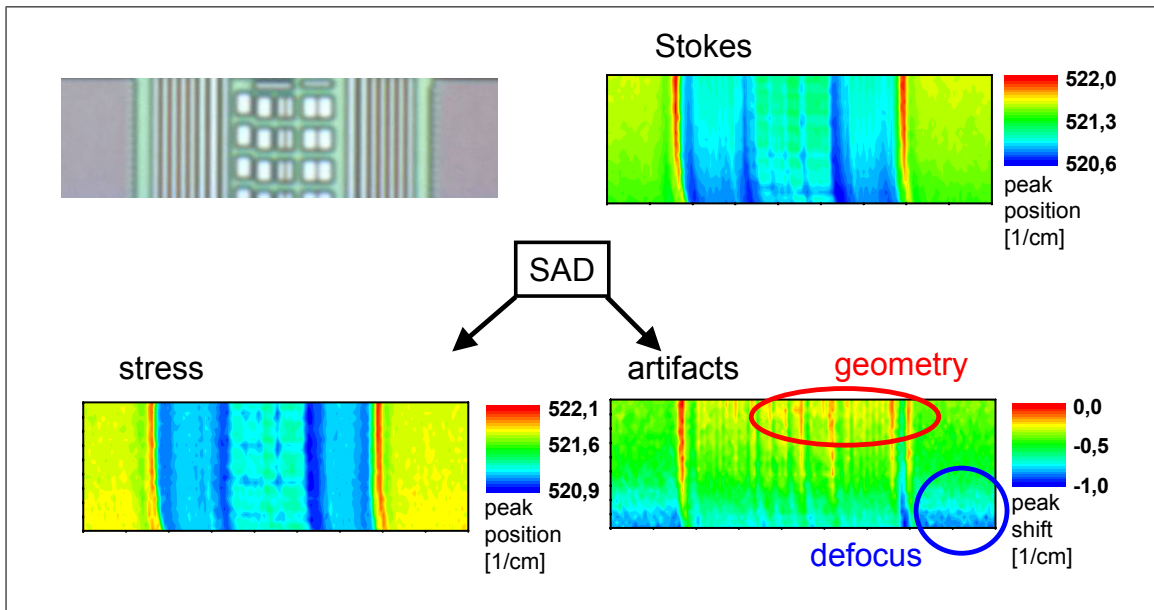

Figure 2.55.: *Top left:* Microscope view of the mapped sample structure, *Top right:* Stokes peak position from the Raman mapping, *Bottom left:* deconvoluted information of stress dependent effects on the peak position, *Bottom right:* non-stress related sources of Raman peak shifts, for example structural edges (red ellipse) or defocussing (blue circle).

2.5. Modeling

Generally it was avoided to give absolute values for the stress in the sample. Apart from the statement that tensile stress results in lower wavenumber and compressive stress results in higher wavenumbers of the silicon peak, it is rather complicated to extract the exact amount of stress, let alone all of the stress tensor's components. For unstructured samples with a distinct, previously known simple stress distribution, e.g. uniaxial stress, it is possible to correlate the Raman peak shift directly to the amount of stress (see section 2.2.3). But as soon as structural edges or more complicated, unknown stress states are involved, the whole system becomes way more complex.

If one wants to simulate Raman linescans for comparison with experimental data, several subproblems have to be solved:

1. penetration of the laser beam into the sample, for the amount of intensity at every volume element

2. stress state at this volume element

3. computation of the measured peak shift resulting from this stress state

4. calculation of the Raman scattered intensity which can reach the detector

5. integration of all single contributions to form the total signal at every scanning point

Each subproblem comes with certain assumptions and simplifications given by the actual complexity. In the following, a closer look is taken on these subjects and some general statements are derived from them.

2.5.1. Defocussing

At first it is important how the incident laser beam behaves when being focused onto a flat silicon sample. To model this a simple MathCAD calculation was done involving the ABCD-matrix theory for Gaussian beams. The principle is, that the Gaussian beam is defined by a complex parameter q, which changes when passing certain optical elements. Every element, e.g. travel distance in free space, a focusing lens, or passing of a different material, is characterized by a certain matrix. The final q parameter is then derived by multiplication of all matrices to the incident Gauss beam. By this we get a pattern of the electric field distribution inside the sample.

Figure 2.56 shows the calculated intensity values of a Gaussian beam which is

focused above, directly at, and below a silicon surface respectively. If we take a closer look at the cases of focusing above and inside the sample, we see that although the distributions look quite different, the main signal always comes from the sample's surface. This is because absorption and reabsorption have a much stronger effect than the distribution of the beam. So the approach to perform depth profiling in silicon by changing the z-focus position [36] doesn't seem to be practical. The whole simulation, where the effects of the sample's refractive index and the absorption can be studied, is shown in the appendix A.2.
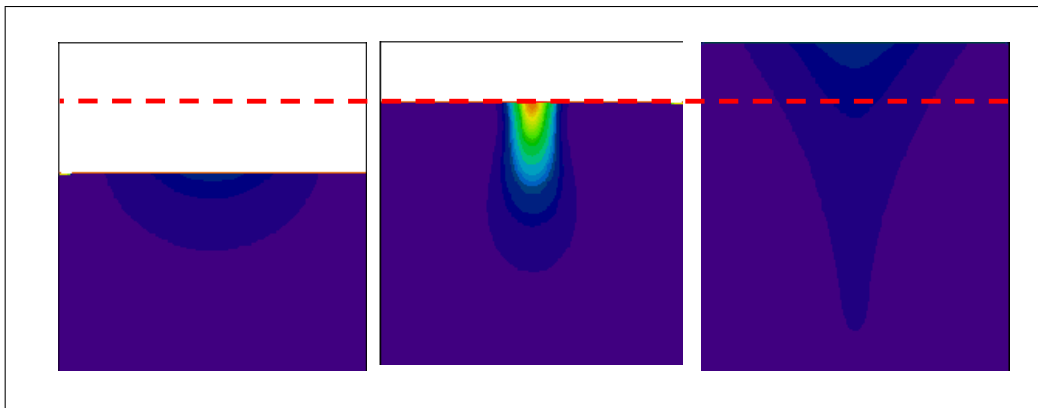

Figure 2.56.: Intensity distribution of a Gaussian laser beam (633 nm) in a silicon sample (objective's NA was 0.8), *Left:* focused two microns above the sample, *Middle:* directly on the sample's surface, and *Bottom:* two microns inside the sample. The dashed line illustrates the position of the focus.

2.5.2. Linescan

In the last section many experiments showed an increase in Raman peak intensity when scanning over a topographic edge. In order to understand the influence of topography and material on the Raman signal, another calculation was done, again with MathCAD. These calculation are based on an analytical model developed within this thesis. A Gaussian laser beam is scanned over a topographic step of a high refractive index material. Effects like absorption, refraction, structural shadowing, reabsorption and signal integration were included in the two-dimensional calculation.

The results in figure 2.57 showed, that on convex corners we get an increased signal and on concave a decreased signal. The reason for this is the following: the Raman light generated at each point in the sample is scattered uniformly in all directions, but because of the high refractive index of the material only a small portion of this angle distribution can reach the objective and can thus contribute to the signal. Most parts can't leave the sample because of total reflection. On convex corners a larger part of the whole angular spectrum can leave the material. With this simple model the edge-effect of increased Raman intensity at structural edges can be understood. Figure 2.57 shows such a topographical step. The color coding means how much intensity reaches the objective, if the Raman signal was generated at this point.
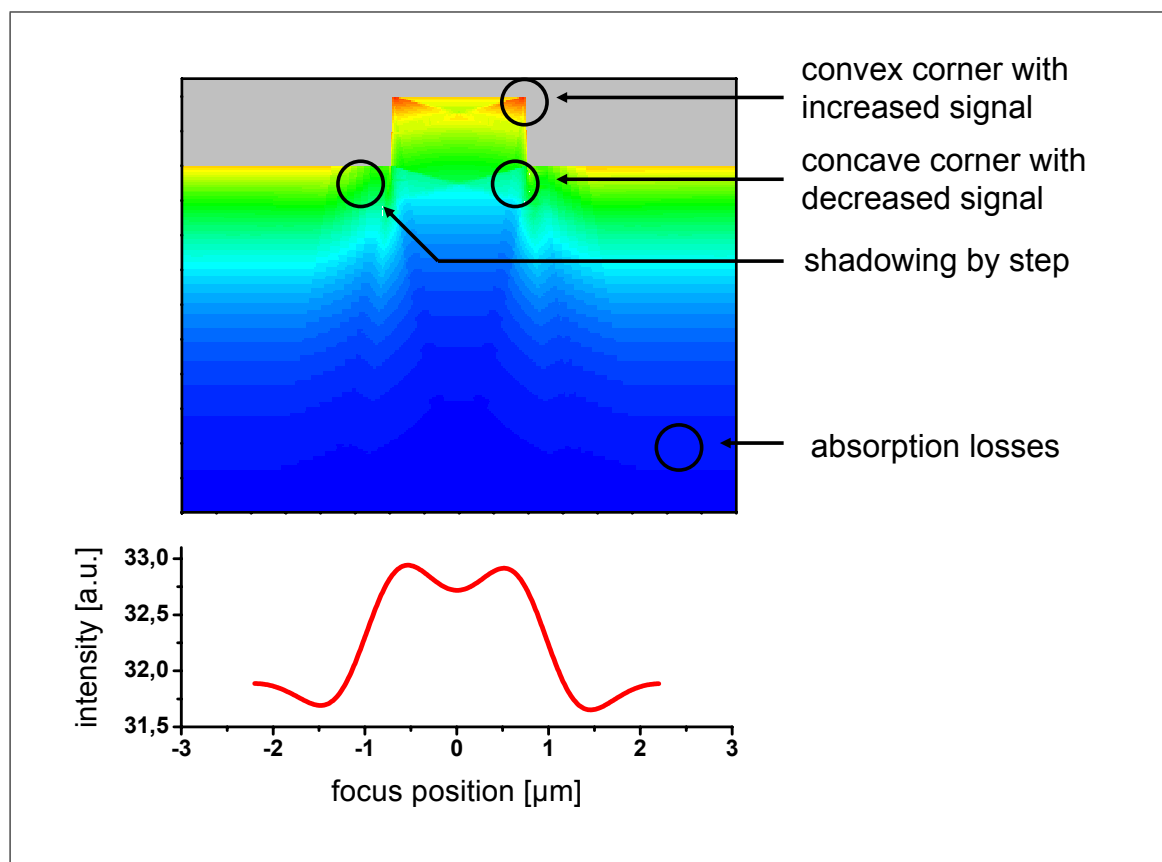

Figure 2.57.: *Top:* Calculated values showing how much Raman signal generated at a certain point reaches the objective, *Bottom:* integrated signal of the individual point's contribution when scanning the laser from left to right.

Besides the increasing and decreasing effects at the structure's corners, we clearly see the quick decrease into the depth caused by the absorption of the material. To the right and the left of the step there is also a small signal decrease because some parts of the angular distribution can't reach the objective due to shadowing of the step itself.

Below the figure is a plot of the integrated intensity over the whole volume with its respective weighted signal portions versus the position of the laser focus. In the weighting, parameters like the beam width and the penetration depth [37] are taken into account. The edge effect can clearly be reproduced. This simple model is by far not exact, effects of beam focusing, diffraction, polarization or the impact of a three-dimensional calculation were not considered. Details and parameters of the simulation can be found in the appendix A.2.

2.5.3. Finite element stress simulation

Finite element calculations were done with ANSYS[3]. Silicon pads surrounded by trenches filled with silicon oxide were simulated under different process conditions. As a result the distribution of stress and strain in different directions were calculated.

Figure A.2 shows such a simulation compared to a Raman mapping over a similar structure. The microscope view on the right shows the silicon pad surrounded by a trench structure which is filled by silicon oxide. To the right and the left of the silicon pad there are squared silicon spacer structures. The simulation in the middle only shows a quarter of the whole structure to save computation time, but this should be sufficient because of the structure's symmetry. The simulation gives calculated values of the x-component of the stress tensor, both in the silicon oxide and in the silicon. Negative values correspond to compressive stress while positive values correspond to tensile stress. Keep in mind that for the Raman shift we already stated that negative peak shifts mean tensile stress and positive peak shifts mean compressive stress.

---

[3]ANSYS inc, United States, http://www.ansys.com

Comparing the Raman stress map and the simulation, we see that next to the silicon pad, marked by black circles, we have compressive stress, seen by the red areas in the Raman map and the lime colored areas in the simulation. On the other hand directly on the pad and on the silicon squares, marked by white circles, there is tensile stress. These are the blue areas in the Raman map and the orange colored areas in the simulation. The highly tensile and compressive stressed red and blue regions in the simulation all correspond to the stress state in the silicon oxide, which cannot be observed with the Raman measurements.

When we apply the uniaxial stress model calculated earlier we get absolute stress values which are much higher than the ones seen in the finite element simulation. Presumably the difference comes from other stress components or different assumptions made for the stress simulation. For example if one takes slightly different process parameters, the resulting stress distribution changes completely, see for example appendix A.3.
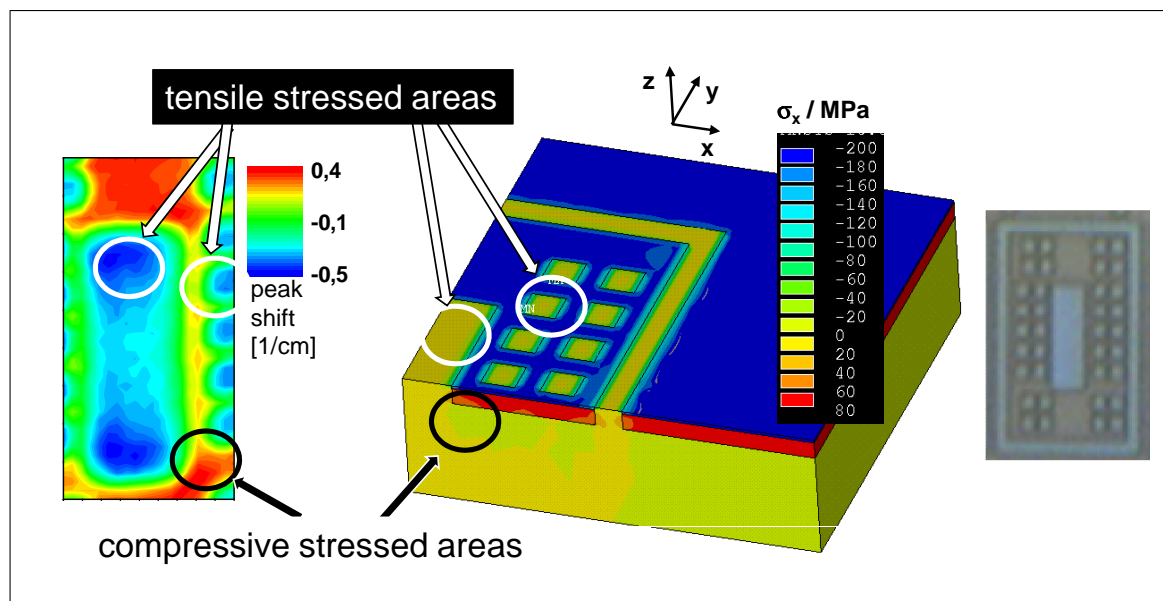

Figure 2.58.: Comparison of a Raman peak shift map over a silicon pad surrounded by trenches filled with silicon oxide with a finite element simulation. *Left:* Raman shift of the silicon peak, *Middle:* ANSYS simulation of the stress component in x-direction in silicon and silicon oxide, *Right:* microscope view of the measured structure.

2.6. Summary

Raman microscopy was used to measure the stress induced changes in the material properties of semiconductor structures. From single spectra, over linescans up to two-dimensional Raman mappings were performed on a variety of structures, like standard silicon samples, PZT specimen, nanowires or structured and multi-layered industrial chip samples. Comparison of different STI fill processes, different process parameters or the influence of topographic features have been discussed. Detailed two-dimensional Raman maps gave a comprehensive overview over the stress state in micro-structured chip samples. In addition a novel method, called 'Stokes-Anti-Stokes-Difference' was proposed, which enables us to separate the effects which cause the Raman peak to shift depending on their origin. By this we can distinguish between stress related effects and non-stress related effects, like defocussing, topographical edges or instrumental artifacts. It was clearly shown that the non-stress related peak shift effects play an important role if one conducts micro Raman measurement with high spectral resolution, and that the deconvolution via the SAD-method is crucial for the exact interpretation of the measured data.

The modeling of Raman linescans was discussed and it showed that several subproblems have to be solved. In general it is not possible to gain access to the complete stress tensor just by a single Raman measurement. Prior knowledge of the principle stress state, e.g. uniaxial or biaxial stress, is needed in order to connect Raman peak shift and absolute stress value. When dealing with different materials or topographic features, a model which also includes the laser beam parameters, has to be developed. The principle way to do this was touched on and some simple simulation examples were shown. Furthermore, a rough comparison between the stress data extracted from Raman measurements and a finite element simulation of a semiconductor structure could verify the measurements. Although care should be taken when assigning absolute stress values to Raman peak shifts, Raman microscopy proved to be a powerful tool to compare relative stress values.

3. Enhancing the Raman Signal

3.1. Introduction

As we have seen in the last chapter, Raman spectroscopy proved to be a powerful tool for measuring the stress state in a semiconductor sample. However, two important issues are to be faced. Namely the **spatial resolution**, i.e. the size of the area our Raman signal comes from, and the **signal strength**, which determines the possibility to resolve and fit individual Raman peaks. This chapter is about enhancing and confining the Raman signal by introducing metalized tips or metal nanoparticles inside the laser beam in the vicinity of the surface.

Overcoming the diffraction limit

In conventional microscopy there is always a limit in the spatial resolution. This limit originates from the minimum diameter a light beam can be focused on the sample. This spot size is limited by diffraction and depends mainly on the used wavelength, the focusing angle of the objective and the refractive index of the ambient medium. For high numerical aperture objectives and with use of immersion oil the optical resolution can be brought down to about half the used wavelength.

Overcoming these limitations has been the subject of many researchers for a long time. It was Synge who first dealt with this problem in detail in the early 20th century [38]. His ideas later formed the basis of todays *Scanning Near-field Optical Microscopy (SNOM)*. He proposed to limit the spatial dimension of the light beam by bringing an aperture smaller than the light's wavelength close to the sample which would confine the beam spot to the aperture size. The aperture or the sample is then scanned to acquire an image with high spatial resolution. However the technical hurdles for this approach, like the formation of a small aperture, keeping a small distance to the sample, and the scanning itself were big challenges at this time. It was not until 1972 as Ash and Nicholls gave the first experimental proof for Synge's ideas by confirming a spatial resolution of

$\lambda/60$ with microwaves [39]. Sub diffraction-limited resolution in the visible light regime was first shown in 1984 by Pohl et al. with a resolution of approximately $\lambda/20$ [40]. Today SNOM is widely used in a variety of applications [41–45].

Setups with apertures consist usually of a tapered fiber tip with a metal coating, which has a small opening at the apex. It can be used in illumination mode where the incident light beam comes through the fiber onto the sample and the signal is detected in the far-field. Alternatively, in detection mode, the sample is directly illuminated and the fiber tip is used to collect the near-field signal to the detector.

The original idea of using an aperture to create or collect evanescent waves at the sample surface can be inverted by using a small object with the dimension of the aperture instead, this is known as Babinet's principle. It leads to a second kind of setup, named apertureless scanning near-field microscopy or *Scattering Scanning Near-field Optical Microscopy (S-SNOM)* [46, 47]. Here an object, for example a tip, is used to create evanescent waves near the surface, or to collect near-field information from the surface by picking them up and converting them into the far-field for detection. Detailed information about the near-field character and evanescent waves can be found in the literature [48]. For the apertureless case there exist different modes of operation concerning the direction of incident and scattered light. The different modes are depicted in figure 3.1. Because solid silicon samples are non-transparent for visible light only the reflection setup, the right most one in figure 3.1 is usable for opaque samples. Here the incident light is focused onto the sample by an objective and collected either through the same or a second one above the sample.
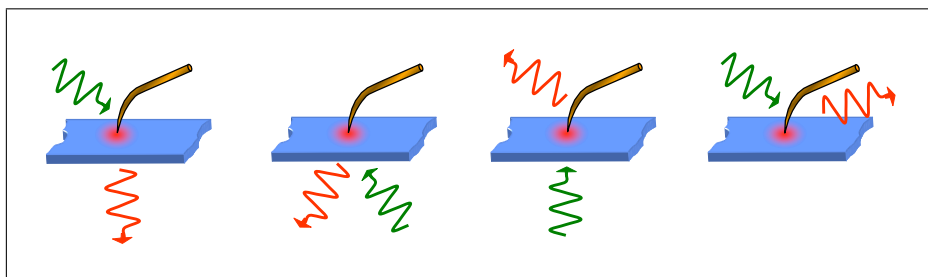

Figure 3.1.: Different modes of illumination (green) and collection (red) in apertureless microscopy setup.

In principle we could use simple glass tips to pick up evanescent information from the sample, but if we use metalized probes, there are additional favorable

effects that can be exploited. One of them, the excitation of collective electron oscillations in a metal by light called *plasmons*, can lead to a huge increase in the strength of the electric field in the vicinity of the metalized object [49]. If the resonance conditions are met we thus have some kind of localized light source whose size is no longer determined by the wavelength, but by the dimension of the tip. So if we bring down a metalized tip in proximity to the surface and illuminate it with light under the right conditions we get mainly three important effects:

- local increase of the electric field of the incoming light

- pick up of near-field information from the surface

- increase of the scattered signal intensity from the surface

So this suggests a method to deal with the two major problems in semiconductor stress measurement by Raman microscopy: we increase the signal intensity and confine the region of information, improving our lateral resolution.

Enhanced Raman microscopy

The concept of using metalized probes in Raman microscopy is known under the name of *Tip-Enhanced Raman Microscopy (TERS)*. Today TERS is used by many groups for many different applications in a variety of setups. Most of them deal with the measurement of organic samples [50, 51], biological samples [52, 53], fullerenes [54], carbon nanotubes [55, 56] to just name some of them. Using TERS to improve stress measurements in semiconductors [57–59] is quite rare because there are inherent difficulties and limitations for the interpretation of data and the experimental setup. First of all, semiconductors are poor Raman scatterers compared e.g. to organic dies, and the high refractive index means big reflection losses at the surface for both incident and scattered light. As already mentioned, we have to use a reflection mode setup which limits us further. Unlike for small, single objects of interest, for example carbon nanotubes, we have to deal with a huge far-field background from the laser spot, making it difficult to analyze the near-field signal. Finally, the demands on the spectrometer are much higher because we don't have to measure simple intensities, but frequency changes of tenths of relative wavenumbers which requires peak fitting and thus sufficient signal strength.

Due to the rather complicated case of having an (at least at nanometric dimensions) arbitrary formed tip oscillating over a surface, a preliminary experiment was chosen to study the parameters used in later TERS measurements. By using

metal nanoparticles directly deposited onto the sample we get rid of the distance dependence between probe and sample and we gain much better reproducibility by having uniformly sized particles. Throughout this chapter these measurements are called *Surface Enhanced Raman Scattering (SERS)* experiments, although the original SERS-effect [60, 61] is obtained when using roughened metal surfaces and coatings rather than single nanoparticles and can involve an additional chemical enhancement [62].

The dependence of particle properties such as size or material and the irradiance properties, i.e. laser wavelength or polarization, are examined regarding their effect on the Raman signal enhancement. The localization of this enhancement is studied by using stacked samples. A possibility to go from immobile metal nanoparticles to scannable nanoparticle probes is demonstrated by the concept of tip-picking. In addition, TERS linescans with metal coated glass tips are shown and their influence on improving signal contrast and resolution is discussed. For the TERS measurements the Raman spectrum with tip and without tip inside the laser focus is called near-field and far-field contribution in this work. It should be noted that for the tip-in-contact-case there is always the sum of different effects, namely far-field signal from the laser spot, near-field signal and shadowing from the tip, it is just called near-field here for the sake of simplicity.

3.2. Theoretical basis

3.2.1. The diffraction limit

When speaking about optical resolution in spectroscopic techniques, there is always a so-called diffraction limit, which prevents us of getting information from regions smaller than a distinct, wavelength dependent area [63, 64]. To calculate this limit, we start with a circular aperture irradiated by light. Under the conditions of incoming coherent light, planar wave fronts and the image plane situated in infinity we get for the irradiance I [48]:

$$I = I_0 \left| \frac{2J_1(\rho)}{\rho} \right|^2 \tag{3.1}$$

with I_0 the incoming light intensity, ρ the distance from the origin and J_1 a first-order Bessel function. This is a representation of the so-called Airy-disc.

To resolve two different point sources, which turns out to be the sum of two Bessel functions, the minimal distance is reached when the maximum of the first function coincides with the minimum of the second one. This results in the Rayleigh-criterion [65] which reads as:

$$\Delta x = \frac{0,61\lambda}{n \sin \vartheta} \tag{3.2}$$

with the spatial resolution Δx, the wavelength λ, the refractive index of the medium n and the opening angle of the imaging objective ϑ.

As already mentioned, any point like source, for example a point dipole $\vec{\mu}$ imaged by an optical system will have a finite size. The reason for this is spatial filtering. While the original point source has an infinite spectrum of k-vectors in x and y, most of them, especially the long k-vectors associated with evanescent waves: $(k_x^2 + k_y^2) \geqslant k^2$ are filtered out. This effect limits the optical resolution. If we want to increase it, we have to increase the spread in the k-vector, this is a simple consequence of the Heisenberg uncertainty equation:

$$\Delta x \Delta k_x \geqslant \frac{1}{2} \tag{3.3}$$

with Δx the uncertainty in the location and Δk_x the uncertainty in the wave vectors. It follows that in order to decrease the spread in x, thereby increasing the resolution, we have to increase the spread in k:

$$\Delta k_x \geqslant \frac{1}{2\Delta x} \tag{3.4}$$

One way of increasing the spread in $\vec{k}$ is the use of an objective with a high numerical aperture. However, a limit for Δk_x seems to be the overall magnitude of k: $|\vec{k}|$. If we want to increase it beyond, i.e.: $k_x > |\vec{k}|$ it follows that one component, for example k_z reading:

$$k_z = \sqrt{\vec{k}^2 - k_y^2 - k_x^2} \ , \tag{3.5}$$

becomes imaginary. An imaginary wavevector in z means that the wave is damped exponentially and is not propagating in that direction – we enter the regime of evanescent waves and the near-field.

3.2.2. Electrical field enhancement

Plasmon frequency

Plasmons are quasi-particles and stand for the density oscillations of electrons, for example in metals. To describe them we begin with a simple model for an electron oscillator driven by an electromagnetic wave:

$$m_0\ddot{\vec{r}} + \underbrace{2m_0\gamma\dot{\vec{r}}}_{\text{damping factor}} + \underbrace{m_0\omega_0^2\vec{r}}_{\text{restoring force}} = \underbrace{-e\vec{E}_0e^{-i\omega t}}_{\text{exciting field}} \tag{3.6}$$

where m_0 is the electron mass, $\vec{r}$ the position with its first and second derivatives, γ a damping constant, ω_0 a frequency related to the binding spring constant, e the unit charge, $\vec{E}_0$ the initial electric field strength, t the time and ω the incoming wave's frequency. With solution for $\vec{r}$ the polarization $\vec{P}$ reads as:

$$\vec{P} = e\vec{r} = \frac{\frac{e^2}{m_0}\vec{E}_t}{\omega_0^2 - \omega^2 - 2i\gamma\omega} \ . \tag{3.7}$$

Using equation (3.7), the model of a free electron gas ($\omega_0 \to 0$), and the case of low damping ($\omega >> \gamma$) we obtain for the complex dielectric function $\epsilon(\omega) = \epsilon' + i\epsilon''$:

$$\epsilon(\omega) = (1 - \frac{\omega_p^2}{\omega^2}) + i\frac{Ne^2\gamma}{\epsilon_0 m_0 \omega^3} \tag{3.8}$$

with the plasmon frequency:

$$\omega_p^2 = \frac{Ne^2}{\epsilon_0 m_0} \tag{3.9}$$

and N the number of electrons and ϵ_0 the electric constant.

Surface plasmons

Surface plasmons are collective surface charge oscillations first reported in 1957 [66]. To derive the conditions for their creation we consider an interface between two media in the x-y-plane, with the indices 1 and 2 respectively. An electromagnetic wave with p-polarization is inbound. For this situation the wavevectors have the following relations:

$$k_x^2 + k_{1,z}^2 = \epsilon_1 k^2 \tag{3.10}$$

$$k_x^2 + k_{2,z}^2 = \epsilon_2 k^2 \tag{3.11}$$

with the wavevector's x-component k_x parallel to the interface being conserved, the z-component k_z perpendicular to the interface and the dielectric functions ϵ of the two media. With further use of the Maxwell equation for source free displacement fields: $\nabla \cdot \vec{D} = 0$, the boundary conditions for matching parallel components of the electric field $\vec{E}$, and the perpendicular component of the displacement field $\vec{D}$ we get to:

$$E_{1,x} - E_{2,x} = 0 \tag{3.12}$$

$$\epsilon_1 E_{1,z} - \epsilon_2 E_{2,z} = 0 \; . \tag{3.13}$$

Using equations (3.10) and (3.11) this leads to the dispersion relation:

$$k_x^2 = \frac{\epsilon_1 \epsilon_2}{\epsilon_1 + \epsilon_2} \frac{\omega^2}{c^2} \tag{3.14}$$

with the frequency ω and the speed of light c. In addition, one obtains the relation for the z-component of the wavevectors:

$$k_{1,z}^2 = \frac{\epsilon_1^2}{\epsilon_1 + \epsilon_2} \frac{\omega^2}{c^2} \tag{3.15}$$

$$k_{2,z}^2 = \frac{\epsilon_2^2}{\epsilon_1 + \epsilon_2} \frac{\omega^2}{c^2} \; . \tag{3.16}$$

If we want to obtain solutions traveling in x-direction and bound to the z-direction with the assumption of small imaginary parts (for small damping effects) we get for the dielectric functions:

$$\epsilon_1(\omega) \cdot \epsilon_2(\omega) < 0 \tag{3.17}$$

$$\epsilon_1(\omega) + \epsilon_2(\omega) < 0 \; . \tag{3.18}$$

These conditions, i.e. big negative values of the real part and small values for the imaginary part of $\epsilon(\omega) = \epsilon' + i\epsilon''$ are true for metals, especially for gold and silver in the visible regime. Figure 3.2 shows the values of ϵ' and ϵ'' for gold and silver dependent on the light's energy [67].
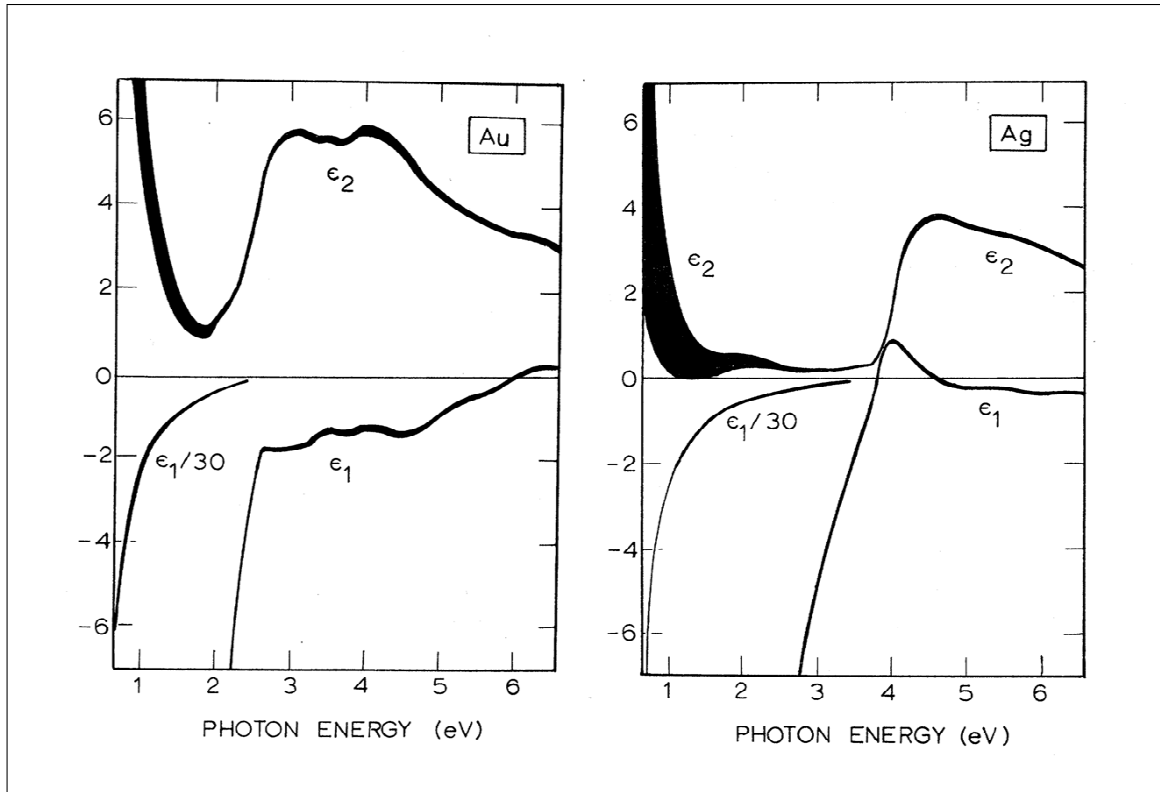
Figure 3.2.: Values for the dielectric functions $\epsilon(\omega) = \epsilon_1 + i\epsilon_2$ of gold and silver versus photon energy from [67].

3.3. Experimental issues

3.3.1. Application of metal nanoparticles

For the SERS experiments spherical gold and silver nanoparticles from British Biocell[1] were used [68]. They were directly applied to the sample from its liquid solution. After the dry-out of the solvent singled or packs of metal nanoparticles can be identified. See figure 3.3 for a SEM view of 250 nm gold particles on a silicon sample.
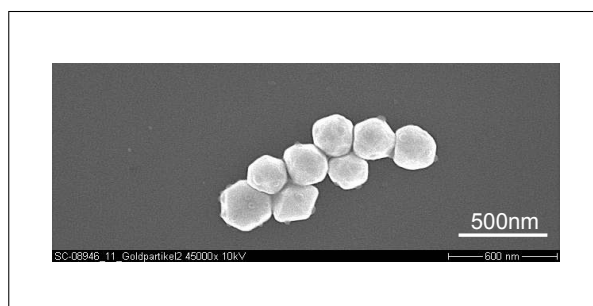
Figure 3.3.: SEM view of 250 nm gold nanoparticles on a silicon sample.

Via the video camera on the Raman tool the position of individual nanoparticles was obtained and they could be brought into match with the reflection of the laser beam. Then single spectra, linescans or two dimensional maps were recorded. The principle of taking so called SERS maps is shown in figure 3.4. The sample is scanned relative to the laser spot, when a gold nanoparticle gets into the spot the Raman signal can be enhanced.
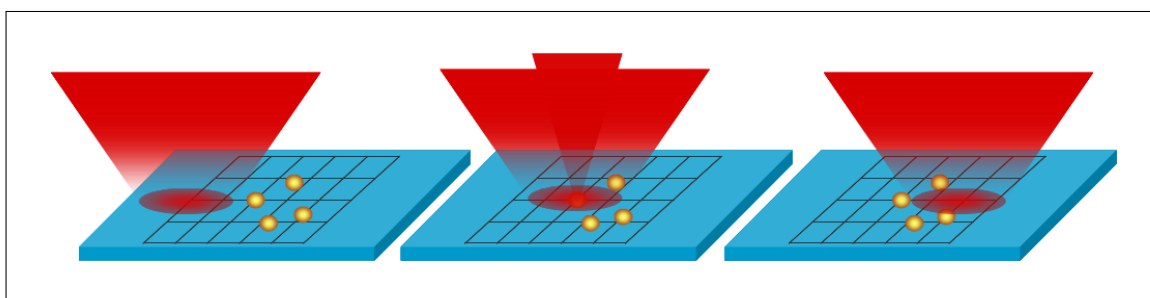
Figure 3.4.: Principle of taking SERS maps. The sample is scanned relative to the laser spot, with nanoparticles inside the spot, the signal is enhanced.

---

[1]British Biocell International Ltd., United Kingdoms, http://www.britishbiocell.co.uk/

3.3.2. Scanning probe

In this work several scanning probes were used. All of them were purchased from Nanonics[2] and vary in tip diameter, coating and gluing. The used feedback mechanism relies on the tuning-fork principle [69]. A silicon oxide tip is glued parallel onto one prone of a quartz tuning fork. The silicon oxide tips are cantilevered probes which are bend towards the end [70]. This ensures that the tip shadows the laser beam as little as possible. For the same reason the upper prone is shortened a little. In order to compensate this mass loss a glue droplet is applied. In a SEM view in figure 3.5 the shortened upper prone with the glue droplet can be seen as well as the small bent glass tip glued to the lower prone (red arrow).
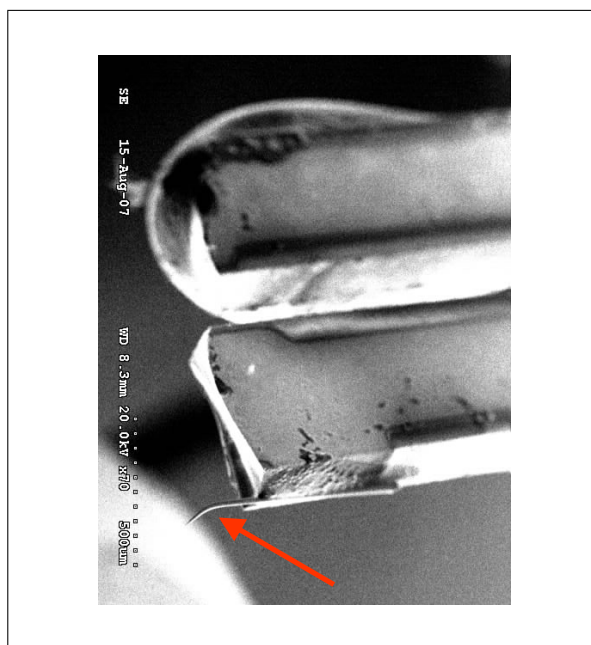
Figure 3.5.: SEM view of the front part of a tuning fork with mounted glass tip.

The tuning fork is excited with its resonance frequency (30 to 45 kHz) and the amplitude and phase of its oscillation are measured. The combined tip-tuning-fork system is then approached to the surface with a stepper motor. As soon as the predefined amplitude or phase offset is reached, the stepper motor stops and the system goes into feedback. The tip- or sample-piezo movement in z-direction is determined by the controller. A scheme of the setup can be seen in figure 3.6.

[2]Nanonics Imaging Ltd., Israel, http://www.nanonics.co.il/
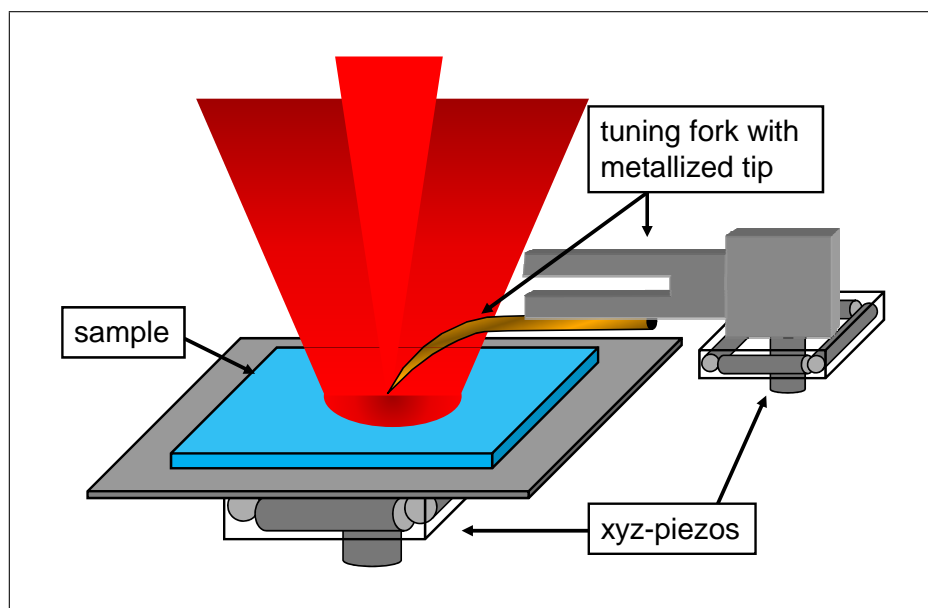
Figure 3.6.: Scheme of the TERS setup with a metalized tip glued onto a tuning fork.

3.3.3. Tip picking

Three different types of tips were used. The standard uncoated silicon oxide tips were used if only topography scans were needed, as well as for reference measurements. The second type of tips was coated either with a 20 to 50 nm silver or gold layer. In the case of the gold coating a thin chromium layer was used for adhesion purposes. Coated tips were all produced by sputtering and obtained from Nanonics directly.

To get better reproducibility and to transfer from SERS to TERS in an elegant way we went over to the process of tip picking, where small metal nanoparticles are attached to a tip and form a highly localized metal antenna. It is based on an idea by Kalkbrenner [71]. Tip picking was done on a modified Axiovert200[3] with white light illumination at the *Institut für Angewandte Photophysik (IAPP)* in Dresden. At first a small droplet from the gold nanoparticle solution [68] is applied onto the sample. The tip is functionalized by a glueing molecule, in our case Aminopropyl-trimethoxysilan (APTMS). The basic principle of the chemical bond lies in different functional groups in this molecule. On the one termination amino groups (NH_2) bind to gold or silver and on the other end a siloxane group couples to silicon oxide [72].

The picking procedure is shown in figure 3.7. First the sample is moved until a

---

[3]Axiovert 200, Carl Zeiss GmbH, http://www.zeiss.de

gold particle appears in the focus. After that the tip is carefully approached to the sample and brought into the focus above the particle by feedback mechanism or careful manual z-piezo movement. Then it is lifted up again. If the particle has vanished from the focus, chances are high that it is now applied to the tip.
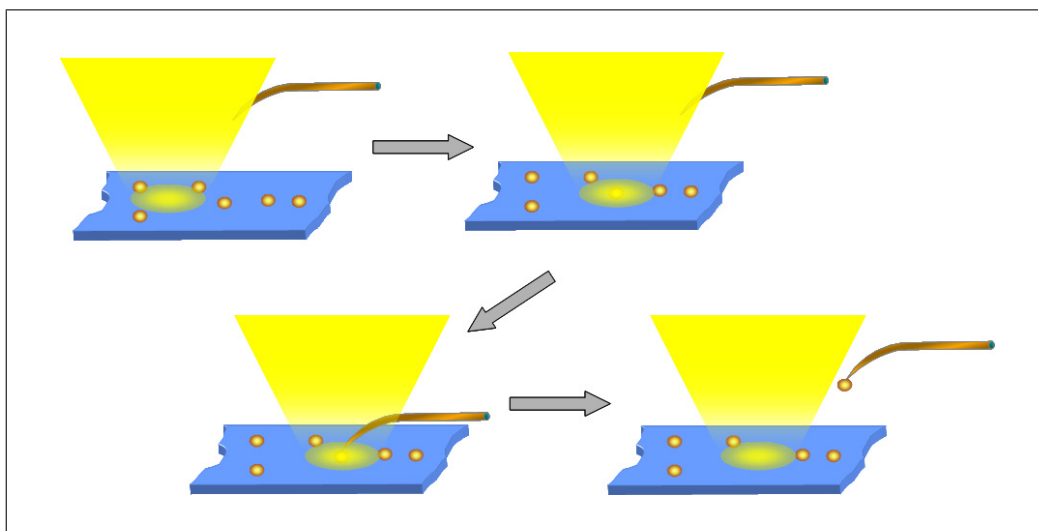
Figure 3.7.: Scheme of the picking procedure, where a metal particle is applied onto a glass tip.

By this method 100 and 250 nm gold particle were applied to silicon oxide tips. SEM views of 100 nm gold particles picked onto a glass tip can be seen in figure 3.8.
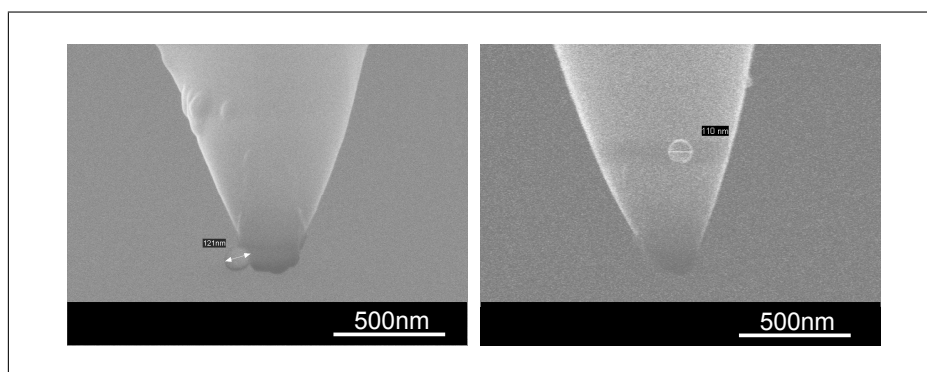
Figure 3.8.: SEM view of 100 nm gold particles picked on a glass tip.

3.3.4. Samples

For the SERS experiments unstructured standard silicon and stacked strained silicon on silicon-germanium samples were used. The stack consists of a thin 11 nm surface layer of silicon strained by an underlying two micron thick layer of silicon-germanium, followed by two microns of graded silicon-germanium on a silicon substrate. For TERS measurements a stacked sSoI sample was used. It consists of a 20 to 70 nm thin strained silicon surface layer on a 150 nm thick silicon-oxide layer on a silicon substrate. A schematic view can be seen in figure 3.9. The details of the fabrication process of strained silicon on silicon-germanium (sSi-SiGe) and sSoI can be found in the literature [25]. The strained silicon pads for the TERS linescans were structured by electron beam lithography and reactive ion etching.
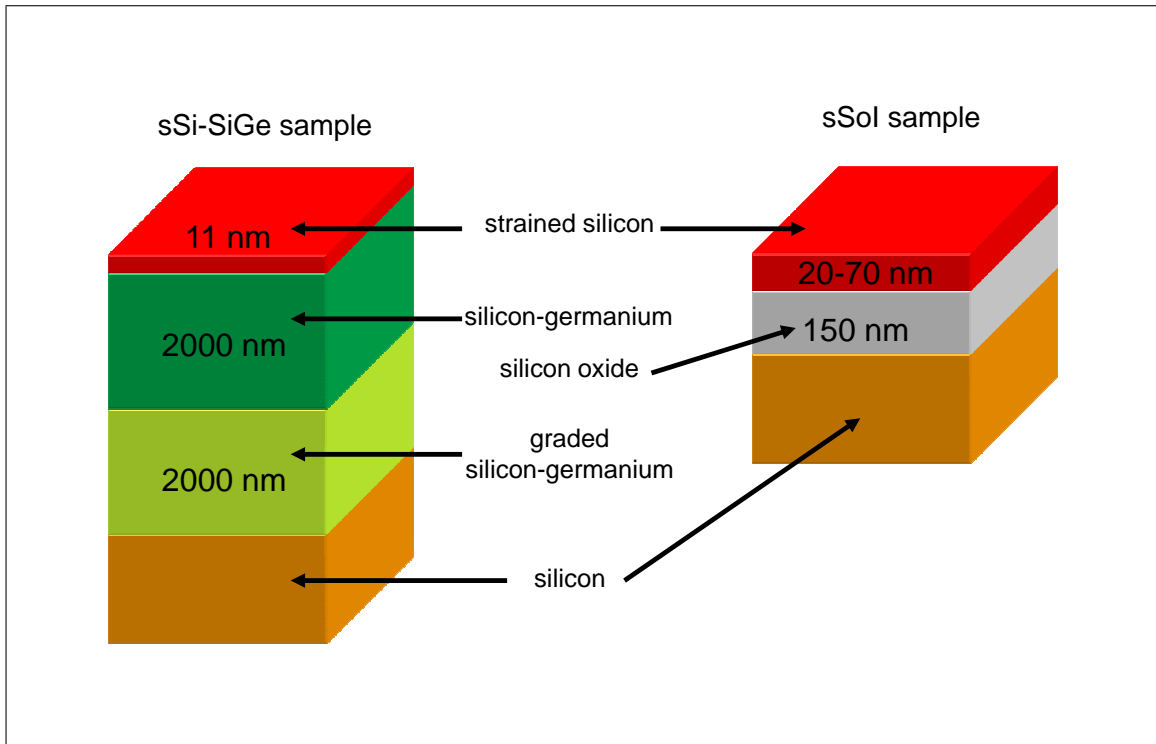
Figure 3.9.: Schematic view of the used sSoI and sSi-SiGe samples.

3.4. Findings

3.4.1. SERS experiments with metal nanoparticles

Size variation

To study the size dependence, three different types of gold nanoparticles were deposited on a silicon sample. With the help of the optical microscope a suitable area was found and SERS maps were taken. The results can be seen in figure 3.10.
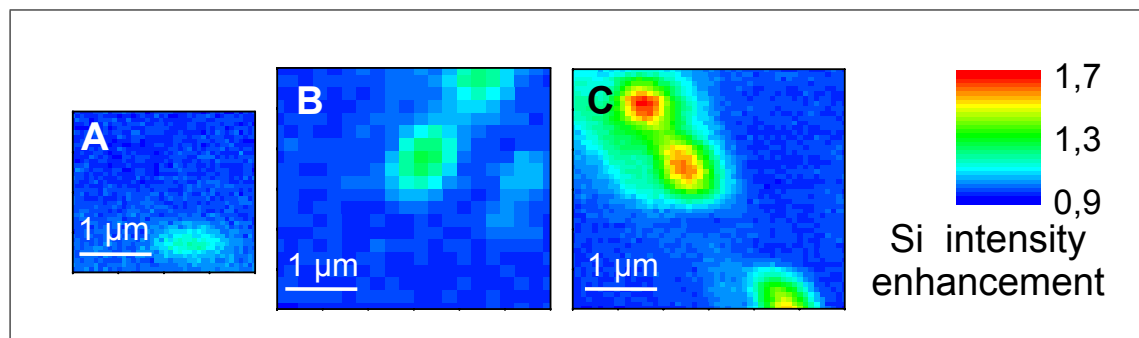
Figure 3.10.: SERS maps of gold particles on silicon showing the intensity enhancement of the silicon peak. Size of particles: *A:* 80 nm (green laser = 532 nm), *B:* 100 nm (green laser), and *C:* 250 nm (red laser = 633 nm). Bigger particles give higher enhancements.

The intensity of the silicon peak fitted by a Lorentz function at each scan position is divided by the average silicon intensity without any particles nearby. By this we obtain a peak intensity enhancement which can be compared between the measurements.

With the 80 and 100 nm gold particles showing only enhancements of $\approx 20\%$, we can increase the silicon peak intensity by up to $\approx 100\%$ by using 250 nm gold particles.

The size dependence is not surprising because bigger particles offer a much bigger scattering volume thus increasing the signal enhancement. The used laser wavelength was chosen to match the particle's plasmon resonance as much as possible. This dependence is discussed in the next but one subsection.

Polarization setting

In a next step the polarization setup was changed, as can be seen in figure 3.11. Three polarization settings: A, B, and C are illustrated. In all cases the laser emits light linearly polarized in x-direction. For setup A it passes a $\lambda/2$ waveplate without any change. After passing the sample the major part of the Raman scattered light, attributed to the far-field signal, is polarized in the same direction because of the strongly polarized LO phonon mode. But there are also components polarized in different directions due to scattering at the particles, i.e. polarized in y-direction. Passing the diffraction grating leaves the components parallel to the grooves unaltered while the components perpendicular to them are damped. Case B shows the situation when the $\lambda/2$ waveplate rotates the laser polarization, so that we obtain light polarized in y-direction. Now the components which are damped the most by the grating correspond to far-field scattering. Hence the contrast between near-field and far-field is increased. Finally as shown in setup C we can introduce a polarizing filter oriented in x-direction and get completely rid of the far-field parts.
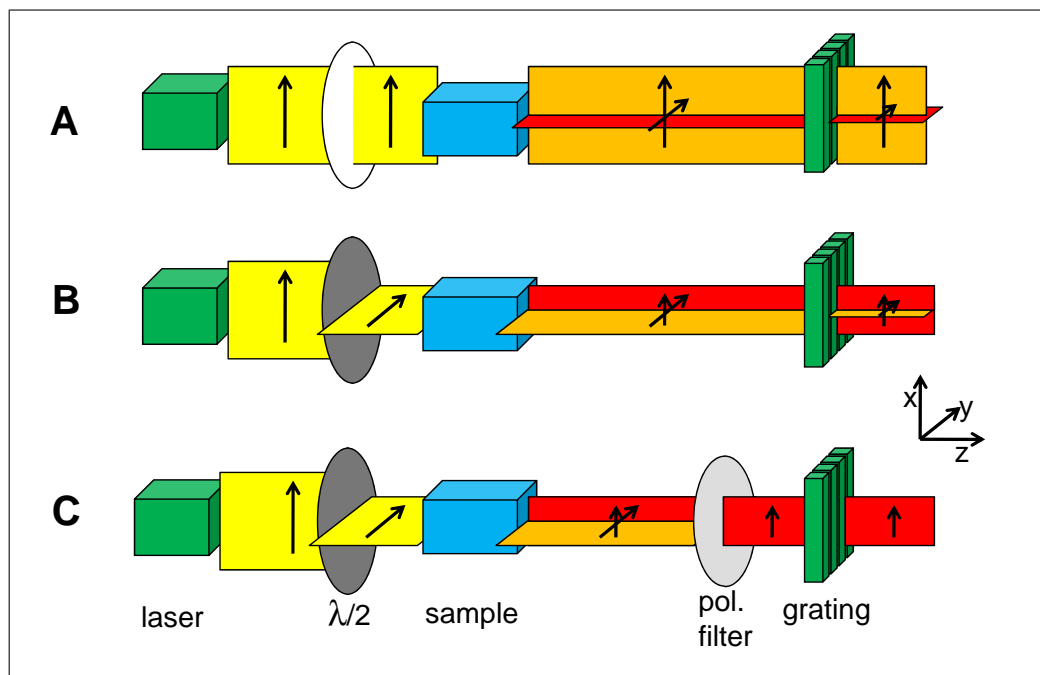
Figure 3.11.: Different setups used for polarization dependent measurements: *A:* incoming laser light parallel, *B:* perpendicular to diffraction grating grooves and *C:* with additional polarizing filter. Incident laser light is shown in yellow, far-field scattered parts in orange and near-field scattered parts in red color.

SERS maps of 100 nm gold particles on silicon are shown in figure 3.12. Changing the polarization setting from case A (left map) to B (middle map) results in a contrast increase between silicon intensity with and without particles from 50% to 100%. By using a polarization filter in setup C, we can further increase this effect to up to 250%, this can be seen in the right map.
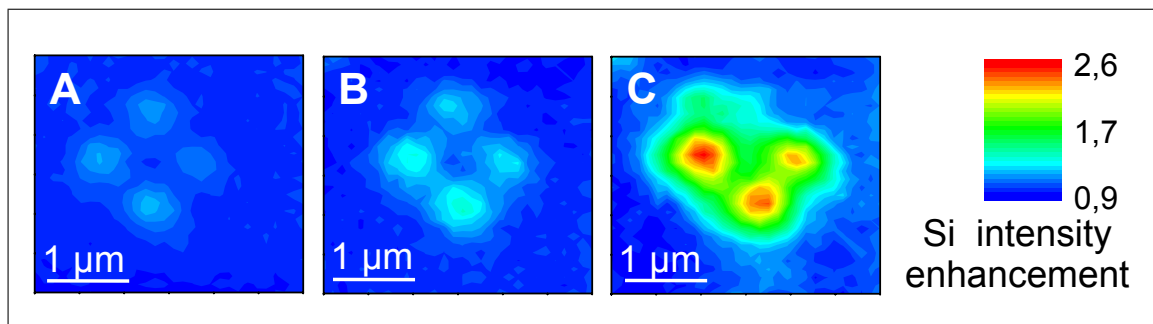
Figure 3.12.: SERS maps of gold particles on silicon showing the intensity enhancement of the silicon peak. Green laser used, polarization of the incoming light: *A:* parallel, *B:* perpendicular to grating grooves and *C:* with additional polarizing filter. Suppressing the far-field parts of the Raman light leads to increased signal contrast.

This observed contrast gain is a background suppression effect, rather than an improvement in absolute signal intensity. The reason for this is, that the grating used to diffract the Raman scattered light onto the detector acts as a polarizer which suppresses light being perpendicular to its grooves. So the far-field part of the light can be suppressed by changing the incoming laser polarization or by introducing a polarizing filter in the Raman scattered beam patch. The metal nanoparticle on the sample surface then acts as a depolarizer thus generating different polarizations which can reach the detector. In short, the far-field portions of the light are much more inhibited than the near-field parts, which appears then as a contrast increase.

Wavelength dependence

An important issue in SERS is the choice of a suitable laser wavelength. In figure 3.13 three SERS maps of 100 nm gold particles irradiated with blue (488 nm), green (532 nm) and red (633 nm) light is shown. An increase in peak intensity is only visible for green and red light, while for blue laser irradiation the intensity of the silicon near the gold particle decreases.
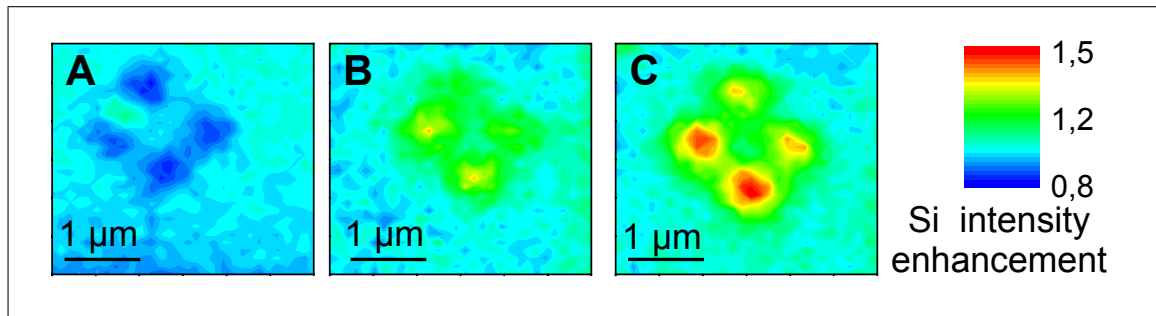
Figure 3.13.: SERS maps of 100 nm gold particles on silicon showing the intensity enhancement of the silicon peak. Incident wavelength varied: *A:* blue (488nm), *B:* green (532nm) and *C:* red (633nm). An intensity Enhancement is only for green and red laser visible.

White-light backscattering spectra of 80 nm and 100 nm gold particles are shown in figure 3.14. The intensity of the backscattered light is normalized and plotted over the wavelength. The plasmon resonances at 570 nm and 600 nm respectively are shown. Note the size dependent red-shift for the bigger particle; the positions of the three available laser wavelengths for the Raman measurements are also included. When looking at the results from the SERS maps, a direct correlation to the white-light backscattering spectra can be seen. Only for wavelengths near the plasmon resonance peak an enhancement is present. It should be pointed out that the backscattering spectra were taken with gold nanoparticles on glass, and a slight red-shift in peak resonance is expected when dealing with high refractive index materials like silicon because the plasmon resonance is dependent on the surrounding medium [73].
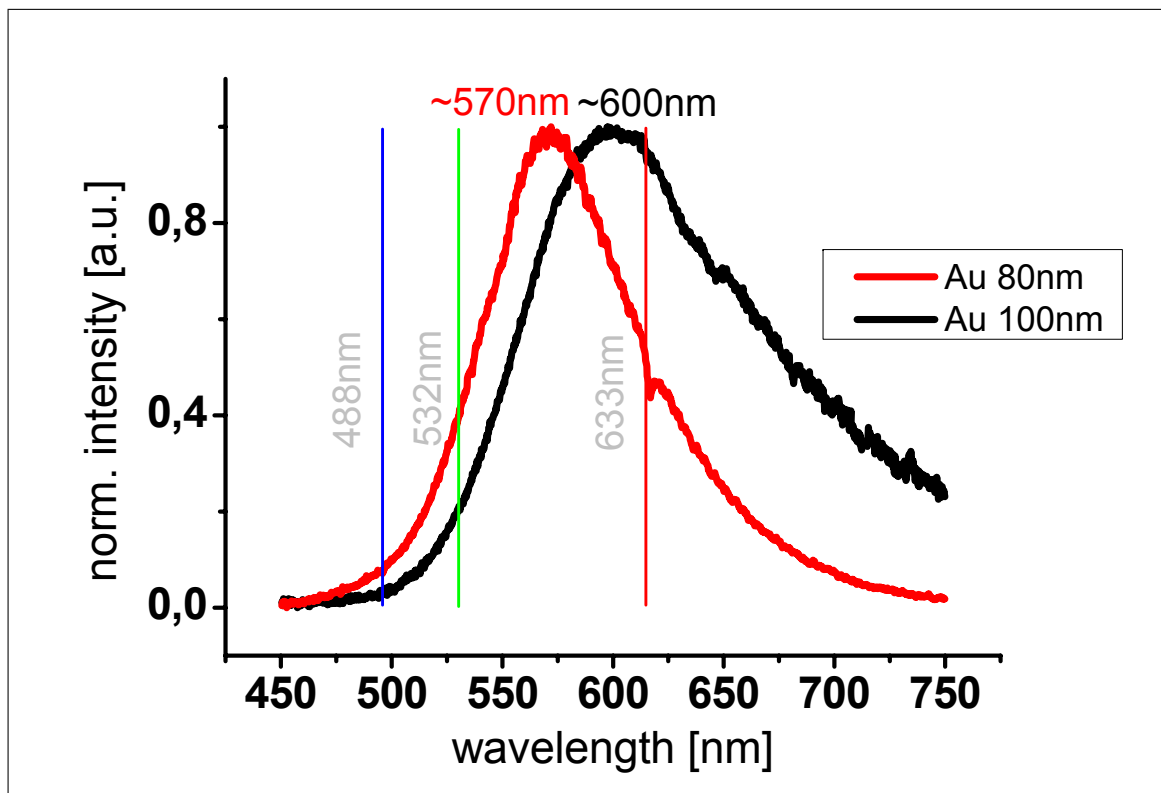
Figure 3.14.: Normalized white-light backscattering spectra of 80 nm and 100 nm gold nanoparticles in air on a glass substrate, resonance peaks and available laser wavelengths shown.

Enhancement localization

To check if the observed Raman intensity enhancements are localized, a stacked sSi-SiGe sample was used. Spectra with and without particles in the laser spot were taken for 100 nm and 250 nm gold spheres respectively. The resulting spectra are offset to matching bulk silicon peak intensities and can be seen in figure 3.15. The peak of the thin strained silicon surface layer at around 516 cm^{-1}, barely visible in the black far-field spectrum, increases significantly. Another effect is the greatly increased background in the near-field spectra, notice the different intensity scales for far-field and near-field spectrum.
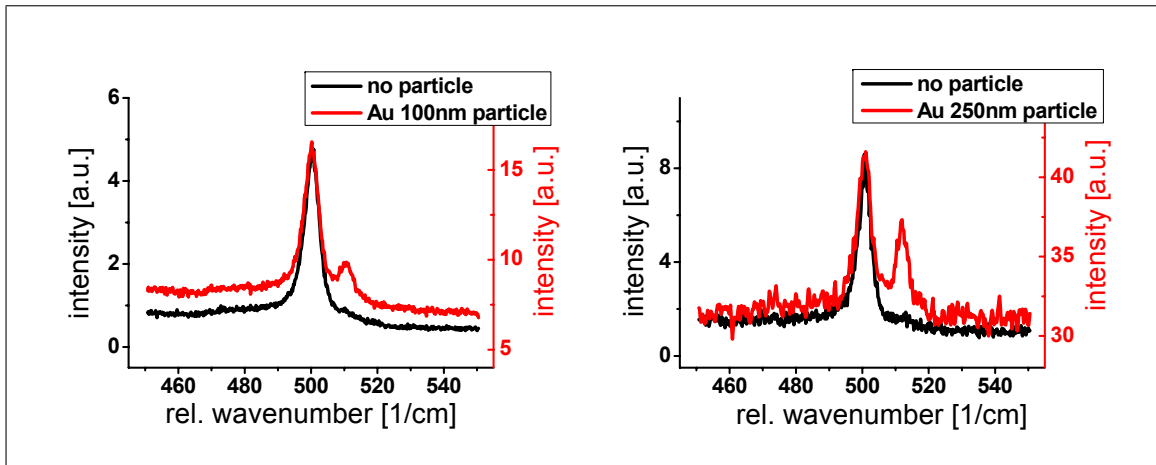
Figure 3.15.: Normalized Raman spectra of layered sSi – SiGe sample without (black) and with gold particle inside laser focus (red). *Left:* 100 nm particle, *Right:* 250 nm particle. The strained silicon peak at 516 cm^{-1} is clearly enhanced.

The higher background and slightly increased signal to noise ration in the near-field spectrum with the 250 nm gold particle is attributed to an increased fluorescence which overlaps the Raman signal.

To correlate the nanoparticle induced changes in the Raman spectrum to a distinct particle coverage, a large SERS map was taken from a specific sample region which was studied with dark-field light microscope and SEM before. Several single particles as well as particle accumulations from 250 nm gold nanoparticles can be seen in figure 3.16.
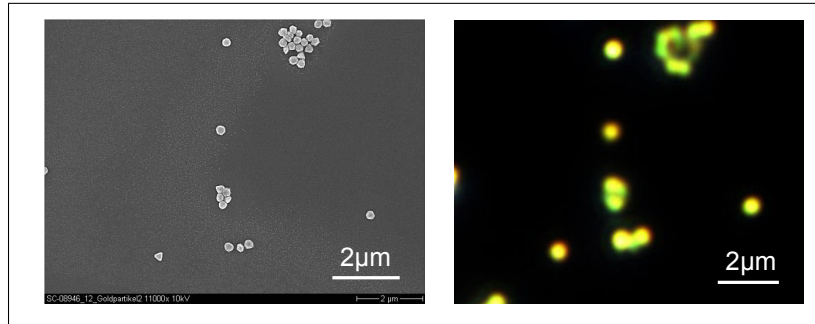
Figure 3.16.: *Left:* SEM view of 250 nm gold particles on sSi-SiGe, *Right:* same area under dark-field microscope.
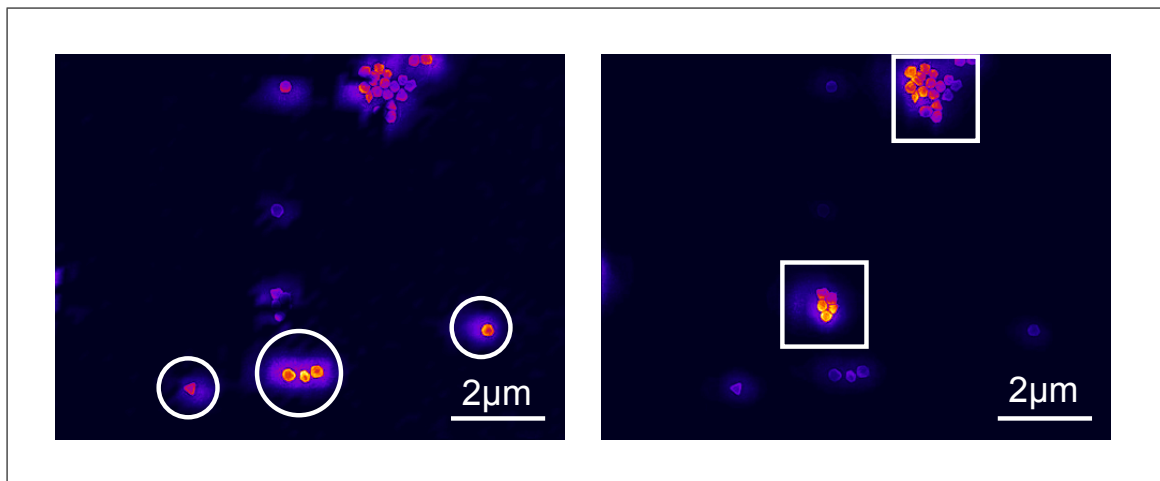
Figure 3.17.: Matrix overlays of detailed SEM information with SERS maps of 250 nm gold particles on a sSi-SiGe sample *Left:* Peak intensity enhancement of the surface strained silicon layer and *Right:* amount of spectral background. Regions of high peak enhancement coincide with single particles (white circles) and high background areas are localized at clusters of particles (white squares).

Raman spectra were taken in this region every 200 nm and analyzed concerning peak intensity and frequency of the silicon-germanium and the strained silicon peak as well as the background level. For better visualization the SEM

views and the spectral data from the Raman maps were overlaid by graphic matrix multiplication. The results can be seen in figure 3.17. Single spots of high strained silicon peak enhancements can be directly related to single gold nanoparticles (white circles in left picture), while particle clusters mainly lead to an huge increase in the background (white squares in right picture).

When looking at the frequency of the silicon-germanium peak, a considerable shift can be correlated to the coverage with gold nanoparticles. In figure 3.18 this peak shift is plotted, frequency changes by as much as 1.3 cm^{-1} are visible mainly in the regions with multiple particles (see black circles). The peak shifts from the strained silicon layer showed similar results but interpreting the fitted peak shifts is rather difficult due to the low peak intensity. These peak shifts
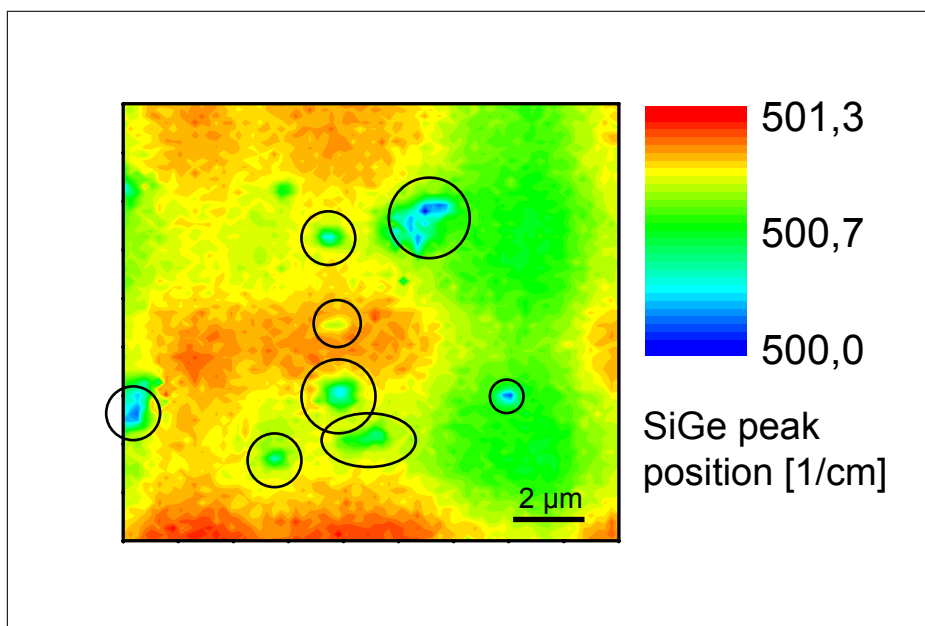
Figure 3.18.: SERS map of 250 nm gold particles on sSi-SiGe sample. Fitted peak position of the SiGe shown. Black circles indicate positions of gold nanoparticles causing peak down shift.

indicate some kind of stress in the SiGe layer. Because a mechanical reason is unlikely (the low mass of the nanoparticles won't result in a significant pressure just by lying on the sample) it is assumed to be a temperature effect. Due to light scattering, the gold particles can heat the underlying materials which causes changes in the microstructure and hence the peak shift.

Particle material

Apart from gold, there is another metal showing plasmon resonances in the visible regime. Thus, silver nanoparticles were studied in a similar fashion like the gold nanoparticle SERS experiments. In figure 3.19 three pairs of spectra, one spectrum without silver particle and one with silver nanoparticle in the laser focus are shown. Due to availability the diameter was chosen to 80 nm and the laser wavelength was changed. For all wavelengths an increase in strained silicon intensity is observed, but the largest effect can be seen with green excitation.
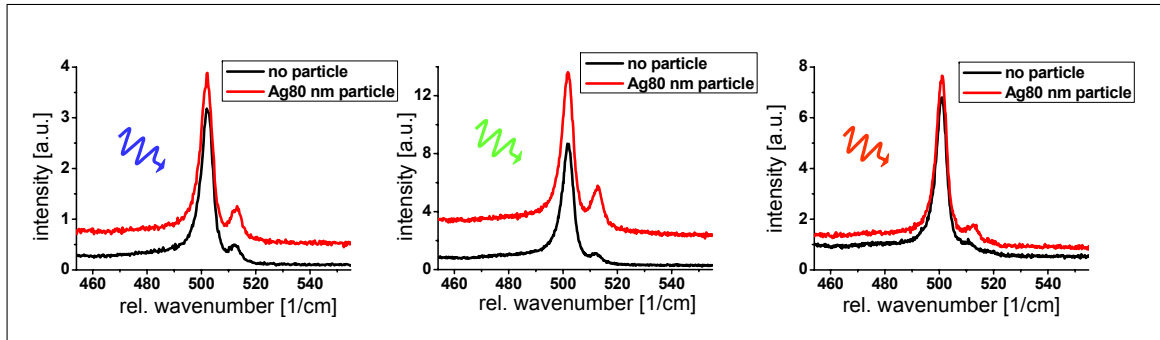
Figure 3.19.: Far-field (black) and near-field (red) spectra of sSi-SiGe sample. 80 nm silver particle illuminated with *Left:* blue = 488 nm, *Middle:* green = 532 nm and *Right:* red = 633 nm laser.

Although the resonance wavelength for 80 nm silver particles theoretically matches the wavelength for the blue laser [73] the relative enhancement of the strained silicon peak is also observed in the measurement with the green laser. The reason for this might be that it was not possible to distinguish singled particles with the microscope, and that it is more likely that accumulations of multiple particles have actually been illuminated with the laser.

3.4.2. TERS results

TERS measurements were done with silver coated glass tips with a diameter from 100 to 200 nm after coating, the diameter were measured from SEM views. As already stated, the near-field enhancement is strongly localized and has a much lower penetration depth than the far-field scattered Raman signal. If a sample is used, where the Raman peak of a thin surface layer can be distinguished from the Raman peak of a deeper lying substrate, a differentiation between the near-field signal and the far-field signal can be achieved. Thus, a layered sSoI sample is used in the following measurements. In figure 3.20 two spectra are shown, the black one is the normal Raman spectrum of the sample and the red one is the spectrum with the metalized tip moved into the laser spot. The incident laser wavelength was chosen to 488 nm to achieve good surface sensitivity. Two effects become visible: the bulk silicon peak at around 520 cm^{-1} decreases slightly and the strained silicon peak at around 515 cm^{-1} increases by more than 250%. Both peaks are fitted and shown in green for the strained silicon and blue for the bulk silicon respectively, the layout of the sample is depicted in the inset of the figure.
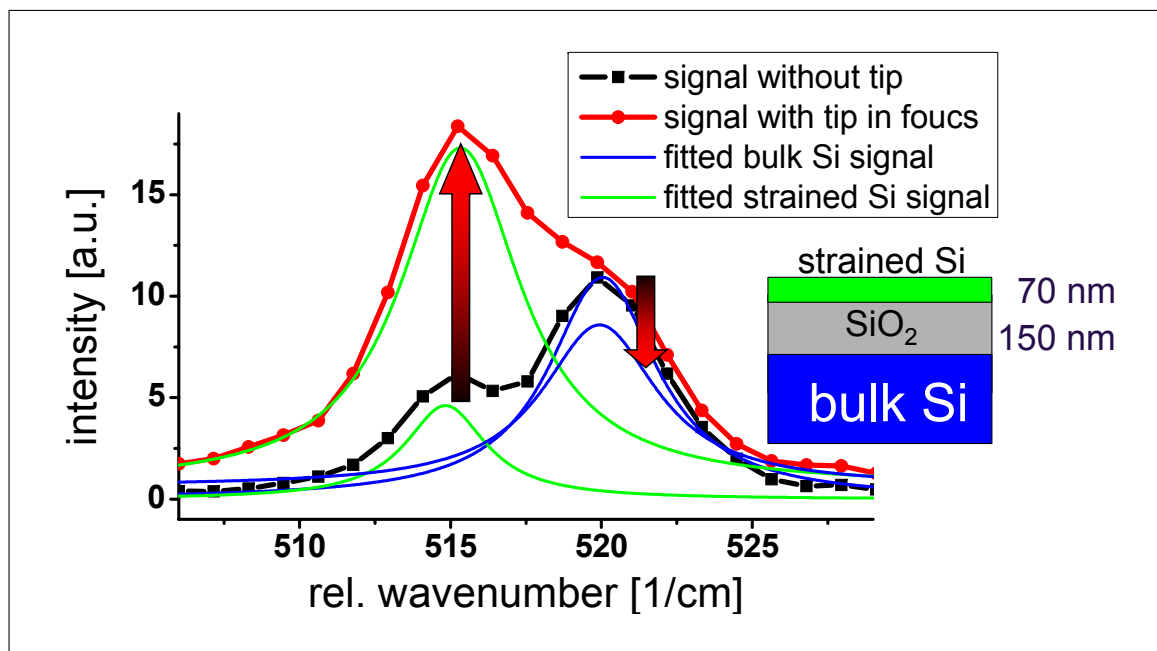
Figure 3.20.: Spectra from sSoI sample (see inset for structure) without and with silver coated tip inside laser focus. Fitted bulk silicon peaks (blue) and strained silicon peaks (green) shown. Notice the greatly increased strained silicon peak in the TERS spectrum.

To visualize the changes in Raman spectra of sSoI when moving a tip into the laser focus and to find an optimal spot inside the beam a so-called tip map was taken. The sample is kept in position while the tip is scanned inside the laser spot. The intensity of the fitted strained silicon peak at every scan position is mapped in figure 3.21 in the middle. Three locations of this tip map are examined. When the tip is completely inside the laser spot, shadowing is predominant. In consequence the total peak intensities decrease while the background increases due to light scattering at the tip. When just the tip apex is inside the laser spot, the electric field enhancement exceeds the shadowing. Thus, the peak intensities, especially of the near surface strained silicon layer, increase. If the tip finally is moved further to the right it leaves the laser spot and we get the normal far-field Raman spectrum of the sample.
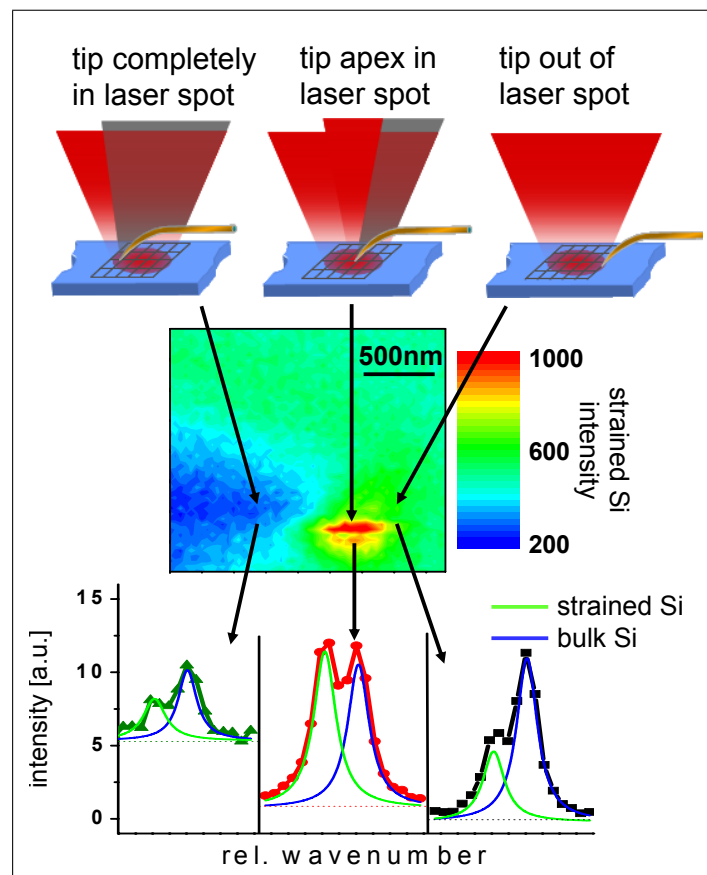
Figure 3.21.: *Top:* Tip position relative to the laser spot, *Middle:* Tip map showing the strained silicon intensity at every scan position, *Bottom:* Single spectra at distinct points of the tip map, showing peak intensities of bulk and strained silicon and background level.

Spatial resolution

To examine and improve the spatial resolution, a similar but structured sample, consisting of pads of strained silicon (see section 2.3.3 and figure 2.14) was used, a schematic cross section of the sample can be seen in the inset of figure 3.22. Linescans were done with and without a silver coated glass tip in contact. In figure 3.22 these scans is shown. The fitted intensity of the strained silicon layer is plotted versus the scan position. While we can barely see the structural periodicity in the far-field curve, it becomes clearly visible in the TERS linescan. As expected, the intensity reaches a maximum on top of the strained silicon pad, and it decreases in between them.
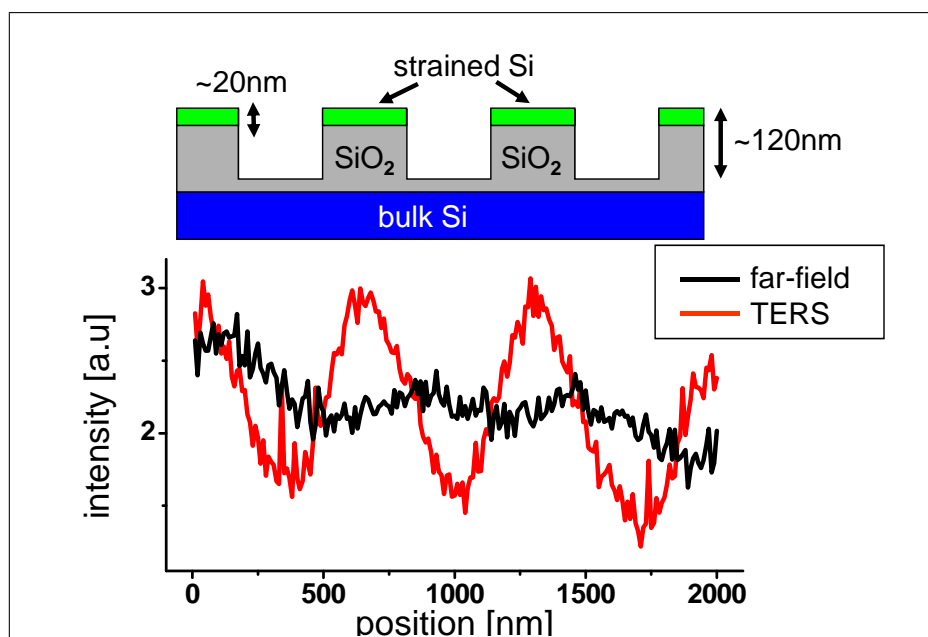
Figure 3.22.: Linescan over sSoI pads, fitted intensity of strained silicon plotted over scan position. Compared to the scan without tip (black) the periodicity of the structure becomes much more clearer in the TERS scan (red). The inset shows the sample structure.

As peak intensities are rather susceptible to topographic or focal artifacts the position of the peaks was also looked at. In figure 3.23 the fitted peak shifts are plotted, together with a smoothed average due to the noisy data. In the black far-field curve no alteration is visible, but in the red TERS scan one can resolve the structure's periodicity. If we keep in mind that the relative wavenumber for unstrained silicon lies at around $520 \, \text{cm}^{-1}$ we see that the most strained regions, i.e. lowest wavenumber, correspond to points directly on the pads. In contrast, less strained, i.e. higher wavenumbers, coincide with positions between the strained

silicon pads. This behavior is expected because the strained silicon pads can keep their intrinsic stress in their middle but relax it towards their edges.
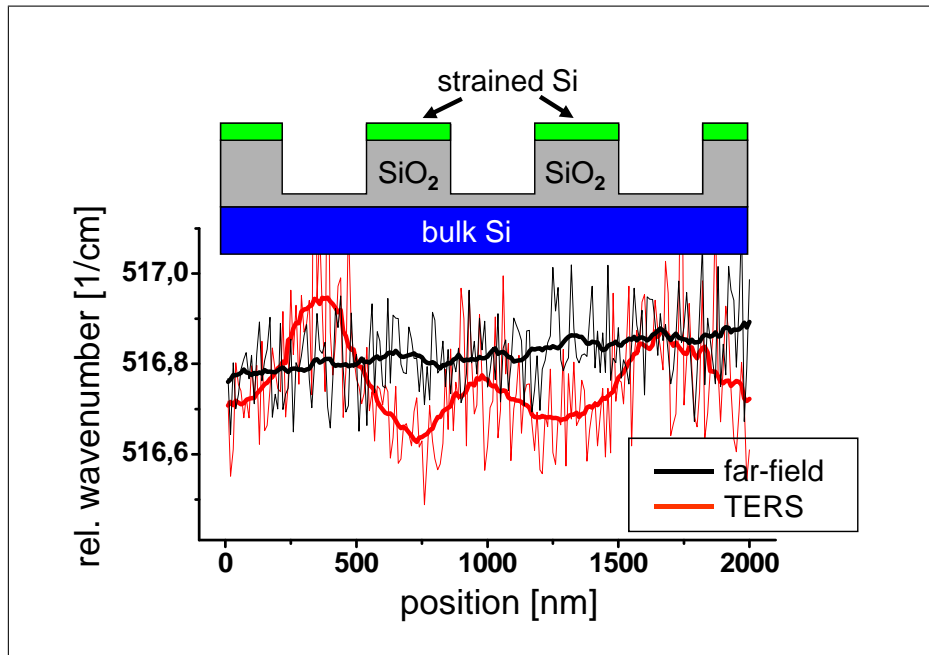

Figure 3.23.: Linescan over sSoI pads, fitted peak frequency of strained silicon plotted over scan position. The TERS scan (red) shows the expected higher wavenumbers, i.e. stress relaxation, at the pad edges. The inset shows the sample structure.

3.5. Remarks & Conclusion

3.5.1. SERS studies

In order to compare the Raman enhancement on semiconductor samples obtained by using metalized tips or tips with attached metal nanoparticles, experiments with metal nanoparticles *directly* deposited on the sample surface were conducted. Several parameters were varied to study their dependence on the Raman intensity increase and the range of the enhancement, namely the size and material of the particles, as well as irradiance properties, like the used wavelength or the polarization settings.

For the particles diameter it was found that bigger particles lead to much higher intensity enhancement factors. This result would lead to the idea of using big particles or broad tips for TERS measurements in order to get a high signal. However as the obtainable resolution will be in the order of the particle's radius we are again restricted. Thus a compromise between signal intensity and desired resolution has to be found for the specific application.

To increase the signal contrast between far-field and near-field contribution, the polarization setting can be altered. It was shown that the far-field part can be significantly suppressed by adjusting the Raman scattered beam perpendicularly to the diffraction grating. This dependence can be seen in figure 3.24.
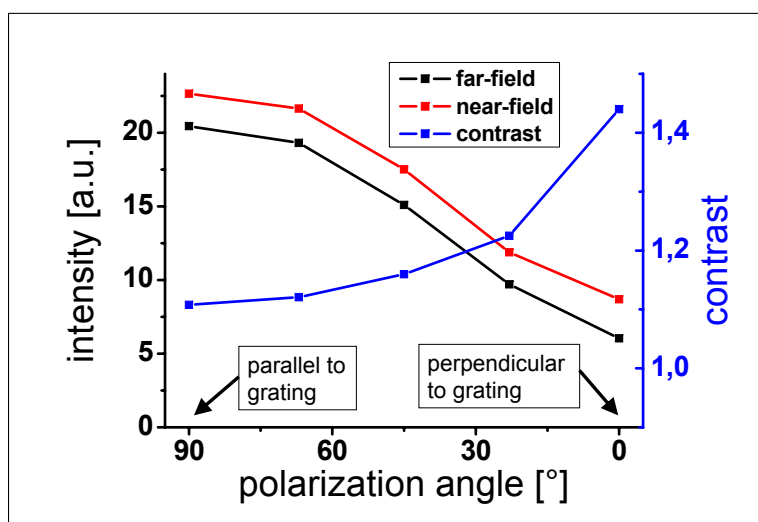
Figure 3.24.: Dependence of signal intensity of far-field and near-field contribution and contrast on the polarization angle (incident laser polarization in relation to grating orientation).

It should be clearly noted that this method won't increase any total *intensities*, it will increase the *contrast*. By suppressing the far-field, the near-field signal is suppressed as well, but by a smaller amount due to having many different polarization directions after scattering.

When speaking about the polarization in such experiments, the highest enhancements will be created with polarization components in the direction of the light's k-vector (z-direction) [74, 75]. In fact when illuminating particles or tips with purely linear polarized light, the enhanced electric field is situated at the particle's sides [76], barely penetrating the samples surface. There are two reasons why we get an increase in signal nevertheless. The first is that in the focus of a high numerical aperture objective there are always different directions of the k-vectors, and thus we also have electric field components in z-direction. The second is, that for large particles, i.e. more than 100 nm at the given wavelength, higher order modes and inteference effects take place [77, 78]. As a result, forward scattering that reaches the sample's surface occurs. This situation is illustrated in Fig. 3.25 in a very simplified sketch. The enhanced electric field surrounding gold nanoparticles illuminated by light is shown. For larger particles (compared to the incident wavelength) more of the enhanced regions can actually reach the sample and thus contribute to an increase in Raman signal.
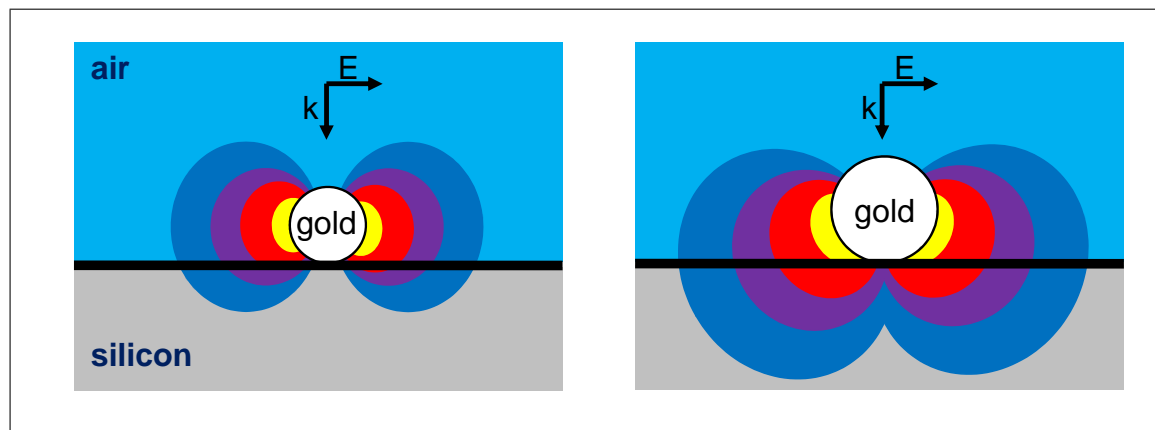
Figure 3.25.: *Left:* Illustration of the enhanced electric field around a small gold nanoparticle. *Right:* Electric field around a bigger gold nanoparticle penetrating larger parts of the sample.

Experiments with radially polarized light to greatly increase the amount of electric field components in z-direction were done with the help of a z-polarizer. It consisted of four lambda half waveplates rotated by 90 degrees which convert linearly polarized light into radially polarized light. After focusing through a high NA objective this produces z-polarized light [79]. Figure 3.26 schematically shows the principle of the z-polarizer. However, measurements with this device suffered from heavy intensity losses through beam deviation and scattering at the center intersections of the four waveplates, so no reliable data of signal enhancements could be collected.
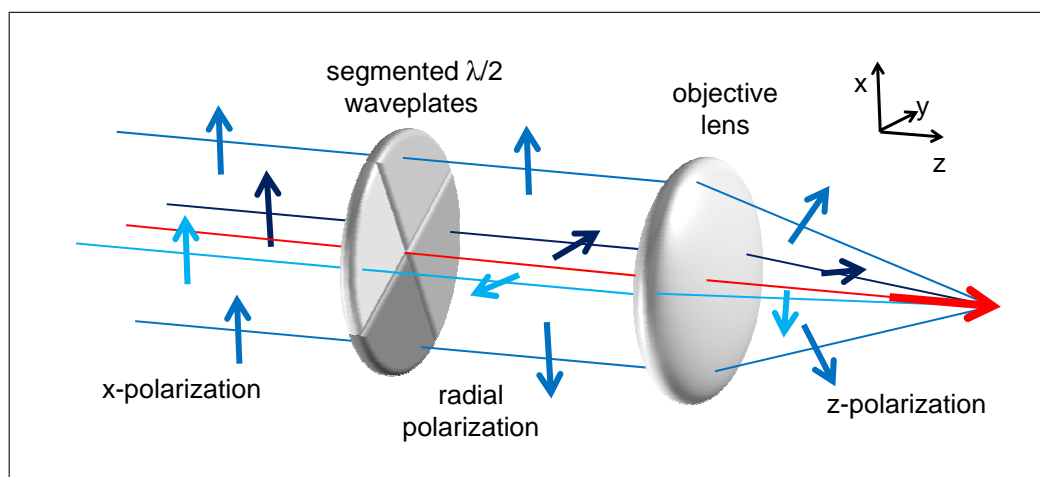
Figure 3.26.: Principle of creating light polarized in the direction of travel: The linearly polarized light is converted into radially polarized light with segmented λ/2 waveplates. After focusing by an objective lens this results in a polarization in z-direction.

The dependence of the incident wavelength on the Raman signal enhancement has been discussed. It has been shown that the results are similar to the white-light backscattering spectra of these particles. The reason for this dependence is the individual particle's plasmon resonance. The scattering spectra can be calculated by Mie-theory and the results are in good agreement with the measured spectra [73]. In fact, the scattering efficiency calculated by this method is related to the far-field. In the near-field regime, which is responsible for the localization confinement, the results are different and more complex. The main difference lies in the relations between different resonance modes, i.e. the dipole and the multipole modes [80]. However the position of the resonance peak, the resonance frequency, is similar which allows us to compare the wavelength dependency of the SERS enhancement with the scattering spectra.

It should be noted that the use of ambient media, like water or oil influences the plasmon resonance peak, both in height and position, higher index media will shift the resonance to longer wavelengths and increase the scattering efficiency [73].

Regarding the localization of the enhanced signal we could confirm the surface sensitivity by using stacked samples. Only the peak of the top most strained silicon layer was enhanced while the Raman signal of the underlying substrate changed barely. However this is only a statement about the depth range, for any conclusions regarding the lateral resolution improvement we have to look at the TERS results with the movable metalized probe.

3.5.2. TERS experiments

The TERS measurements with silver coated glass tips on sSoI samples showed clearly the selective enhancement of the Raman signal from the top strained silicon layer. It should be clearly stated that this enhancement is no pure near-field effect: it has different contributions. When moving a tip in the laser focus, several things have to be considered:

- decrease of Raman signal intensity by *shadowing* from the tip
- angle-dependent *changes* in the Raman *selection rules* by scattering
- change in the incoming *polarization* by scattering
- enhanced Raman signal by *local increase* of the electric field
- pick up of evanescent components at the sample surface

All of these effects have an impact on the resulting signal intensity. Special care has to be taken when measuring layered high refractive index materials such as the sSoI samples. It is possible that by reflections at the tip we get angle-dependent multiple scattering in the silicon-oxide layer which greatly alters the amount of Raman signal from the strained silicon layer [81]. Additionally, we can change any present polarization dependent signal suppression by scattering at the tip which could give as an increase contrast (see section: 3.4.1: Polarization setting).

The approach of picking metal nanoparticles on tips was chosen to circumvent the bad reproducibility of the coated tips, which showed significant differences in quality concerning diameter, sharpness and coating uniformity. Similar looking tips with equal diameters could give completely different enhancing results,

probably caused by the appearance of hot spots. In figure 3.27 SEM views of a silver coated tip used for TERS scans are shown. Apart from the bluntness and the protrusions at the apex the coating seems to have chipped off, probably due to heating of the tip's glass body by the laser. The rather large grains in the coating could also be responsibly for the appearance of hot spots.
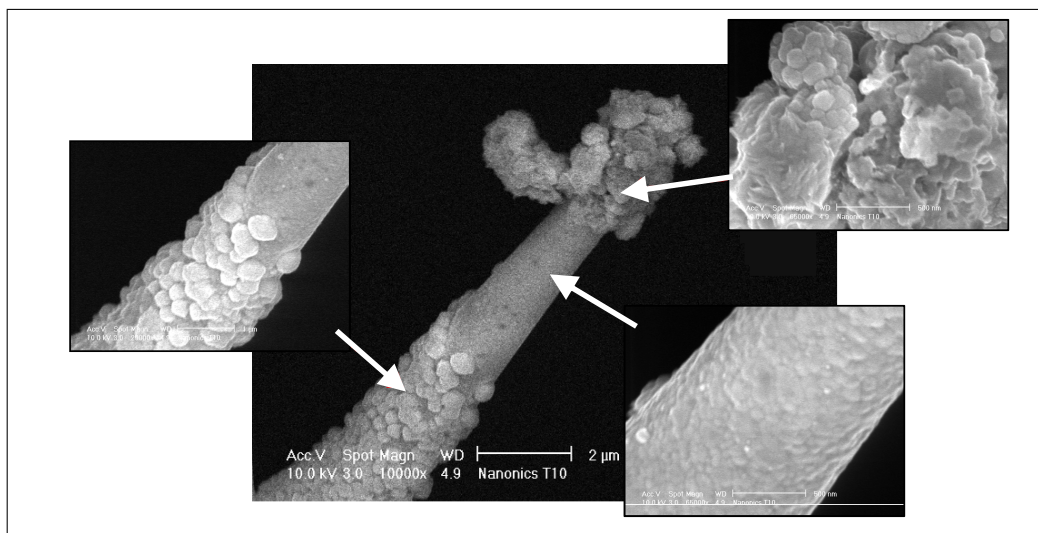

Figure 3.27.: SEM views of a silver coated tip used for TERS scans. The grained structure of the coating might favor the appearance hot spots. The middle part of the tip suffered from chip off of the coating, probably due to laser heating.

While the procedure of picking nanoparticles onto tips was successful, their use in TERS experiments proved to be rather unsatisfying. Tips with attached 100 nm gold particles delivered no signal enhancement on the silicon samples. Tips with attached 250 nm particles lost their particle after careful approach to the surface. Reasons for this are basically attributed to the scanning probe mechanism at the tool. The exponentially decaying enhancement of the electric field around the tip requires a small distance between probe and sample, preferably under 10 nm [82]. But because the tuning fork oscillates normally to the surface with an attached rather flexible glass tip, the minimum oscillation amplitude couldn't be lowered significantly under 50 nm with the existing controllers, so most time of the oscillation period the sample is out of the region of the increased field from the tip.

3.5.3. Improved resolution and artifacts

The TERS linescans on the structured sSoI sample imply an increased lateral resolution by showing both, periodicity in the signal intensity barely visible without metalized tip and periodicity in the peak shift, which was not visible without a tip at all. However one should be very careful when making statements about optical resolution, especially in the case of structured, i.e. topographic samples. Just by obtaining any variance in the intensity signal of a linescan one should not conclude an eventual highly localized near-field TERS effect. Due to the topography and the feedback mechanism the tip changes its position relative to the sample and also relative to the laser spot. This may introduce cross talk [48, section 7.3]. The following two pictures in figure 3.28 show an AFM scan of 50 nm wide trenches in a silicon sample to the left, and the corresponding Raman signal intensities at each scanning point to the right. By comparing the Raman pattern with the AFM pattern one could say we clearly resolved the 50 nm trenches, hence our resolution was improved to this value. The truth is, that the Raman map was taken with a simple glass tip, so no electric field enhancement is expected and the effect just results from the different scattering situations when the tip follows the topography in feedback.
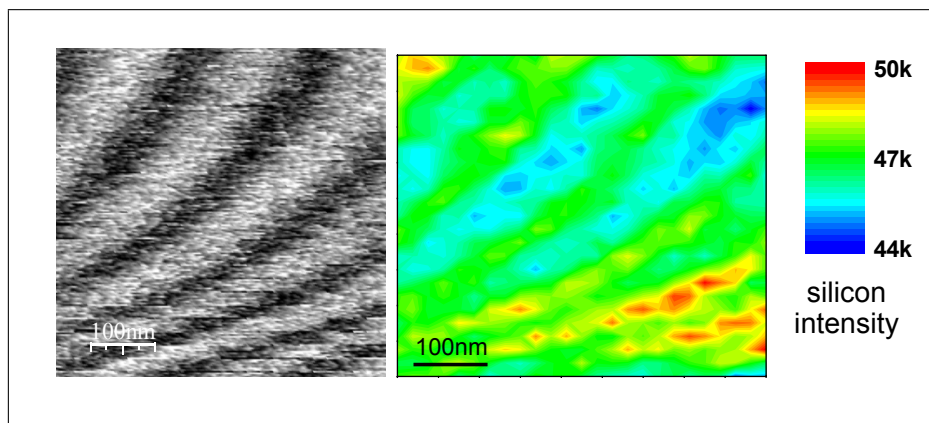
Figure 3.28.: 50nm silicon trenches etched 20nm deep. *Left:* AFM topography information, *Right:* intensity of the Raman signal from silicon. The curved trenches result from a sample drift during the measurement.

This 'negative example' shows that for true statements about an increase in optical resolution the optical signal should not be dependent on the signal used for feedback mechanism. As a consequence, samples which are completely topography free should be used.

Thus statements like:

> *The TERS scan of PMMA lines on CdS indicate extremely high lateral res-*
> *olution, probably comparable to the experimental uncertainty of 20 nm.*

from [83] should probably reconsidered. Similar care should be taken when speaking about improved optical resolution after mapping point like single structures, e.g. carbon nanotubes or when treating with very low absorption depths as in UV laser Raman measurements [84].

4. Summary & Outlook

Raman microscopy was used to measure stress in semiconductor structures. It was shown that it is possible to map the stress distribution in real devices and compare the influence of different process parameters and materials. To a certain extend statements about the direction of the stress can be drawn by changing the polarization settings.

When observing complex structures there is always the problem of topographic artifacts. A novel method was developed to address this issue. By obtaining both, the Stokes and the Anti-Stokes Raman peak additional information can be gained. Using the Stokes-Anti-Stokes-Difference method, the different influences on the Raman peak shift can be deconvoluted. Thus, clear differentiation between topographic effects, tool features and possible drift effects on the one hand and stress related effects on the other hand is possible. By this, real stress maps with near diffraction limited spatial resolution can be obtained in complex semiconductor structures by Raman microscopy.
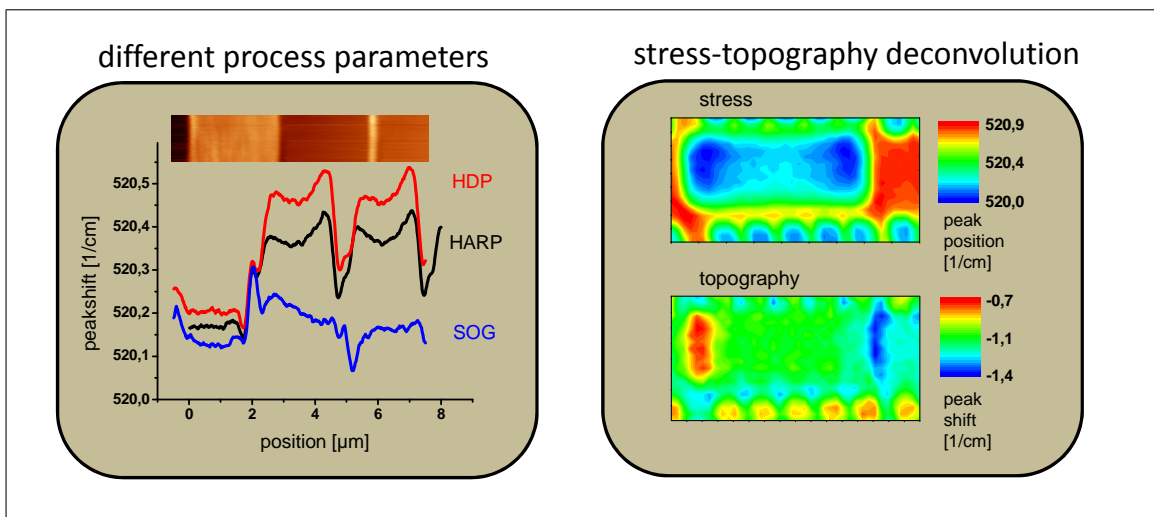
Figure 4.1.: *Left:* Raman linescan, different process parameters of the silicon oxide, *Right:* Raman maps deconvoluted into stress and topography dependent peakshift effects by the SAD method.
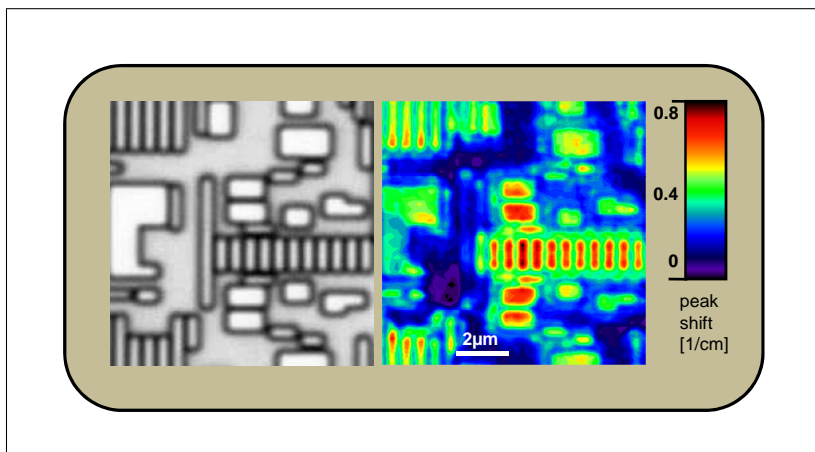
Figure 4.2.: High precision stress map obtained by overlay of Raman peakshift data with topographic information.

In chapter 3 a study about the effect of metal nanoparticles on the Raman spectrum of semiconductor materials was presented. To simplify the rather complex situation of a metallic tip to enhance the Raman signal, metal nanoparticles were directly deposited on the sample and a variety of parameters were changed and analyzed regarding their effect on the signal enhancement and localization.
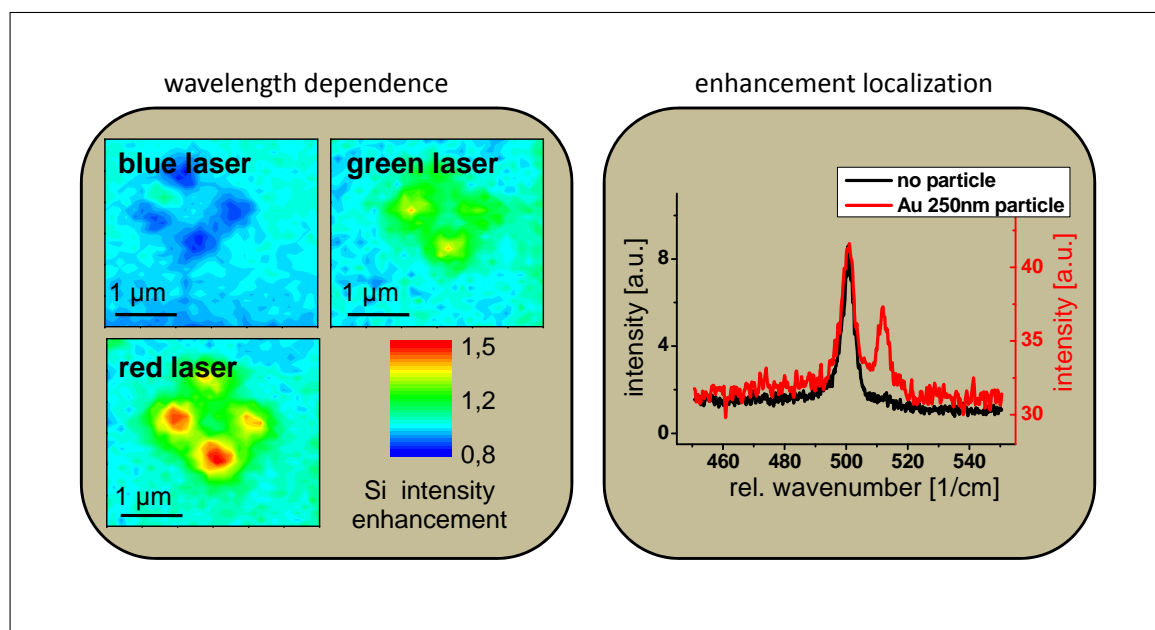
Figure 4.3.: *Left:* Wavelength dependence of SERS enhancement, *Right:* Enhancement localization on strained silicon layer.

A strong size and wavelength dependence could be observed and maximum signal enhancement was achieved when meeting the plasmon resonance of a given particle. By using different polarization settings, the contrast between the far-field and the near-field portion of the Raman signal can be greatly increased. With the help of stacked samples it could be shown that the enhancement is indeed localized, thus meeting a prerequisite for a local resolution below the diffraction limit.

To move from immobile enhancing particles to a scannable setup, metal particles have been attached to a scanning probe tip by a tip picking procedure. Although the present scanning and feedback setup proved to be suboptimal for nanometric resolution TERS scans, first clues of a improved resolution on semiconductor samples could be shown.
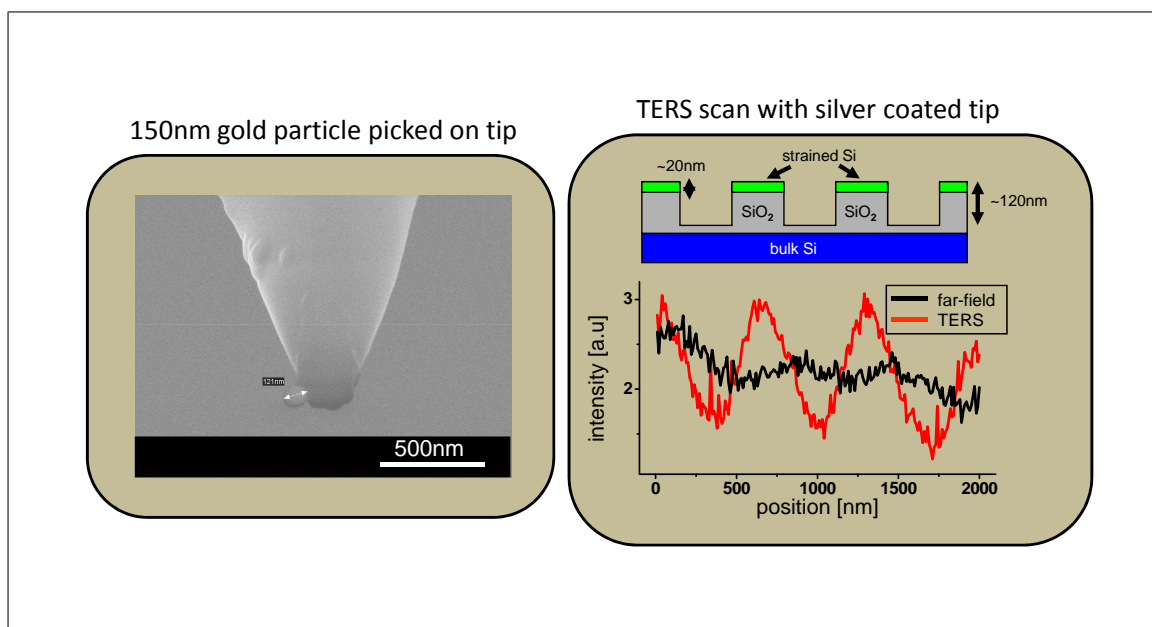
Figure 4.4.: *Left:* SEM view of picked gold particle, *Right:* TERS scan over structured silicon sample.

The ideal choice would be a setup combining two crucial conditions. On the one hand, the peak shift has to be measured with high spectral resolution and the data have to be acquired and analyzed in a way, that only stress related peak shift effects are obtained, as presented in chapter 2. On the other hand the localized enhancement of the Raman signal by using some kind of TERS tip has to be available in the same tool. Here, metal particles, carefully chosen according to the SERS parameter study presented in chapter 3 and picked on scanning probe tips might offer the successful increase in lateral resolution, thus breaking the diffraction limit.

Real TERS scans on silicon like samples remain challenging, but with precise feedback controls and careful choice of the illumination settings and tip parameters, near-field enhanced Raman scattering will be a promising tool for today's metrology in semiconductor industry and it's increasingly challenging demands.

A. Appendix

A.1. Peak fitting

All Raman spectra recorded during this work were saved as ASCII files and imported into Origin. There the data analysis, like peak fitting or two-dimensional mapping, was done. With the data files sometimes containing several thousands of spectra a self-made skipt was developed for the peak fitting process. The next box shows the macro for a fit of two different Lorentz curves, for example used in spectra of sSoI samples.

Listing A.1: fit skript

```
allspectra = 9;                                    //number of total spectra
win −a Data1;
for (ii = 2; ii <= $(allspectra+1); ii++)
    {work −n $(ii) B$(ii−1); work −t $(ii) 1;};    //renaming of columns

create results −w $(allspectra) number spos
sint swidth bpos bint bwidth back sarea barea error;  //creation of results worksheet
nlsf.cleanUpFitData();

nlsf.numfitsets=1;
nlsf.func$ = Lorentz;                              //type of fitting curve
nlsf.numReplica = 1;                               //number of additional peaks
y0=10;xc1=520;xc2=514;w1=4;w2=4;A1=50;A2=8000;     //initial fit parameters
nlsfv1=1;
nlsf.lbon1=1;nlsf.ubon1=1;nlsf.lbon2=1;nlsf.ubon2=1;
nlsf.lbon3=1;nlsf.ubon3=1;nlsf.lbon4=1;nlsf.ubon4=1;
nlsf.lbon5=1;nlsf.ubon5=1;nlsf.lbon6=1;nlsf.ubon6=1;
nlsf.lbon7=1;nlsf.ubon7=1;                         //activation of fitting bounds

nlsf.lb1=0;nlsf.ub1="−−";nlsf.lb2=519;nlsf.ub2=522;
nlsf.lb3=2;nlsf.ub3=6;nlsf.lb4=0;nlsf.ub4="−−";
nlsf.lb5=510;nlsf.ub5=519;nlsf.lb6=3;nlsf.ub6=9;
nlsf.lb7=0;nlsf.ub7="−−";                          //fitting bounds

break.open(progress);
for (pp = 1; pp <= $(allspectra); pp++)            //start of fitting loop
{
nlsf.begin();
nlsf.fitdata1$ = Data1_B$(pp);                     //data to be fitted
nlsf.iterate(20);                                  //number of fitting iterations
if( xc1 < xc2 )
{xl=xc1; xh=xc2;Al=A1;Ah=A2;wl=w1;wh=w2;}
```

```
else
{xh=xc1;xl=xc2;Ah=A1;Al=A2;wh=w1;wl=w2;}              //declaration of peak order
 results_number[pp] = pp;
 results_bpos[pp] = xh;
 results_spos[pp] = xl;
 results_barea[pp] = Ah;
 results_sarea[pp] = Al;
 results_bwidth[pp] = wh;
 results_swidth[pp] = wl;
 results_bint[pp] = 2*Ah/(PI*wh);
 results_sint[pp] = 2*Al/(PI*wl);
 results_back[pp] = y0;
 results_error[pp] = nlsf.chisqr;                     //fitting results
nlsf.msgPrompt=0;
nlsf.end(13);
nlsf.cleanUpFitData();

break.set(pp);
break.max = allspectra;
if (break.abort == 1) {break;};                       //progress bar and abort function
};
break.close();
```

A.2. Mathcad calculations

Defocussing
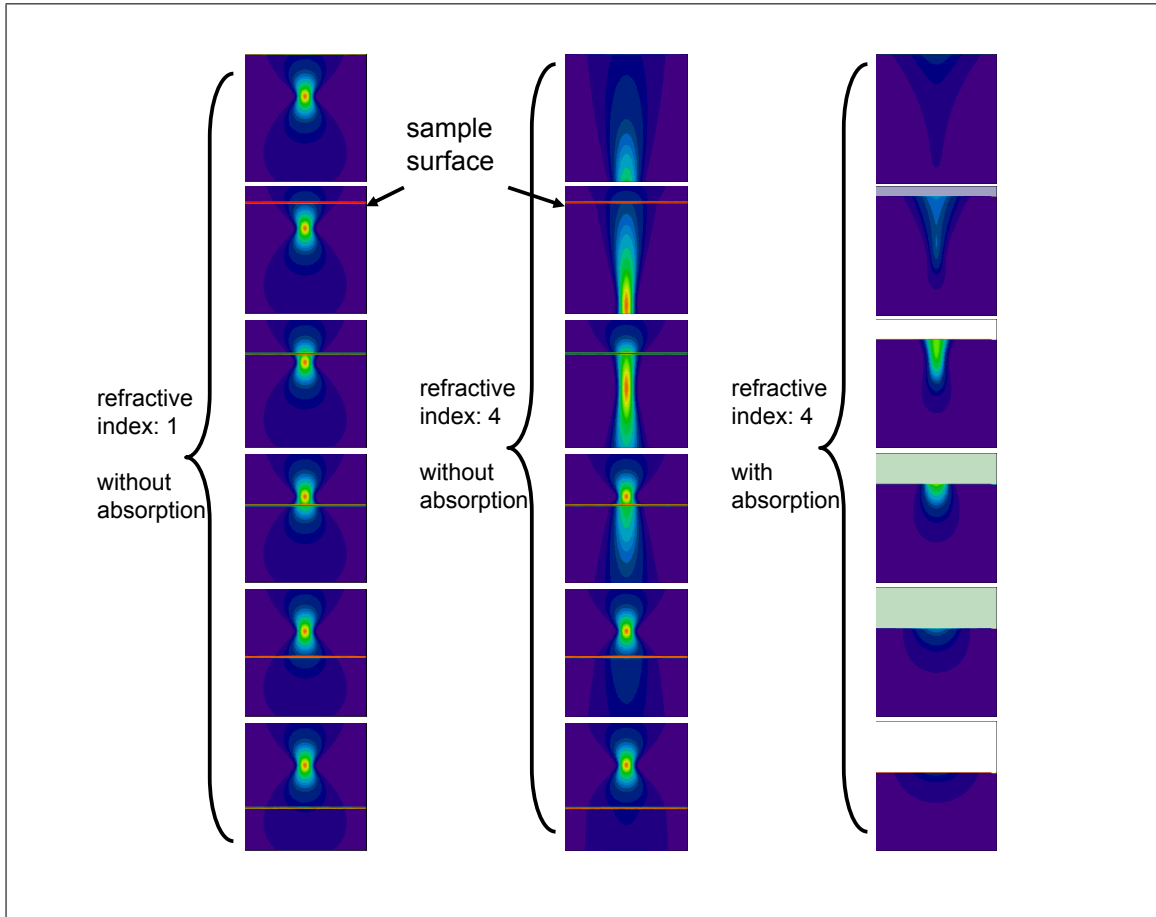
Figure A.1.: Intensity distribution of a Gaussian laser beam (633 nm) in a silicon
sample, *Left:* focused two microns above, *Middle:* directly on the
sample's surface, and *Bottom:* two microns inside the sample. The
dashed line illustrates the position of the focus.

Edge effect

The program used for the simulation of a linescan over a silicon step is based
on a two-dimensional model using raytracing The topography is modeled by
a stepping function, then every point in the sample is treated as an individual
Raman scatterer where the light radiates uniformly in all directions. This con-
tinuous spectrum is divided in discrete rays with a specific angle (for example

every half degree from $-180°$ to $+180°$). Every ray is then followed and its intersection with the topography function is calculated together with the intersecting angle. Dependent on the refractive index on the sample it is then decided if the ray can leave the sample by refraction and under which angle, or if the ray is reflected totally. If the individual ray can leave the sample it is checked if it has another intersection with the topography (for example at the step causing the later shadowing effect). In the case the light beam passes total reflection and step shadowing the angle at which it leaves the sample is compared to the objectives numerical aperture to see if it can be detected. Only then the ray can contribute to the total signal and the amount of this contribution is weighted with the distance it travels through the sample because of the absorption in the silicon. The sum of this contribution from all rays from a specific grid point then defines the value in the color coded model.

The linescan was calculated by having a Gaussian laser beam incident on the sample over a certain scanning point. Then the amount of laser power reaching a certain point is multiplied with the point's ray tracing value calculated before. After that the integration over the whole region is done and the result represents the intensity at a given scanning point.

Listing A.2: linescan parameters

```
h       = 200   //step height in nm
w       = 400   //step width in nm
n1      = 1     //refractive index of upper material air
n2      = 4     //refractive index of lower material silicon
l       = 4500  //scanning distance in nm
lambda  = 488   //laser wavelength in nm
NA      = 0.8   //numerical aperture of objective
alpha   = 1300  //absorption coeff. of Si for lambda=488nm in 1/mm
```

A.3. FE simulations

Finite element modelling of the x stress component in a STI structure with different processing parameters, with and without a 2.5 nm thin layer of thermal oxide at the bottom and side walls of the trenches. The huge influence of different process parameters can be seen.
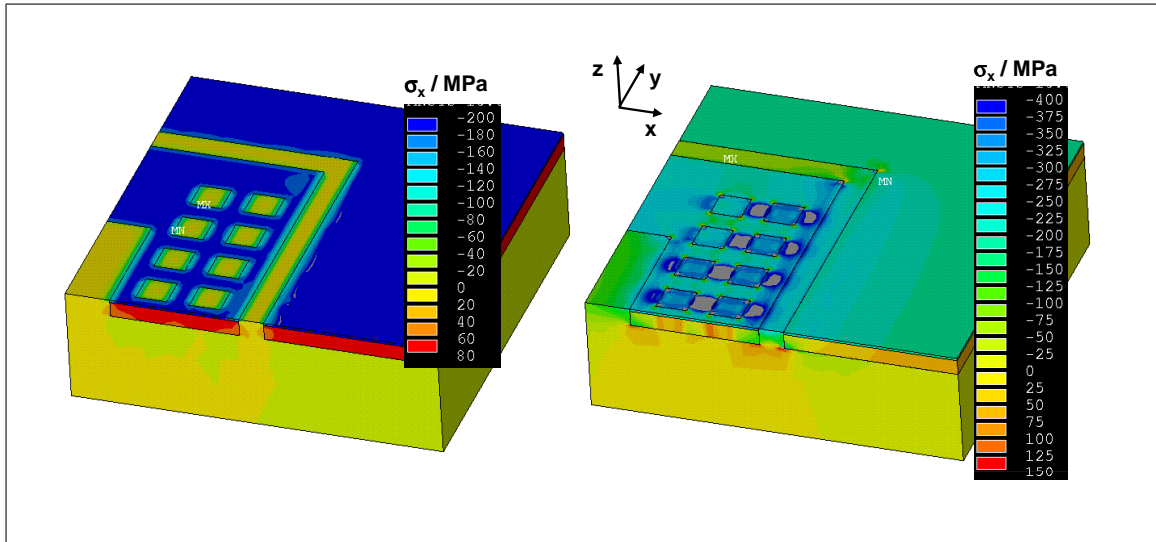
Figure A.2.: FE simulation of the x stress component in a STI test structure. *Left:* ANSYS simulation without thermal oxidation layer, *Right:* ANSYS simulation with thermal oxidation layer.

B. Bibliography

[1] S.A. Smee, M. Gaitan, D.B. Novotny, Y. Joshi, D.L. Blackburn. IC Test Structures for Multilayer Interconnect Stress Determination. *IEEE Electron Dev. Lett.*, 21:12-14, 2000.

[2] P.M. Zeitzoff, J.A. Hutchby, H.R. Huff. MOSFET and Front-end Process Integration: Scaling Trends, Challenges, and Potential Solutions Through The End of The Roadmap. *Intl. J. of High-Speed Elect. and Systems*, 12:267-293, 2002.

[3] R. Arghavani, N. Derhacobian, V. Banthia, M. Balseanu, N. Ingle, H. MSaad, S. Venkataraman, E. Yieh, Z. Yuan, L.-Q. Xia, Z. Krivokapic, U. Aghoram, K. MacWilliams, S. E. Thompson. Strain engineering to improve data retention time in nonvolatile memory. *IEEE Trans. Electr. Dev.*, 54(2):362-365, 2007.

[4] G. E. Moore. Cramming More Components onto Integrated Circuits. *Electr. Mag.*, 38(8), 1965.

[5] I. Aberg, O.O. Olubuyide, C. Ni Chleirigh, I. Lauer, D.A. Antoniadis, et al. Electron and Hole Mobility Enhancements in Sub-10nm-thick Strained Silicon Directly on Insulator Fabricated by a Bond and Etch-back Technique. *Dig. of 2004 Symp. on VLSI Technol.*, 52-53, 2004.

[6] T. Ghani, M. Armstrong, C. Auth, M. Bost, P. Charvat, et al. A 90nm High Volume Manufacturing Logic Technology Featuring Novel 45nm Gate Length Strained Silicon CMOS Transistors. *IEDM Tech. Dig. 2003*, 978-980, 2003.

[7] L. Rayleigh. On the light from the sky, its polarization and color. *Phil. Mag.*, 41:274-279, 1871.

[8] A. Smekal. Zur Quantentheorie der Dispersion. *Naturwiss.* 11:873-875.

[9] C. V. Raman and K. S. Krishnan. A new type of secondary emission. *Nature*, 121:501-502.

[10] J. P. Russell. Raman scattering in silicon. *Appl. Phys. Lett.*, 6(11):223-224, 1965.

[11] K. Brunner, G. Abstreiter, B. O. Kolbesen, and H. W. Meul. Strain at Si—SiO$_2$ interfaces studied by Micron-Raman spectroscopy. *Appl. Surf. Science*, 39(1-4):116-126, 1989.

[12] R. Loudon. The Raman effect in crystals. *Adv. Phys.*, 13(52):423-482, 1964.

[13] E. Anastassakis, A. Pinczuk, and E. Burstein. Effect of static uniaxial stress on the Raman spectrum of silicon. *Solid State Commun.*, 8:133-138, 1970.

[14] E. Anastassakis, A. Cantarero, and M. Cardona. Piezo-Raman measurements and anharmonic parameters in silicon and diamond. *Phys. Rev. B*, 41(11):7529-7535, 1990.

[15] E. Anastassakis. Strain characterization of polycrystalline diamond and silicon systems. *J. Appl. Phys.*, 86(1):249-258, 1999.

[16] V. Poporchii, T. Tada, and T. Kanayama. High-spatial-resolution Raman microscopy of stress in shallow-trench-isolated Si structures. *Appl. Phy. Lett.*, 89(23):3505, 2006.

[17] E. Bonera, M. Fanciulli, D. B. Batchelder. Combining high resolution and tensorial analysis in Raman stress measurements of silicon. *J. Appl. Phys.*, 94(4):2729-2740, 2003.

[18] S. J. Harris, A. E. O'Neill, W. Yang, P. Gustafson, J. Boileau, W. H. Weber, B. Majumdar, S. Ghosh. Measurement of the state of stress in silicon with micro-Raman spectroscopy. *J. Appl. Phys.*, 96(12):7195:7201, 2004.

[19] H. Yin, R. L. Peterson, K. D. Hobart, S. R. Shieh, T. S. Duffy, J. C. Sturm. Tunable uniaxial vs biaxial in-plane strain using compliant substrates. *Appl. Phys. Lett.*, 87(06):1922, 2005.

[20] E. Bonera, G. Carnevale, and M. Fanciulli. Raman stress maps from finite-element models of silicon structures. *J. Appl. Phys.*, 100(3):3516, 2006.

[21] S. C. Jain, H. E. Maes, K. Pinardi. Stresses in strained GeSi stripes and quantum structures: calculation using the finite element method and determination using micro-Raman and other measurements. *Thin Solid Films*, 292:218-226, 1997.

[22] S. Ganesan, A. A. Maradudin, and J. Oitmaa. A lattice theory of morphic effects in crystals of the diamond structure. *Anals of Physics*, 56:556-594, 1970.

[23] I. De Wolf and H. E. Maes. Stress measurements in silicon devices through Raman spectroscopy: Bridging the gap between theory and experiment. *J. Appl. Phys.*, 79(9):7148-7156, 1996.

[24] E. Anastassakis and M. Siakavellas. Elastic properties of textured diamond and silicon. *J. Appl. Phys.*, 90(1):144-152, 2001.

[25] S. H. Christiansen, R. Singh, I. Radu, M. Reiche, U. Gösele, D. Webb, S. Bukalo, and B. Dietrich. Strained silicon on insulator (SSOI) by waferbonding. *Mat. Sci.*, 8:197-202, 2005.

[26] V. Paillard, B. Ghyselen, C. Aulnette, B. Osternaud, N. Daval, F. Fournel, H. Moriceau, T. Ernst, J. M. Hartmann, C. Lagahe-Blanchard, S. Pocas, P. Leduc, L. Vincent, F. Christiano, Y. Campidelli, O, Kermarrec, P. Besson, Y. Morand. Strain characterization of strained silicon on insulator wafers. *Micro. Eng.*, 72:367-373, 2004.

[27] N. Everall. The influence of out-of-focus sample regions on the surface specifity of confocal Raman microscopy. *Appl. Spec.*, 62(6):591-598, 2008.

[28] M. Schmidbauer, Th. Wiebach, H. Raidt, M. Hanke, and R. Köhler. Ordering of self-assembled SiGe islands studied by grazing incidence small-angle x-ray scattering and atomic force microscopy. *Phys. Rev. B*, 58: 10523-10531, 1998.

[29] M. Cazayous, J. Groenen, F. Demangeot, R. Sirvin, M. Caumont, T. Remmele, M. Albrecht, S. Christiansen, M. Becker, H. P. Strunk, H. Wawra. Strain and composition in self-assembled SiGe islands by Raman spectroscopy. *J. Appl. Phys.*, 91(10):6772, 2002.

[30] S. H. Christiansen, M. Becker, S. Fahlbusch, J. Michler, V. Sivakov, G. Andrä, R. Geiger. Signal enhancement in nano-Raman spectroscopy by gold caps on silicon nanowires obtained by vapour-liquid-solid growth.

[31] M. Deluca, T. Sakashita, C. Galassi, and G. Pezzotti. Investigation of local orientation and stress analysis of PZT-based materials using micro-probe polarized Raman spectroscopy. *J. Europ. Cer. Soc.*, 26:2337-2344, 2006.

[32] A. T. Tilke, R. Hampp, C. Stapelmann, M. Culmsee, R. Conti, W. Wille, R. Jaiswal, M. Galiano, A. Jain. STI Gap-Fill Technology with High Aspect Ratio Process for 45nm CMOS and beyond. *Adv. Semicon. Manufact. Conf.*, The 17th Annual SEMI/IEEE Volume , 22-24 May 2006 Page(s):71 - 76, 2006.

[33] M. Staedele, G. Ilicali, E. Landgraf, M. Goldbach, S. Finsterbusch, J. Lindolf, J. Radecker, B. Uhlig. Reduction of layout variations with stress-compensated hybrid STI fills: a comprehensive analysis. *VLSI Technology, Systems and Applications*, 130-131, 2008.

[34] B. Dietrich and K. F. Dombrowski. Experimental challenges of stress measurements with resonant micro-Raman spectroscopy. *J. Raman Spectrosc.*, 30:893-897, 1999.

[35] I. De Wolf. Micro-Raman spectroscopy to study local mechanical stress in silicon integrated circuits (Review). *Semicond. Sci. Technol.*, 11:139-154, 1996.

[36] A. Atkinson, S. C. Jain, H. E. Maes, K. Pinardi, and M. Willander. Depth profiling of strain using micro-Raman measurements. *Semicond. Sci. Technol.*, 16:584-588, 2001.

[37] K. Pinardi, S. C. Jain, M. Willander, A. Atkinson, H. E. Maes, R. Van Overstraeten. A method to interpret micro-Raman experiments made to measure nonuniform stresses: Application to local oxidation of silicon structures. *J. Appl. Phys.*, 84(5):2507-2512, 1998.

[38] E. H. Synge. A suggested model for extending microscopic resolution into the ultra-microscopic region. *Phil. Mag.*, 6:356-362, 1928.

[39] E. A. Ash and G. Nicholls. Super-resolution aperture scanning microscope. *Nature*, 237:510-513, 1972.

[40] D. W. Pohl, W. Denk, and M. Lanz. Optical stethoscopy: image recording with resolution $\frac{\lambda}{20}$. *Appl. Opt.*, 44:651-653, 1984.

[41] A. Lewis, H. Taha, A. Strinkovski, A. Manevitch, A. Khatchatouriants, R. Dekhter, and E. Ammann. Near-field optics: from subwavelength illumination to nanometric shadowing. *Nature Biotech.*, 21(11):1378-1386, 2003.

[42] M. Yoshikawa, M. Murakami, and H. Ishida. Highly sensitive detection of near-field Raman scattered light from strained Si/SiGe heterostructures by scanning near-field optical Raman microscope using ultraviolet resonant Raman scattering. *Appl. Phys. Lett.*, 92(09):1903, 2008.

[43] M. Futamata, A. Bruckbauer. ATR-SNOM-Raman spectroscopy. *Chem. Phys. Lett.*, 341:425-430, 2001.

[44] J. Schreiber, F. Demoisson, B. Humbert, G. Louarn, O. Chauvet, and S. Lefrant. Nanoscale-resolved subsurface imaging by scattering-type near-field optical microscopy. *AIP Conf. Proc.*, 685(1):181-184, 2003.

[45] S. Webster, D. A. Smith, D. N. Batchelder, S. Karlin. Sub-micron spatial resolution Raman spectroscopy and its application to stress mapping in silicon. *Synth. Metals*, 102:1425-1427, 1999.

[46] A. Rasmussen, V. Deckert. New dimension in nano-imaging: breaking though the diffraction limit with scanning near-field optical microscopy. *Anal. Bioanal. Chem.*, 381:165-172, 2005.

[47] T. Taubner, F. Keilmann, and R. Hillenbrand. Nanoscale-resolved subsurface imaging by scattering-type near-field optical microscopy. *Opt. Express*, 13(22):8893-8899, 2005.

[48] L. Novotny and B. Hecht. Principles of Nano-Optics. Cambridge Unversity Press, Cambridge, New York, first edition, 2006.

[49] A. L. Demming, F. Festy, and D. Richards. Plasmon resonances on metal tips: Understanding tip-enhanced Raman scattering. *J. Chem. Phys.*, 122(18):4716, 2005.

[50] N. Hayazawa, A. Tarum, Y. Inouye, S. Kawata. Near-field enhanced Raman spectroscopy using side illumination optics. *J. Appl. Phys.*, 92(12):6983-6986, 2002.

[51] B. Pettinger, B. Ren, G. Picardi, R. Schuster, G. Ertl. Nanoscale probing of adsorbed species by tip-enhanced Raman spectroscopy. *Phys. Rev. Lett.*, 92(9):6101, 2004.

[52] U. Neugebauer, P. Rösch, M. Schmitt, J. Popp, C. Julien, A. Rasmussen, C. Budich and V. Deckert. On the way to nanometer-sized information of the bacterial surface by tip-enhanced Raman spectroscopy. *ChemPhysChem*, 7:1428-1430, 2006.

[53] H. Watanabe, Y. Ishida, N. Hayazawa, Y. Inouye, and S. Kawata. Tip-enanced near-field Raman analysis of tip-pressurized adenine molecule. *Phys. Rev. B*, 69(15):5418, 2004.

[54] J. J. Wang, D. A. Smith, D. N. Batchelder, Y. Saito, J. Kirkham, C. Robinson, K. Baldwin, G. Li, B. Benett. Apertureless near-field Raman spectroscopy. *J. Microsc.*, 210(3):330-333, 2003.

[55] C. Vannier, B. S. Yeo, J. Melanson, and R. Zenobi. Multifunctional microscope for far-field and tip-enhanced Raman spectroscopy. *Rev. Sc. Instr.*, 77(02):3104, 2006.

[56] A. Hartschuh, N. Anderson, and L. Novotny. Near-field Raman spectroscopy using a sharp metal tip. *J. Microsc.*, 210(3):234-240, 2003.

[57] Y. Saito, M. Motohashi, and N. Hayazawa. Nanoscale characterization of strained silicon by tip-enhanced Raman spectroscope in reflection mode. *Appl. Phys. Lett.*, 88(14):3109, 2006.

[58] W. X. Sun and Z. X. Shen. Near-field scanning Raman microscopy using apertureless probes. *J. Raman Spectrosc.*, 34:668-676, 2003.

[59] N. Hayazawa, M. Motohashi, Y. Saito, H. Ishitobi, A. Ono, T. Ichimura, P. Verma, and S. Kawata. Visualization of localized strain of a crystalline thin layer at the nanoscale by tip-enhanced Raman spectroscopy and microscopy. *J. Raman Spectrosc.*, 38:684-696, 2007.

[60] M. Fleischmann, P. J. Hendra, and A. J. McQuillan. Raman spectra of pyridine adsorbed at a silver electrode. *Chem.Phys.Lett.*, 26(2):163-166, 1974.

[61] S. Nie and S. R. Emory. Probing single molecules and single nanoparticles by surface enhanced Raman scattering. *Science*, 257(5303):1102-1106, 1997.

[62] A. Otto. What is observed in single molecule SERS, and why? *J. Raman Spectrosc.*, 33(8):593-598, 2002.

[63] E. Abbe. Beitraege zur Theorie des Mikroskops und der mikroskopischen Wahrnehmung. *Archiv f. Mikroskop. Anat.*, 9(1):413-418, 1873.

[64] L. Rayleigh. Investigations in optics, with special reference to the spectroscope. *Phil. Mag.*, 8:261-247/403-411/477-486, 1879.

[65] L. Rayleigh. On the theory of optical images with special reference to the microscope. *Phil. Mag.*, 5:167-195, 1896.

[66] R. H. Ritchie. Plasma losses by fast electrons in thin films. *Phys. Rev.*, 106(5):874-881, 1957.

[67] P. B. Johnson and R. W. Christy. Optical constants of noble metals. *Phys. Rev. B*, 6(12):4370-4379, 1972.

[68] British Biocell International Ltd., United Kingdoms. http://www.britishbiocell.co.uk/products/goldreagents.asp?navid=2.

[69] K. Karrai and R. D. Grober. Piezoelectric tip-sample distance control for near field optical microscopes. *Appl. Phys. Lett.*, 66(14):1842-1844, 1995.

[70] Nanonics Imaging Ltd., Israel. http://www.nanonics.co.il/optical-fiber-afm-probes.html.

[71] T. Kalkbrenner, M. Ramstein, J. Mlynek, and V. Sandogdhar. A single gold particle as a probe for apertureless near-field optical microscopy. *J. Microsc.*, 202(1):72-76, 2001.

[72] T. Sato, D. Brown, and B. F. G. Johnson. Nucleation and growth of nano-gold colloidal lattices. *Chem. Commun.*, 11:1007-1008, 1997.

[73] C. Soennichsen. Plasmons in metal nanostructures. PhD thesis, LMU Muenchen, 2001.

[74] A. Bouhelier, J. Renger, M. R. Beversluis, and L. Novotny. Plasmon-coupled tip-enhanced near-field optical microscopy. *J. of Microsc.*, 210(3):220-224, 2003.

[75] O. J. F. Martin, C. Girard. Controlling and tuning strong optical field gradients at a local probe microscope tip apex. *Appl. Phys. Lett.*, 70(6):705-707, 1997.

[76] M. Micic, N. Klymyshyn, Y. D. Suh, and H. P. Lu. Finite element method simluation of the field distribution for AFM tip-enhanced surface-enhanced Raman scanning microscopy. *J. Phys. Chem. B*, 107:1574-1584, 2003.

[77] T. Häertling, P. Reichenbach, and L. M. Eng. Near-field coupling of single fluorescent molecule and a spherical gold nanoparticle. *Opt. Express*, 15(20):12806-12817, 2007.

[78] J. Renger. Excitation, interaction, and scattering of localized and propagating surface plasmons. PhD thesis, TU Dresden, 2006.

[79] Y. Saito, N. Hayazawa, H. Kataura, T. Murakami, K. Tsukagoshi, Y. In-ouye, S. Kawata. Polariztaion measurements in tip-enhanced Raman spec-troscopy applied to single-walled carbon nanotubes. *Chem. Phys. Lett.*, 410:136-141, 2005.

[80] B. J. Messinger, K. U. v. Raben, R. K. Chang, and P. W. Barber. Local fields at the surface of noble-metal microspheres. *Phys. Rev. B*, 24(2):649-657, 1981.

[81] C. Georgi, M. Hecker, and E. Zschech. Raman intensity enhancement in silicon-on-insulator substrates by laser deflection at atomic force mi-croscopy tips and particles. *Appl. Phy. Lett.*, 90(17):1102, 2007.

[82] A. Hartschuh, M. R. Beversluis, A. Bouhelier, and L. Novotny. Tip-enhanced optical spectroscopy. *Phil. Trans. R. Soc. Lond. A*, 362:807-819, 2004.

[83] D. Mehtani, N. Lee, R. D. Hartschuh, A. Kisliuk, M. D. Foster, A. P. Sokolov, J. F. Maguire. Scanning nano-Raman spectroscopy of silicon and other semi-conducting materials. *Advances in Nano-Optics and Nano-Photonics*, Tip En-hancement. Elsevier, 2007.

[84] V. Poborchii, T. Tada, and T. Kanayama. Edge-enhanced Raman scattering in Si nanostripes. *Appl. Phys. Lett.*, 94(13):1907, 2009.

[85] F. Keilmann and R. Hillenbrand. Near-field microscopy by elastic light scat-tering from a tip. *Phil. Trans. R. Soc. Lond. A*, 362:787-805, 2004.

List of Figures

Curriculum Vitae

Personal Details

Name   Benjamin Uhlig

Born   May 1st, 1982 in Dresden, Germany

Studies

2000–2005   Studies of 'Physics' at Technische Universität Dresden, Germany.

2004   Student research assistant at Leibnitz Institut IFW in Dresden.

2005   Passed final examinations. Diploma thesis 'Untersuchung dünner modifizierter Kupferschichten nach Implantation mit Silberionen' composited at Leibnitz Institut IFW in Dresden, supervised by Dr. S. Menzel, IFW, refereed by Prof. W. Möller, FZR Rossendorf, Germany.

2005-2009   Research for this PhD thesis at Institute of applied Photophysics (IAPP), Technische Universität Dresden, Germany, supervised by Prof. L. M. Eng.

Publications

2007   B. Uhlig, J.-H. Zollondz, M. Haberjahn, H. Bloess, and P. Kücher: 'Nano-Raman: Monitoring Nanoscale Stress'. *AIP Conf. Proc.*, **931**, p.84–88, 2007.

2008   M. Staedele, G. Ilicali, E. Landgraf, M. Goldbach, S. Finsterbusch, J. Lindolf, J. Radecker, B. Uhlig: 'Reduction of layout variations with stress-compensated hybrid STI fills: a comprehensive analysis'. *VLSI Technology, Systems and Applications*, **21-23**, p.130-131, 2008.

in preparation   B. Uhlig: 'Evaluation of enhanced Raman spectroscopy on semiconductors'.

invention   B. Uhlig, J.-H. Zollondz: Submission of invention: 'Improving the stress measurement in silicon devices', 2008.

Acknowledgement

Viele haben einen Anteil daran, dass diese Arbeit letztendlich fertig wurde. Ich möchte die Gelegenheit ergreifen sie hier zu erwähnen und danke:

- Prof. Lukas Eng für die Betreuung der Doktorarbeit, die Unterstützung und wissenschaftlichen Anregungen sowie die Bereitschaft die Arbeit zu begutachten.

- Prof. Alexander Michaelis für die Möglichkeit an diesem Thema und im Fraunhofer IKTS zu arbeiten, sein Interesse an dieser Arbeit und die Übernahme des Zweitgutachtens.

- Dr. Hendrik Zollondz meinem Betreuer seitens Qimonda, ein absoluter Glücksgriff. Egal ob es um wissenschaftliche, private oder lustige Dinge ging, er war immer da und sorgte für eine angenehme Atmosphäre.

- der Axio-Gruppe vom IAPP für die donnerstäglichen Gesprächsrunden und somit die Möglichkeit sich mit anderen jungen Wissenschaftlern auszutauschen. Aus dieser Gruppe besonders:

- Dr. Phillip Olk für die Hilfe mit $\LaTeX$, das Lektorieren der Arbeit und gemeinsam mit

- Marc Tobias Wenzel für die wissenschatlichen Anregungen und die Hilfe beim Tip-Picking

- Dr. Tobias Mayer-Uhma für die Unterstützung bei allen IKTS Verwaltungsgeschichten

- dem gesamten Metrology Team von Qimonda für die nette Arbeitsatmosphäre. Ich hoffe, dass inzwischen jeder ein neues Zuhause gefunden hat!

- vor allem meiner Familie und meiner Freundin Susan dafür, dass sie mich ausgehalten haben, für ihre Geduld und ihren Anteil an der Fertigstellung dieser Arbeit.

- nicht zuletzt allen die ich hier vergessen hatte, Danksagungen zählen eindeutig nicht zu meinen Stärken.

Erklärung

Die vorliegende Dissertation wurde am Institut für Angewandte Photophysik der Fakultät Mathematik und Naturwissenschaften an der Technischen Universität Dresden unter wissenschaftlicher Betreuung von Prof. Dr. Lukas Eng angefertigt.

Hiermit versichere ich, dass ich die vorliegende Arbeit ohne unzulässige Hilfe Dritter und ohne Benutzung anderer als der angegebenen Hilfsmittel angefertigt habe; die aus fremden Quellen direkt oder indirekt übernommenen Gedanken sind als solche kenntlich gemacht. Die Arbeit wurde bisher weder im Inland noch im Ausland in gleicher oder ähnlicher Form einer anderen Prüfungsbehörde vorgelegt.

Ich versichere weiterhin, dass bislang keine Promotionsverfahren stattgefunden haben.

Ich erkenne die Promotionsordnung der Fakultät Mathematik und Naturwissenschaften an der Technischen Universität Dresden vom 20.03.2000, in der Fassung der vom Fakultätsrat am 19.06.2002 und 12.07.2002 beschlossenen und mit Erlass des Sächsischen Staatsministeriums für Wissenschaft und Kunst vom 18.03.2003 genehmigten Änderungen gemäß Satzung vom 16.04.2003 sowie gemäß der Änderungssatzung vom 17.07.2008, an.

Dresden, den 22.12.2009

Benjamin Uhlig